Digital Calorimetry For Future e^+e^- Linear Colliders and Their Impact On The Precision Measurement of the Top Higgs Yukawa Coupling

Tony Price

Thesis submitted for the degree of
Doctor of Philosophy

Particle Physics Group,
School of Physics and Astronomy,
University of Birmingham.

August 25, 2013

Abstract

The International Linear Collider (ILC) is a proposed future e^+e^- linear collider which will make precise measurements of the Standard Model of Particle Physics. Novel detector systems with unprecedented performance are required to allow these measurements. This thesis focuses on the validation of a Digital Electromagnetic Calorimeter (DECAL) which infers the energy of the incident particles by counting the number of pixels fired (particles) in the shower rather than the energy deposited. The TPAC sensor has been developed for use as the active layer of a DECAL and its properties have been studied during beam tests at CERN and DESY. Data from these tests has been used to validate the DECAL concept by showing that pixel multiplicity increases with incident particle energy and material depth as expected for electromagnetic shower development. The radiation hardness of the TPAC sensors was also evaluated with a reduction in the signal to noise ratio of 8 % observed at doses up to 200 krad. The semileptonic decay of $e^+e^- \rightarrow t\bar{t}H$ has been studied at 1 TeV to evaluate the performance of the International Large Detector (ILD) yielding a predicted uncertainty on the measurement of the top Higgs Yukawa coupling of 6.9% with 1000 fb^{-1} of data. An investigation into the effect of the inclusion of a DECAL has yielded results consistent with a conventional calorimeter system.

Author's Contribution

Whilst the work detailed in this thesis falls under the umbrella of three collaborations, SPiDeR, CALICE, and the ILD Software and Analysis Working Group, the results presented are solely my own. Where this work has relied upon contributions from others this is clearly stated.

As a part of the SPiDeR Collaboration I attended the beam testing of the TPAC sensors at DESY where the data was collected to allow the studies into sensor and shower characteristics to be performed. Prior to the beam test I developed a simulation which aided the planning of the beam test, throughout the beam test I worked the night shifts monitoring the data which was being taken and performing basic analysis, and afterwards I completed an in depth analysis using the data obtained. I presented results of the beam test at three international conferences, TiPP2011, CALICE 2012, and LCWS12. For these conferences I not only completed the analysis but compiled the slides, presented at the conferences, and wrote any corresponding proceedings.

The TPAC sensors were irradiated with x-rays to evaluate their radiation hardness for future applications. For this work I designed the experiment, carried out all necessary irradiations and measurements, presented the results at TiPP2011, and wrote the results into a paper which was published by the Journal of Instrumentation [1].

As part of the ILD Software and Analysis Working Group I used centrally generated simulations to evaluate the performance of the ILD detector in measuring the top Higgs Yukawa coupling by studying the $e^+e^- \to t\bar{t}H$ interaction at the ILC operating at a centre of mass energy of 1 TeV. This analysis was essential for the ILC Technical Design Report as it was one of the requested benchmark processes to demonstrate the physics potential of the detector. I worked independently on the semileptonic decay channel of the $t\bar{t}$ system as described in this thesis which was then combined

with the hadronic channel into an LCnote [2]. For the LCnote I took a lead in the writing and editing stage pushing through the publication prior to the release of the Technical Design Report.

To evaluate the impact of replacing the conventional ECAL system within ILD I modified pre-existing full scale detector models in Geant4 to allow the implementation of tiny digital pixels. I then performed simulations on the BlueBEAR cluster [3] for both the conventional detector and the modified geometry to allow comparisons to be made between the technologies. These simulations amounted to over 2 TB of data and 80,000 CPU hours. The analysis of these simulations allowed me to evaluate the impact on the physics performance of the Digital ECAL.

Acknowledgements

I had intended on keeping these acknowledgements brief. However, when I sat down and thought of all the people who have helped me over the past 36 months the list became rather long.

Firstly, I would like to thank the University of Birmingham for giving me the opportunity to complete this work within their fantastic department and to the STFC for their financial backing. A special thank you is required for my supervisor, Nigel Watson, for his guidance, patience and flexibility, without which the completion of this thesis and the work it contains would not have been possible. I would also like to thank the other PhD students in the department for the correct blend of work, office badminton, and the construction of medieval warfare artifacts to keep me sane during the writing process.

The work completed in this thesis fell under the umbrella of three collaborations; SPiDeR; CALICE, and the ILD Software and Analysis Working Group. I would like to thank all members of these collaborations for tolerating my many presentations and always providing useful and insightful comments to help drive my work.

I should also acknowledge the financial support from EUDET, without which the DESY beam test data which formed such an integral part of my PhD would not have been taken. On this note, ATLAS students Thomas McLaughlan and Hardeep Bansil also receive my gratitude for attending the beam test and allowing a full three weeks data taking to be achieved.

During the course of my PhD I was lucky enough not only to work from my home institute but to also spend two long term attachments away from the department. I would like to thank Marcel Stanitzki who acted as my supervisor whilst at the Rutherford Appleton Laboratory. A particular mention should go to Vladimir Ra-

jovic who redesigned the sensor PCBs in his own time and unfunded, without which the radiation tests would not have been possible. A huge debt of gratitude is owed to the whole of the Experimental Physics Department of the University of Edinburgh for making me feel welcome at their institute for much longer than originally planned. In particular, I would like to thank Victoria Martin for taking me under her wing and aiding me through my physics study.

Finally, I would like to thank all of my friends and family for their love and support not only over the past 36 months but through the many years leading up to this point. To my mom for keeping me fed and in clean clothes during the writing up process; my dad for not moaning too much that his son has returned home for a third time; my Charlotte for her patience, support and motivation throughout, and the Poppy dog alarm clock system[1] for waking me up every morning for food and walkies.

[1] patent pending

For all of those who came along for the journey, and for Jake who we lost along the way.

Contents

List of Figures

List of Tables

List of Acronyms

AECAL Analogue Electromagnetic Calorimeter

CLIC Compact Linear Collider

CMB Cosmic Microwave Background

CoB Chip on Board

DECAL Digital Electromagnetic Calorimeter

DTU DAQ Threshold Unit

DPW Deep P-Well

DST Data Summary Tables

ECAL Electromagnetic Calorimeter

EWSB Electroweak Symmetry Breaking

FORTIS FOuR Transistor Imaging Sensor

GRPC Glass Resistive Plate Chambers

HCAL Hadronic Calorimeter

HEP High Energy Physics

HIRES High Resistivity

ILC International Linear Collider

ILD International Large Detector

IP Interaction Point

ISR Initial State Radiation

LEP Large Electron Positron Collider

LHC Large Hadron Collider

LOI Letter Of Intent

MAPS Monolithic Active Pixel Sensor

MIP Minimum Ionising Particle

PandoraPFA Pandora Particle Flow Algorithm

PandoraPFO Pandora Particle Flow Object

PDF Parton Distribution Function

PFA Particle Flow Algorithm

PMT PhotoMultiplier Tube

QED Quantum Electrodymamics

RAL Rutherford Appleton Laboratory

SET Silicon External Tracker

SiD Silicon Detector

SIT Silicon Inner Tracker

SPiDeR Silicon Pixel Detector R&D

SM Standard Model of Particle Physics

SPS Super Proton Synchrotron

TDR Technical Design Report

TPAC TeraPixel Active Calorimeter

TPC Time Projection Chamber

VTX Vertex Tracker

CHAPTER 1

Introduction

1.1 A Brief History of Time

In the beginning there was nothing, then almost instantaneously there was everything.

Observations by Hubble found that galaxies are receding with a velocity which is proportional to their distance from us [4]. The big bang theory is a cosmological model which takes the observations of Hubble and explains the evolution of the early universe. It states that the universe began approximately 14 billion years ago from a single point which underwent an unimaginably huge expansion in an infinitesimally small time and has been expanding and cooling ever since.

At approximately 10^{-10} s after the big bang the temperature of the universe is believed to have been 10^{15} K. At these temperatures the quarks and gluons were not

bound by the nuclear force and behaved like free particles. At 10^{-4} s the universe had cooled sufficiently such that the quarks and gluons became trapped by the strong force into protons and neutrons. The continued cooling of the universe saw protons and neutrons form together to make atomic nuclei around 1 s after the big bang. At this stage the universe was dominated by radiation and the photons were so energetic that they continually broke up any electrons which had combined with the atomic nuclei. Around 10^{12} seconds after the big bang the universe had cooled such that the photons could no longer break up the atoms [5]. Before the universe had cooled sufficiently for the electrons and ions to combine, the photons were trapped in the plasma due to constant scattering with the ions. When the electrons and ions did combine the mean free path of the photons effectively became infinite and matter and radiation became decoupled. The resulting radiation signature, the Cosmic Microwave Background (CMB), has been studied by astrophysicists since it was accidentally discovered in 1965 by Penzias and Wilson [6]. The results obtained by the Planck mission [7] have measured the CMB to an unprecedented level. Although these results give an insight into the universe shortly after the big bang, astronomy is unable to determine what happened prior to decoupling as the radiation cannot be measured.

High Energy Physics (HEP) experiments aim to recreate and study earlier epochs of the universe by colliding beams of high energy particles. The Large Hadron Collider (LHC) currently holds the world record for the highest man made collision energy of $\sqrt{s}$=8 TeV. Experiments at the LHC have tested the Standard Model of Particle Physics (SM), which explains the fundamental particles from which all matter is constructed and the interactions between them in the closest conditions to that of the early universe

1.2 Standard Model

Everything around us, from the air we breath, to the desk I am writing at, to the materials used to construct the LHC, is made up of protons, neutrons, and electrons. However, only one of these particles, the electron, can be classed as fundamental. The protons and neutrons consist of up quarks, down quarks and gluons in much the same way that atoms are constructed from protons, neutrons, and electrons. The electron neutrino, ν_e, the electron and up and down quarks complete the first generation of fundamental particles. The first generation of particles are joined by two more generations, with the particles having increasing mass as summarised in Table 1.1. An example of this is the muon, a particle from the second generation, which is effectively a heavy electron, and is surpassed in mass by the tau from the third generation. The electron, muon, and tau all have an associated neutrino and these six particles are know as leptons. The six quarks and six leptons are fermions as they all have an intrinsic spin of 1/2 $\hbar$ and are the building blocks for all matter in the universe.

Table 1.1: Properties of the fermions arranged into generations with the masses shown in brackets in units of [GeV/c^2] [8]

	Generation			Charge [e]
	I	II	III	
Quarks	u ($(2.3\pm0.6)\times10^{-3}$)	s ($(95\pm5)\times10^{-3}$)	t (173.5 ± 1.0)	+2/3
	d ($(4.8\pm0.5)\times10^{-3}$)	c (1.275 ± 0.025)	b (4.180 ± 0.03)	-1/3
Leptons	e^- (511×10^{-6})	μ^- (105.7×10^{-3})	τ^- (1.7768)	-1
	ν_e ($<2\times10^{-9}$)	ν_μ ($<0.19\times10^{-3}$)	ν_τ ($<18.2\times10^{-3}$)	0

Baryonic matter, such as protons and neutrons, are formed of three quarks and in the ground state have spins of 1/2 $\hbar$ or 3/2 $\hbar$ dependent on the orientation of the three quarks. Quarks can also be arranged in a quark anti-quark pair to yield a particle with integer spin (0 or 1) known as a meson (e.g. a pion). The baryons and mesons are collectively known as hadrons.

The SM not only explains the properties of the quarks, leptons and hadrons but also the ways in which they interact. There are four forces which interact with fermions

and therefore govern the World around us:

- the electromagnetic force,
- the strong nuclear force,
- the weak nuclear force, and
- gravity.

Of these forces the strong and weak nuclear forces have ranges comparable with the size of a nucleus. The strong nuclear force is the strongest of all the forces and is responsible for containing the quarks within a nucleon where the weak nuclear force governs processes such as β decay (which changes the flavour of a quark within a nucleon). The electromagnetic and gravitational forces act on particles at ranges larger than the size of a nucleon. The electromagnetic force acts on all charged particles and gravity on all particles with mass.

The SM incorporates all of the fundamental forces apart from gravity. The forces interact via the exchange of a particle called a gauge boson which is a fundamental particle with integer spin. The electromagnetic force is carried by the photon, the strong nuclear force via gluons and the weak interaction by charged W bosons and the neutral Z boson. The properties of the bosons are summarised in Table 1.2, including the hypothetical graviton for propagating gravity. As the photon is a stable particle with zero mass, the electromagnetic force has an infinite range. The range of the $W^{\pm}$ and Z bosons are set by their extremely short mean lifetimes and the speed of light. The gluons are fundamentally different to both photons and the weak gauge bosons as they have a finite range but are massless. This arises because the gluons carry colour charge and, as the strong force interacts with colour, gluons are self-interacting. It is postulated that only colour neutral particles can exist as free particles in nature and the confining behaviour of the strong force [9] on the colour charged gluon limits the range to within the nuclear volume.

Table 1.2: Properties of the force carrying bosons [8]

Force	Boson	Spin	Charge	Mass[GeV/c^2]	Lifetime [s]	Range [m]
electromagnetic	photon	1	0	0	∞	∞
strong	gluon	1	0	0	∞	10^{-15}
weak	$W^{\pm}$	1	±1	80.385±0.015	3.16×10^{-25}	9.48×10^{-17}
	Z	1	0	91.188±0.0021	3.64×10^{-25}	1.09×10^{-16}
gravity	graviton	2	-	-	-	-

The SM is one of the most precisely tested theories in physics. This is exemplified by tests carried out using one of its components, Quantum Electrodymamics (QED). For example, one of the most stringent measurements is that of the muon magnetic dipole moment, which has been measured with extreme precision and the theoretical prediction agrees within one part in 10^{-8} with data [10].

However, there are problems and anomalies in the SM including:

- the amount of matter and antimatter in the universe should be balanced due to lepton and baryon number conservation, this is in contrast to observations, and
- the fundamental particles should be massless.

The second of these problems is particularly poignant as discussed below.

In physics the symmetry of a system is important. Noether's theorem [11] states that if a system is symmetric under a transformation then there is a corresponding conservation law. For example if a system is symmetric under:

- a translation then momentum is conserved,
- a rotation then angular momentum is conserved, and
- a time change then total energy is conserved.

The concept of symmetries under transformations can be applied to the theories which govern the SM. The SM is a quantum field theory which is invariant under a change of gauge.

All gauge theories must be renormalisable for them to make finite predictions. When a theory is renormalisable, divergent integrals which can occur in the theory are cancelled by other divergent integrals and real, calculable predictions can be made. Without this, the theories would only be valid up to an arbitrary cut off point which is introduced to remove the logarithmically divergent integrals and its predictions would depend on the value of the cut-off. For a gauge theory to be renormalisable it must be gauge invariant.

Gauge invariance is a property of gauge fields which are unchanged in form by a gauge transformation. A gauge transformation is a transformation which changes the phase of a gauge field, the simplest example being a change in the global phase, independent of position.

The dynamics of a system can be explained using a *Lagrangian* function of the general form

$$\mathcal{L} = T - V \ , \tag{1.1}$$

where T is the kinetic energy and V is the potential energy of the system. In quantum field theory, the field of a system describing fermions is characterised by the Dirac field with the Lagrangian

$$\mathcal{L}_{Dirac} = i\overline{\Psi}\gamma^{\mu}\partial_{\mu}\Psi - m\overline{\Psi}\Psi \ . \tag{1.2}$$

When global gauge transformations involving a phase such as

$$\Psi(x) \rightarrow \Psi'(x) = e^{i\alpha}\Psi \ , \tag{1.3}$$

are applied to Equation 1.2 the Lagrangian is unchanged as $e^{i\alpha}e^{-i\alpha}$=1.

However, if the gauge transformation acts locally such that it is a function of time and position of the form $e^{-i\alpha(x)}$ then Equation 1.2 becomes

$$\mathcal{L}'_{Dirac} = i\overline{\Psi}\gamma^{\mu}\partial_{\mu}\Psi - m\overline{\Psi}\Psi - \overline{\Psi}(x)\gamma^{\mu}\Psi(x)\partial_{\mu}\alpha(x) \ , \tag{1.4}$$

and the gauge invariance is broken locally. To restore gauge invariance the derivative ∂_{μ} in Equation 1.2 needs to be replaced by a covariant derivative, D_{μ}, which transforms in the same way as $\Psi(x)$ such that

$$D_{\mu}\Psi(x) \rightarrow D'_{\mu}\Psi'(x) = e^{i\alpha(x)}D_{\mu}\Psi(x) \ , \tag{1.5}$$

which holds on the assumption that the covariant derivative has the form

$$D_{\mu} = \partial_{\mu} + ieA_{\mu} \ , \tag{1.6}$$

where the gauge field, A_{μ}, transforms as

$$A_{\mu} \rightarrow A'_{\mu} = A_{\mu} - \frac{1}{e}\partial_{\mu}\alpha(x) \ . \tag{1.7}$$

When the covariant derivative is substituted in Equation 1.2 and a local gauge transformation is applied the additional gauge field restores gauge invariance.

The addition of massive particles causes local fluctuations in the SM wavefunction which are cancelled out by the addition of the *Higgs field* and gauge invariance

is restored. For the Higgs field to interact with matter there must at least one additional exchange boson in the SM, termed the *Higgs Boson*.

1.3 Higgs Boson

The Higgs boson was originally proposed in 1964 by Peter Higgs [12] [13] as the mediator of the scalar field which gives mass to particles in the SM. The search for the Higgs boson has been long and varied with the Large Electron Positron Collider (LEP) in the 1990s and the Tevatron in the 1990s and 2000s only managing to set limits on the Higgs mass by excluding regions over which they had studied [14] [15]. Nearly 50 years after it was first proposed, a Higgs-like boson was finally observed at the LHC in 2012 [16] [17]. Since the discovery, measurements of the couplings have verified that the boson is in fact a Higgs boson [18].

The SM predicts many of the properties of the fermions and bosons which it describes. For example, the coupling of the Higgs boson [19] to fermions is predicted via

$$g_{ffH} = \frac{M_f}{\nu} \ , \tag{1.8}$$

and to vector bosons via

$$g_{VVH} = \frac{2M_V^2}{\nu} \ , \tag{1.9}$$

where M_f and M_V are the masses of the fermion and vector boson respectively and ν is the vacuum expectation value of the scalar Higgs field. The testing of these predictions to validate the SM can be achieved by measuring the branching fractions of processes which involve the couplings.

In the search for the W and Z bosons the experiments were tuned to look in a certain

region as their masses were predicted by the Higgs mechanism in the SM. However, the search for the Higgs boson took a huge amount of time as its mass is predicted via

$$M_H^2 = 2\lambda\nu^2 \ , \tag{1.10}$$

where both M_H and λ are unknowns preventing a direct prediction of the Higgs mass. Whilst LEP had set a lower limit of 114.4 GeV/c^2 [14] the upper limit, on a theoretical basis, could be $\sim$1 TeV before breaking the SM. To explore such a huge range in potential masses the LHC was built to collide protons with a design collision energy of 14 TeV. However, as the proton is a composite particle not all of the energy is available to the hard process in the collision as it is the quarks and gluons within the protons which actually interact. The energy of the collision is calculated on a statistical basis using Parton Distribution Functions (PDF)s which describe the fraction of the total proton energy each parton has. Whilst PDFs are generally understood, a limit on the precise measurements at the LHC can be imposed from the uncertainty in $\sqrt{s}$ [20]. This contributes to the notion that the LHC is a "discovery machine" as it has the potential to search for new physics at many energies whereas lepton colliders, which collide fundamental particles, such as LEP or the proposed International Linear Collider (ILC), have a significantly narrower range of energies at a given $\sqrt{s}$.

1.4 Calorimetry

A calorimeter is a device used to measure the energy deposited within a medium and forms an integral part of any HEP detector. The calorimeter systems within a detector at a HEP facility are formed of two main parts, the Electromagnetic Calorimeter (ECAL) which is designed to measure the energy deposited by electromagnetic particles (electrons and photons), and the Hadronic Calorimeter (HCAL)

which is designed to measure the properties of hadrons.

Electromagnetic and hadronic particles differ in their interactions with matter, leading to differing designs for the calorimeter components to detect the resulting particle showers. As this thesis focuses on the construction of a Digital Electromagnetic Calorimeter (DECAL) attention will only be paid to electromagnetic showers. Further information on hadronic showers is available in many sources e.g. [21].

1.4.1 Electromagnetic Showers

The particles created when an electromagnetic particle interacts with a material can be characterised in terms of the radiation length, χ_0, of the material. The radiation length is defined as "the distance travelled by an electron through a material until its energy has reduced to a factor of 1/e by bremsstrahlung". It can be approximated using [22]

$$\frac{1}{\chi_0} = 4\alpha r_e^2 \frac{N_A}{A} Z^2 \ln(183/Z^{-\frac{1}{3}})) \ , \tag{1.11}$$

where α is the fine structure constant, N_A is Avogadro's number, A and Z are the atomic mass and number of the absorber, and r_e is the classical electron radius.

When an electron (photon) interacts with a material, electrons, positrons and photons are created via bremsstrahlung (pair production) with a lower energy than the parent particle. These particles then also interact and a particle shower develops. This process continues until the energy of the particles are below the critical energy of the material, E_c, where ionisation dominates and the particles deposit their energy in the medium. The energy deposition as a function material depth is given by [8]

$$\frac{dE}{dt} = E_0 b \frac{(bt)^{a-1} \exp(-bt)}{\Gamma(a)} \ , \tag{1.12}$$

where E_0 is the energy of the incident particle, a and b are properties of the absorbing material and the depth in radiation lengths traversed by the particle, t, is defined as

$$t = \frac{x}{\chi_0} \ . \tag{1.13}$$

The depth at which the shower deposits the maximal amount of energy is given by

$$t_{max} = \frac{(a-1)}{b} = \ln(y) + C \ , \tag{1.14}$$

where $C = -0.5$ for electron induced showers and $C = +0.5$ for photon induced showers, and

$$y = \frac{E_0}{E_c} \ . \tag{1.15}$$

The depth of a calorimeter is typically designed to contain between 95% or 99% of the longitudinal shower energy depending on the required energy resolution. The exponential behaviour of Equation 1.12 can lead to large differences between the two measures and will impact heavily on both the size and costs of the ECAL. The total thickness required to longitudinally contain 95% of the energy of a 100 GeV electron is $\sim$17 χ_0. If this is increased to a 99% containment the calorimeter needs to be 17% deeper at $\sim$20 χ_0 [21].

The lateral development of the electromagnetic shower is parameterised by the Molière radius of a material which is the radius within which 90% of the energy is deposited. It is related to the radiation length of the absorbing material by [8]

$$\mathcal{R}_{\mathcal{M}} = \frac{21\text{MeV}}{E_c}\chi_0 \ . \tag{1.16}$$

In order to separate overlapping showers, the Molière radius of a calorimeter needs to be small compared to the typical transverse separation of particles entering the ECAL. In general, the granularity of a calorimeter is kept as close as possible to the Molière radius.

Although there are a wide range of designs for calorimeter systems used in HEP, they can be classified into two main types, homogeneous and sampling calorimeters as outlined below.

Homogeneous Calorimeter

A homogeneous calorimeter generally consists of high density crystals and it acts both as the absorber and the active medium. There are a variety of materials used with readout generally occurring from scintillation or Cherenkov light which is fed into a PhotoMultiplier Tube (PMT). The materials need to have a short radiation length (to contain the shower in as short a distance as possible) and be opaque (to allow the light to reach the PMTs).

As all of the particle's energy is deposited within the active layer of the calorimeter the energy resolution which can be achieved is excellent. However, very little information on the depth of the shower is available and the spatial resolution is dominated by the size of the crystals. In order to fully contain high energy particles the crystals need to be deep in terms of χ_0 and very pure which makes the crystals both difficult and very expensive to produce.

Sampling Calorimeter

A sampling calorimeter consists of many alternating layers of sampling and absorbing material. The basic set-up of a sampling calorimeter is a layer of absorbing material, usually a high Z material such as steel or tungsten, followed by a low Z, easily ionisable sampling material such as plastic scintillators or silicon. The ab-

sorbing material causes a particle to shower creating lower energy particles which then deposit a small amount of energy in the sampling material. The small amounts of energy deposited in all of the sampling layers are then summed and scaled to find the true energy of the incident particle. If the ratio of sampling to absorbing material between the layers is constant throughout the calorimeter this is a simple process. However, if the ratios change then an algorithm must be developed for the calorimeter to scale the energy correctly.

The energy scaling utilises a property of the layers known as the sampling fraction, $\mathcal{F}_{samp}$. This is the ratio of the energy deposited by a Minimum Ionising Particle (MIP) in one sampling layer, E_{Dep}^{samp}, to the energy deposited by a MIP in one complete layer including the sampling and absorbing material, E_{Dep}^{layer}, by

$$\mathcal{F}_{samp} = \frac{E_{Dep}^{samp}}{E_{Dep}^{layer}} \ . \tag{1.17}$$

In general sampling calorimeters are divided into regions where the thickness of the absorbing material differs and each region will have its own sampling fraction which will be fed into the scaling algorithm. The sampling fraction is calculated by a variety of methods including; simulating muons through a layer of the detector; test beam data, and later on during commissioning of the calorimeter using cosmic muons. There are uncertainties associated with the scaling fraction which can occur from fluctuations in the energy deposition and shower properties and a larger sampling fraction is preferred to reduce these effects. The sampling fraction can be increased in one of two ways; either by increasing the thickness of the sampling layers, or by having many finely segmented alternating layers of sampling and absorbing material.

1.4.2 Energy Resolution

The energy resolution, σ/E, of an ECAL is governed by many factors including; shower fluctuations; sampling fluctuations; noise in the electronics of the readout;

calibration of the calorimeter, and leakage of the shower from the calorimeter (both longitudinal and transverse). Each of these factors has an associated energy dependence and this allows the uncertainties to be arranged into groups. For a sampling calorimeter to be viable, the energy resolution must be dominated by the shower and sampling fluctuations.

The intrinsic resolution of the calorimeter is determined by the fluctuations of physical processes within the shower. Whilst the rules determining the shower development are fixed, the actual interactions occur randomly meaning that each and every shower is different. The number of particles in a shower is governed by Poisson statistics and as such the uncertainty is proportional to $1/\sqrt{N}$. The number of particles in a shower is proportional to the energy of the incident particle and as such the uncertainty can also be expressed as $\sigma_{shower}/\sqrt{E}$.

As the energy is deposited by low energy electrons, positrons, and photons their range in the absorbing material is greatly reduced. If the absorbing material is too thick the fraction of the shower which reaches the sampling layers in a state where energy is readily deposited is diminished. The uncertainty in the fluctuations in the number of particles reaching the sampling layer is $\sqrt{E_c t_{abs}/E}$ or $\sigma_{samp}/\sqrt{E}$ where t_{abs} is the thickness of the absorbing material and σ_{samp}=$\sqrt{E_c t_{abs}}$.

Until now, an assumption has been made that all of the particles in the shower pass through the same amount of absorber material. However, all of the particles will traverse the calorimeter at different angles and will therefore pass through varying thicknesses of absorbing and sampling materials. This effectively modifies t_{abs} per particle and must be accounted for. In addition to this the energy deposition in thin layers of materials follows a Landau distribution rather than a Gaussian in thicker materials. The scaling of the energy distribution for slight increases in sampling material depth are therefore more complex and adds an extra uncertainty of $\sigma_{landau}/\sqrt{E}$.

For sampling layers such as plastic scintillators there are fluctuations in the conver-

sion of charged particles into photo electrons which affects the size of the signal and leads to an additional uncertainty in the energy resolution. Again, the number of photons are proportional to the energy of the ionising particles and the fluctuations in the number are described by a $1/\sqrt{N}$ relationship leading to a contribution to the energy resolution of $\sigma_{pe}/\sqrt{E}$.

The readout systems of the sampling layers will have an associated electronic noise. As this noise contribution is assumed to be constant and independent of the signal size the noise has a σ_{noise}/E dependence and its contribution quickly falls away as the size of the energy deposition increases.

There may also be a term in the energy resolution from miscalibrations of the calorimeter during detector commissioning. It is generally accepted that the contribution to the energy resolution of a calorimeter from miscalibrations has the form σ_{cal}/E and once again becomes less significant with increasing energy.

The final source of uncertainty arises due to leakage of the shower from the calorimeter. There can be a significant constant term in the energy resolution associated with the leakage which does not vary with particle energy. There are two forms of leakage; longitudinal and transverse. Longitudinal leakage occurs when the calorimeter is too shallow to fully contain the shower. Transverse leakage originates when the Molière radius of the shower is greater than the lateral dimensions of the calorimeter. Longitudinal leakage is more severe than transverse with a 10% transverse energy leakage being equivalentto that of a 5% longitudinal leakage in the energy resolution [21].

All of these contributions to the energy resolution are added in quadrature to calculate the overall resolution via,

$$\frac{\sigma_E}{E} = \frac{\sigma_{shower}}{\sqrt{E}} \oplus \frac{\sigma_{samp}}{\sqrt{E}} \oplus \frac{\sigma_{landau}}{\sqrt{E}} \oplus \frac{\sigma_{pe}}{\sqrt{E}} \oplus \frac{\sigma_{noise}}{E} \oplus \frac{\sigma_{cal}}{E} \oplus \sigma_{leak} \quad . \tag{1.18}$$

As mentioned earlier the terms with the same energy dependence are often grouped together to yield the general expression for the energy resolution of

$$\frac{\sigma_E}{E} = \frac{a}{\sqrt{E}} \oplus \frac{b}{E} \oplus c \ . \tag{1.19}$$

1.4.3 Digital Calorimetry

The premise of digital calorimetry is to count the number of particles in a shower rather than the total energy which they deposit. Whilst the noise (b/E) and leakage (c) terms in Equation 1.19 are unaffected by this change in approach, theoretically there are large gains to be made with digital calorimetry via the stochastic ($a/\sqrt{E}$) term.

In conventional calorimeters the final measurement is reliant on the total energy deposited within the sampling layers. As this is affected heavily by the Landau fluctuations in the energy deposition per particle and the number of particles in a shower, the uncertainty can be large and complex. However, a digital calorimeter merely counts the numbers of particles in the shower which is readily understood from Poisson statistics. If this number can be accurately measured then the uncertainty associated with the Landau fluctuations can be removed and the energy resolution approaches the intrinsic resolution. The basic design feature required to achieve this is that each cell within the calorimeter only records at most one shower particle.

There are additional complications involved with the digital calorimeter method which do not arise in the conventional approach, the main one being saturation. If multiple particles pass through the same cell of a conventional calorimeter the output signal increases and the reconstruction algorithms can account for this and no signal is lost. In the case of a digital calorimeter this can potentially be disastrous. A single cell within a digital calorimeter only registers that something has happened which has pushed the cell over threshold. When multiple particles pass through the same cell the number of particles in the shower will be underestimated leading to an underestimation of the energy of the incident particle. As this is increasingly

probable for incident particles with higher energies, the calorimeter will have a non-linear response at higher energies. To avoid this, a cell in a digital calorimeter must be designed such that it is small enough that, even in very dense particle showers, only one particle passes through each pixel per shower.

For example, the estimated peak density in the core of an electromagnetic shower at the ILC is 100 particles/mm^2 and to avoid saturation occurring the cell sizes need to be approximately 50×50 μm^2. In the ECAL of the International Large Detector (ILD) at the ILC this would lead to a total of $\sim 10^{12}$ cells each requiring power supplies, readout electronics and cooling which would create large dead areas associated with each cell. The cells would thus need to have integrated electronics and use minimal power to reduce the cooling requirements. Whilst these factors complicate the design of a digital calorimeter, the technology is under serious consideration for both the ECAL and HCAL systems of detectors at future linear colliders [23] [24] and much effort has been invested in the R&D to achieve these design goals [25].

1.5 TeraPixel Active Calorimetry Sensor

1.5.1 Introduction

The CALICE-UK Collaboration [26] developed and tested the TeraPixel Active Calorimeter (TPAC) sensor for use in a binary readout DECAL within the detectors at a future e^+e^-collider such as the ILC. TPAC is based on CMOS Monolithic Active Pixel Sensor (MAPS) technology and is the first prototype device for such an application. The testing of these sensors forms an integral part of this thesis.

CMOS sensors can be fabricated for many purposes due to the huge combination of potential components including resistors, capacitors, diodes, and PMOS and NMOS transistors. The large variety of electrical components also leads to the potential of

integrated electronics within the pixels. In general, the charge deposited within the sensitive regions of a CMOS sensor is allowed to diffuse towards diodes where it is collected. However, in conventional CMOS sensors the use of PMOS transistors is restricted due to the associated N-Wells parasitically collecting the charge liberated by charged particles within the thin epitaxial layers.

The detection of a MIP has been successfully demonstrated using CMOS MAPS [27] technology. These allow the development of low noise, high sensitivity, radiation tolerant sensors [28] [29]. The cost per unit area of standard CMOS sensors is expected to be considerably lower than other technologies, making it possible to build a complete ECAL with silicon readout. Sensor fabrication would be more straightforward, with integrated electronics and a much wider choice of vendors leading to increased production speed and capacity with a reduced risk of having a single vendor for such a key element of the detector.

To date, no significant effort has been made to minimise the power consumption of TPAC, a characteristic which will be essential in a DECAL. Although the readout is based on ILC bunch time structure (5Hz bunch trains, each consisting of $\sim$3000 bunches separated by a few hundred ns) the timings could be optimised for alternative machines e.g the Compact Linear Collider (CLIC) [30] [31].

1.5.2 Sensor Design

To avoid saturation occurring in the sensors, a pixel size of 50×50 μm^2 was chosen for prototyping. The TPAC pixel consists of a low resistivity silicon substrate with a very thin (5–18 μm), p-doped silicon epitaxial layer grown onto the surface. The prototype sensor contains 28224 pixels in a 168×168 grid. The grid itself is segmented into four regions with each region served by a column of logic and SRAM for readout purposes, which are visible as the lighter, vertical areas in Figure 1.1. Each region of the sensor is subdivided into 168 rows of 42 pixels with each row divided into seven banks of six pixels [32]. Each pixel contains four diodes located

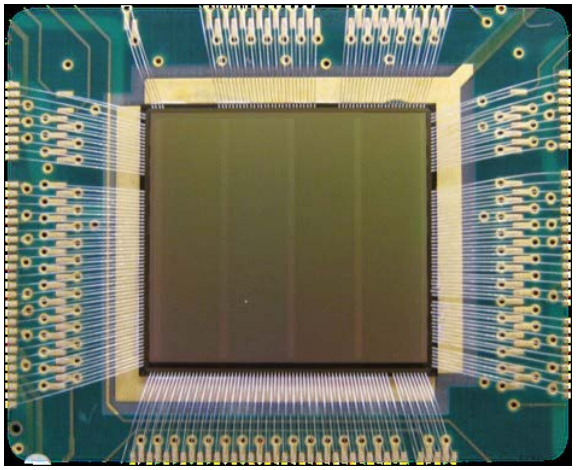

Figure 1.1: Photograph of a bonded TPAC sensor showing the four vertical regions and the columns of logic and SRAM (lighter regions) which serve them.

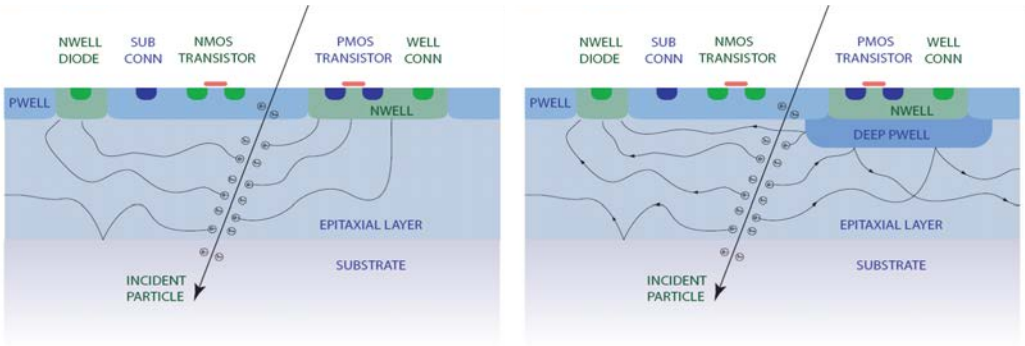

Figure 1.2: A schematic of a typical standard CMOS sensor demonstrating the charge diffusion to the diodes (left), and a CMOS sensor utilising INMAPS where the charge is repelled from the deep P-well (right).

in optimal regions of the pixel to maximise the charge collection efficiency within a pixel due to the charge diffusion between pixels, which is allowed by the lack of physical boundaries between pixels. The pixels are sampled every 400 ns and the hits are stored with the corresponding *timestamp*. There are 8192 timestamps in a *bunchtrain* before the data is read from the chip with a maximum of 19 hits allowed in each bank of six pixels.

To minimise the effect of parasitic charge collection due to the PMOS transistors, the TPAC sensors were fabricated utilising the novel INMAPS technology developed at the Rutherford Appleton Laboratory (RAL) [33]. The TPAC sensor is the first

sensor of its type to be made with the INMAPS technology. A schematic of the cross section of a regular CMOS sensor and a CMOS sensor with an INMAPS implant are shown in Figure 1.2. The INMAPS technology consists of a P-Well implant which surrounds the N-Wells associated with the PMOS components. When a particle traverses the epitaxial layer ionisation occurs which creates electron–hole pairs which drift through the silicon until they are either collected or recombine. When the charge drifts towards the INMAPS implant the positive holes, which would be collected at the N-Wells, are repelled back into the epitaxial layer by the positive charge, reducing the parasitic charge collection. The benefits to charge collection and pixel efficiency have been successfully demonstrated [34] [35]. Therefore, the INMAPS process allows full CMOS technology to be used whilst maintaining sensor performance. The INMAPS process also allows sensors to be fabricated with a high-resistivity epitaxial layer.

There are four available variants to the TPAC sensor:

- 12 μm standard epitaxial layer without INMAPS,
- 12 μm standard epitaxial layer with INMAPS (referred to as "standard" in this thesis),
- 12 μm high-resistivity epitaxial layer with INMAPS, and
- 18 μm high-resistivity epitaxial layer with INMAPS.

1.5.3 Pixel Circuit Layout

The layout of the TPAC pixel circuitry is illustrated in Figure 1.3.

In total there are 160 transistors, 27 capacitors, and a single large resistor in each pixel. To maximise the charge collected within the hit pixel there is a diode in each quadrant of the pixel, giving a total of four diodes per pixel. The four diodes are

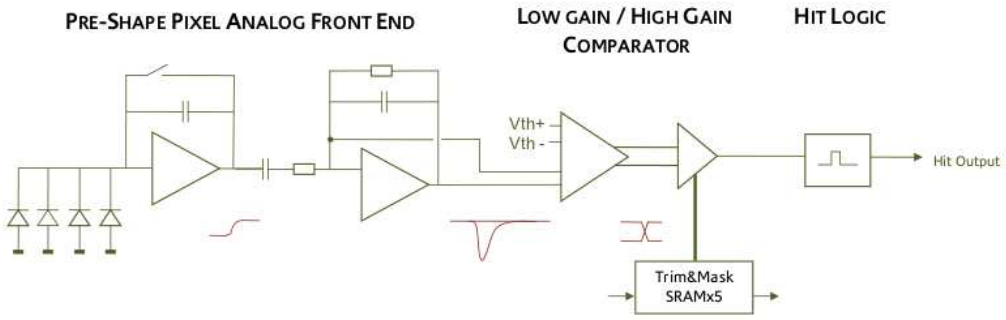

Figure 1.3: Illustration of the pre-shaper circuitry within the TPAC pixels.

connected to a pre-amplifier which generates a voltage output which is proportional to the size of the total collected charge.

The voltage is passed to a CR–RC shaper circuit which generates a pulse size proportional to the input voltage. The reset time of the shaper circuit between successive events is governed by the size of the signal up to 2500 $e^-$where the system saturates and the reset time becomes non linear. The expected signal size within the epitaxial layer for a MIP, at nominal incidence, is 1200 e^-. Simulations have demonstrated a reset time of $\sim$12 ns for a signal of 2500 e^-.

The comparator system consists of two comparators, one which provides a small gain and the other a large gain. The small gain comparator has four input voltages; the voltage from the shaper circuit, a voltage equal in size to the global pedestal, and two reference voltages which originate from the same source. The signal from the shaper circuit and threshold are corrected for the reference voltages to reduce the impact from noise in the electronics. The comparator then outputs the difference of the signal and threshold with a small gain. This output signal is then passed to the second comparator, alongside the global pedestal, where it is adjusted for pixel by pixel trims. The output of the second comparator has a high gain which saturates when the signal is greater than the trim adjusted pedestal in a pixel. A flag is set when this happens which trips a monostable circuit with a design reset time of 400 ns leading to an output signal with a constant time, independent of the

excess charge collected above threshold. The pixel is sampled every 400 ns and, if the monostable circuit is active, a hit is recorded in the memory buffer to be read out at a later time.

The output from the second comparator can be completely suppressed by setting a mask flag in the configuration buffer which effectively turns off the pixel and ensures that it never fires. This is useful to suppress any pathologically bad pixels.

1.5.4 Pixel Configuration and Readout

Each row of 42 pixels is connected to logic and SRAM registers located on the left-hand side of each row with a width of 250 μm.

The pixel configuration settings including the individual trim values and mask flags are loaded into the SRAM registers when the sensors are first initialised. The configuration settings are loaded into the registers through a serial interface where the data is loaded across a single row into the correct columns and moved down the columns into the correct row as illustrated in Figure 1.4. The configuration settings can be monitored in two places:

- at the end of the first row to check for errors loading across a row, and
- at the end of the final row to check for errors loading down the columns.

The row logic monitors the individual hit outputs from the pixels within the row and writes the details of the hits into the SRAM registers for readout at the end of a bunchtrain. There are 19 SRAM registers which can be filled allowing a maximum of 19 hits in each row per bunchtrain to be collected. When a hit is recorded the logic moves onto the next register and once all of the registers are full a flag is set to stop the collection for the particular row in question in order to preserve the collected hits. In order to relax the 19 hit limit, each register is capable of storing the information of a bank of six pixels with additional bits of information

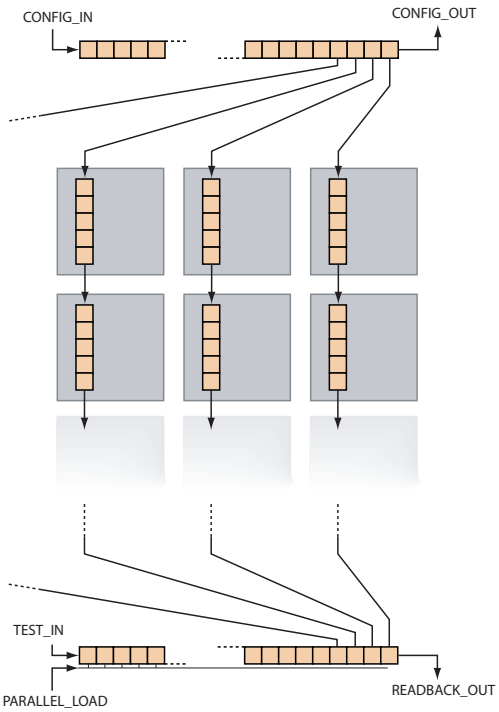

Figure 1.4: A schematic for the loading of configuration settings into the shift register where the data is written on at the top left, shifted across the top row and then shifted down each column to be readout at the bottom right at the end of data taking.

controlling which pixel in the bank fired. This is essential in dense showers where multiple neighbouring particles could fire causing the rapid filling of the register. Each register contains 22 bits of information and there is a total of 12,768 SRAM registers per sensor.

At the end of each bunchtrain the rows are scanned sequentially for rows of logic with registered hits. When a row with hits is found the SRAM register is read out in reverse order to write the data to disk. Each row logic contains a 9 bit ROM cell which adds a unique ID to the hits containing the row number. A total time of 2.6 ms is required to readout a sensor in which all rows of logic have been completely filled with 19 hits, yielding a total data size of 50 kBytes.

CHAPTER 2

The International Linear Collider and International Large Detector

2.1 International Linear Collider

2.1.1 Introduction

The ILC is a proposed future HEP facility which will precisely measure the properties of the SM and search for new physics beyond the SM. The ILC will consist of two linear accelerators which will collide bunches of electrons and positrons. In a collision between an electron and a positron the two particles annihilate and all of their energy is available to create new particles. This leads to a highly tuneable machine where the conditions of the collisions are known with a high precision. This is in contrast to a hadron collider, where the actual energy of the collisions are uncertain because the constituents of the hadrons which interact carry a poorly defined amount of the

energy. Hadron colliders are historically used to discover new particles due to the higher energies available in the collisions whereas e^+e^- colliders are used for precise measurements due to the cleaner initial environment. An example of this is the discovery of the W boson at the Super Proton Synchrotron (SPS) [36] [37] with the precise measurements of its properties taken at LEP [38]. With the discovery of the Higgs boson at the LHC, the logical next step would be to construct a lepton collider to determine its properties with greater precision.

The maximum energy available in a circular e^+e^- collider such as LEP is limited by the circumference of the accelerator and the available accelerating power to compensate for the huge amounts of synchrotron radiation which the leptons suffer during acceleration. At the end of running at LEP the accelerator was pushed to the limit in an attempt to discover the Higgs boson. Even with a circumference of 27 km, the centre of mass energy was not great enough to produce the boson and LEP was only able to set a lower limit on the mass of 114.4 GeV/c^2 [14]. In contrast, at a linear collider, where the electrons do not emit synchrotron radiation, the maximum energy of the collisions only depends on the length of the accelerators and the accelerating gradient of the RF cavities. Unlike a circular accelerator, where the circumference is fixed, if a higher centre of mass is required the linear accelerators can be extended relatively simply.

2.1.2 Physics Potential

The physics potential of the ILC is vast and varied due to the tuneable centre of mass energy. With the discovery of the Higgs boson with a mass around 125 GeV/c^2, the most likely run plan would be an initial phase with $\sqrt{s}$=250 GeV to create a "Higgs factory". This will create a huge number of Higgs bosons to allow a precise measurement of its mass, followed by a second phase at $\sqrt{s}$=500 GeV to measure the couplings of the Higgs and a potential final phase of $\sqrt{s}$=1 TeV to maximise the vector boson fusion production method of the Higgs. For completeness, the physics potential of various processes with $\sqrt{s}$=91 GeV–1 TeV will be discussed.

Z Boson Production

Collisions at $\sqrt{s}$=M_Z would allow the detectors at the ILC to collect vastly more Z boson events than was achieved at LEP. This would lead to ultraprecise measurements of the Z boson and the electroweak sector including its mass, couplings to other particles, and for rare processes where measurements at LEP had been limited by statistics.

W Boson Production

The most precise measurement of the W boson mass could be carried out by studying the centre of mass energy dependence of the cross section for $e^+e^- \rightarrow W^+W^-$ in the vicinity of the pair production threshold, $\sqrt{s} \sim 2M_W$. This significantly reduces the experimental uncertainties associated with kinematic reconstruction of the W boson decay products.

Higgs-strahlung and the Higgs Couplings

At $\sqrt{s}$=250 GeV the cross section of the "Higgs-strahlung" process ($e^+e^- \rightarrow ZH$) where the electron and positron annihilate to create a Z boson which radiates a Higgs boson becomes maximal. This is the lowest energy at which a large number of Higgs bosons would be produced in a very clean environment and would allow precision measurements of the Higgs mass and couplings to the Z boson and light fermions. In addition, the shape of the cross section around 250 GeV will allow a measurement of the spin and parity of the Higgs.

The expected precision on the product of cross section and branching ratios of a Higgs with a mass of 125 GeV are presented in Table 2.1.

Table 2.1: Expected uncertainty on the product of the cross section and branching ratios of a Higgs with mass of 125 GeV at various $\sqrt{s}$, and integrated luminosities, $\mathcal{L}$, at the ILC, from [39]

	$\Delta(\sigma.\mathrm{BR})/(\sigma.\mathrm{BR})$ [%]				
$\sqrt{s}$ and $\mathcal{L}$ (P_{e^-},P_{e^+})	250 fb^{-1} @ 250 GeV (-0.8,+0.3)		500 fb^{-1} @ 500 GeV (-0.8,+0.3)		1 ab^{-1} @ 1 TeV (-0.8,+0.2)
mode	ZH	$\nu\bar{\nu}H$	ZH	$\nu\bar{\nu}H$	$\nu\bar{\nu}H$
H$\to b\bar{b}$	1.1	10.5	1.8	0.66	0.47
H$\to c\bar{c}$	7.4	-	12	6.2	7.6
H$\to gg$	9.1	-	14	4.1	3.1
H$\to WW*$	6.4	-	9.2	2.6	3.3
H$\to \tau^+\tau^-$	4.2	-	5.4	14	3.5
H$\to ZZ*$	19	-	25	8.2	4.4
H$\to \gamma\gamma$	29–38	-	29–38	20–26	7–10
H$\to \mu^+\mu^-$	100	-	-	-	32

Higgs Production Through Vector Boson Fusion

The vector boson fusion production cross section of the Higgs boson occurs when the electron and positron each emit a W or Z boson which fuse to create a Higgs. In the dominant case of WW fusion, the final state consists of a Higgs and two neutrinos whereas the ZZ fusion consists of the beam electron and positron and a Higgs. The beam leptons generally escape detection close to the beam axes leading to an observed signal of just a Higgs decay in the detector for both channels.

The cross section of vector boson fusion increases with $\sqrt{s}$ and becomes dominant over the Higgs-strahlung process above 450 GeV. With an upper limit of 1 TeV in the collisions, vector boson fusion can be studied over a wide range of energies to yield accurate measurements of the Higgs couplings to fermions and gauge bosons. The predicted branching ratios for WW fusion are also presented in Table 2.1.

In a model without the Higgs boson, the cross section of WW scattering (WW fusion where the Higgs decays to two W's) is predicted to increase rapidly and violate unitarity. Should the Higgs boson discovered at the LHC prove not be a SM Higgs boson, it would be essential to study this process at these higher energies to search for physics beyond the SM.

Top Quark Threshold Scan

Around $\sqrt{s}$=350 GeV there is an enhancement in the total cross section where the threshold energy to produce two top quarks is exceeded. A dedicated threshold scan of the $t\bar{t}$ cross section would allow a measurement of the top quark mass with a precision of 100 MeV and allow a greater understanding of the shape of the $t\bar{t}$ mass distribution. An understanding of this distribution is essential as the $t\bar{t}$ process will act as a background to many physics studies at higher $\sqrt{s}$ and the systematics arising from the $t\bar{t}$ shape must be minimised.

Top Higgs Yukawa Coupling

The Yukawa coupling to the top quark is the strongest and any perturbations from the SM would be an indication of new physics so it is important to minimise the uncertainty on this process.

The direct measurement of the Higgs Yukawa coupling to the top quark is kinematically allowed above energies of ∼470 GeV (M_t+M_t+M_H). Around 500 GeV the cross section is increased slightly due to bound state effects making it possible to measure the strength of the coupling [40] [41].

At $\sqrt{s}$=800 GeV the cross section of $e^+e^- \rightarrow t\bar{t}H$ becomes maximal. However, the dominant background of $t\bar{t}$ decreases with increasing $\sqrt{s}$ and at $\sqrt{s}$=1 TeV it is possible to measure the Higgs Top Yukawa coupling with a precision of 4% (see Chapter 5).

2.1.3 Accelerator

The current agreed layout of the ILC is shown in Figure 2.1. The ILC will consist of an electron source, a positron source, and two damping rings, which will reduce the phase space and emmitance of the electron and positron beams prior to entering

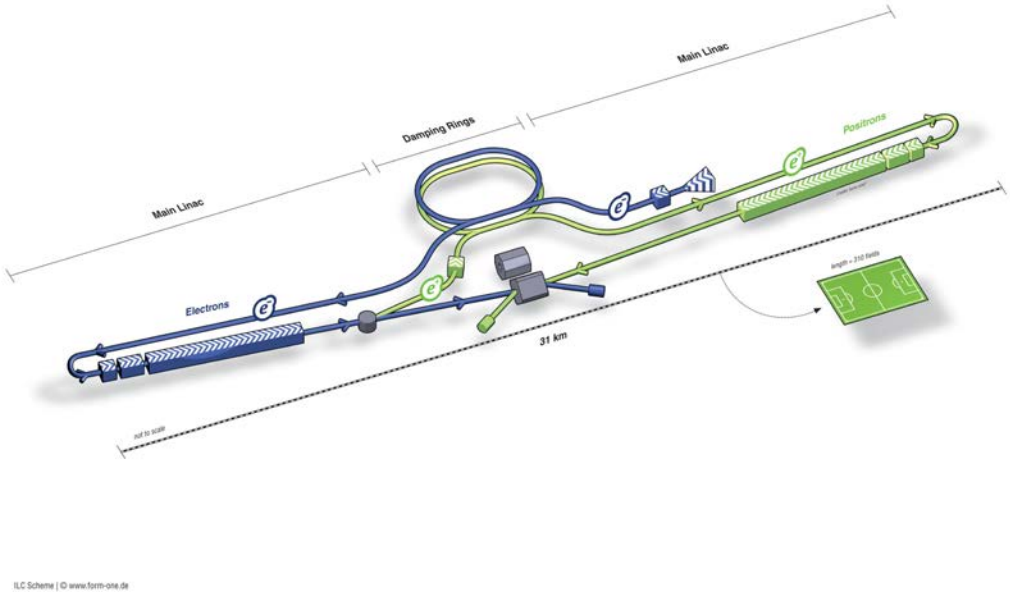

Figure 2.1: Layout of the ILC taken from [42]

the main linear accelerators, which will accelerate the particles to maximum energy before being tightly focused and collided at the Interaction Point (IP). The site length is 31 km for $\sqrt{s}$=500 GeV with each linac being 11 km in length. The linac lengths will double for $\sqrt{s}$=1 TeV.

The proposed beam parameters at various centre of mass energies are presented in Table 2.2.

Electron Source

The electrons are produced by illuminating a GaAs photocathode in a DC gun with a laser. The liberated electrons will have at least an 85% polarisation with a minimum of 80% required for the proposed physics plan at the ILC. The electrons are produced in bunches of 1 ns which are then compressed down to 20 ps and accelerated via gradients of 8.5 MV/m to increase the beam energy to 76 MeV. The beam is then injected into a linac system which accelerates the beam to 5 GeV before it is passed into the damping ring.

Table 2.2: ILC proposed beam parameters for running at $\sqrt{s}$=250 GeV–1 TeV from [43]

Parameter	Unit	$\sqrt{s}$ [GeV]		
		250	500	1000
Beam Energy	GeV	125	250	500
Collision Rate	Hz	5	5	4
Number of Bunches		1312	1312	2450
e^- / bunch	10^{10}	2.0	2.0	1.74
e^+ / bunch	10^{10}	2.0	2.0	1.74
Bunch separation	ns	554	554	366
e^- polarisation	%	80	80	80
e^+ polarisation	%	30	30	20
β_h @ IP	mm	13.0	11.0	11.0
β_v @ IP	mm	0.41	0.48	0.23
Luminosity	10^{34} cm^{2}s^{-1}	0.68	1.47	4.32

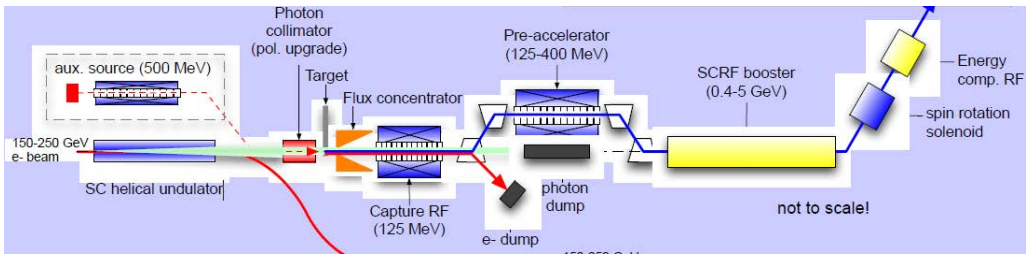

Figure 2.2: Layout of the positrons source system as presented here [44].

Positron Source

The positrons are created using the main electron linac beam. The electrons are passed through an undulator which causes them to radiate photons which interact with a thin metal target to create an electromagnetic shower. The positrons are then captured using a momentum selection RF system prior to acceleration to 400 MeV. The 400 MeV positrons are then accelerated in a similar fashion to the electron beam up to 5 GeV before entering the damping ring. The layout of the components required to achieve this is shown in Figure 2.2.

Damping Rings

The damping ring system consists of two storage rings located at the centre of the ILC site, each with a circumference of 3.2 km [45]. The goal of the damping rings is to form the required bunch structure before the beams are passed to the main linacs, and to reduce the emittance of the bunches to maximise the luminosity. Each ring will contain 1312 bunches with each bunch consisting of 2×10^{10} particles which will be compressed to a horizontal emittance of 0.57 nm and a vertical emittance of 2.00 pm.

Each ring consists of two straight 710 m sections and two arc regions to complete the ring. In addition to the kicker to extract the beam when it is required, the straight sections contain the required wigglers to reduce the emittance and an RF cavity to ensure the beam energy remains at 5 GeV after each loop.

When the beam is required, the particles are extracted from the damping ring into the Ring to Main Linac system, which is a 15 km long beampipe with a 180° turn-around section which aids with beam stabilisation.

Main Linacs

The main linacs will accelerate the beams of electrons and positrons up to the desired collision energy. The linacs will utilise 1.3 GHz superconducting technology with an accelerating gradient of 31 MV/m. To achieve this the linacs will consist of nine-cell niobium cavities cooled via liquid helium to 2 K. The total length of each linac will be determined by the desired energy. At $\sqrt{s}$=500 GeV the positron linac will consist of 278 RF units and the electron linac of 282 RF units to compensate for the energy lost through the undulators [46].

Interaction Region

At a linear collider there is a single IP after which the particle beams are directed to beam dumps. It is essential to have an efficient method of delivering the beams to the IP. This is achieved via the Beam Delivery System.

The Beam Delivery System refocuses the beams from the linacs until their emittance is sufficiently small to achieve the required luminosity before colliding the beams and transporting the spent beams to the beam dumps. The linacs are arranged with a crossing angle of 14 mrad and the beams are deflected via a series of crab cavities to allow a horizontal crossing angle [46]. Following collisions, the energy spread of the beam can be large and a robust method of safely removing the beam will be required to prevent damage to the accelerator and detector. The complete system needs to be designed with "push-pull" capabilities such that the two detectors (ILD and the Silicon Detector (SiD)) can be swapped into place at the single IP.

2.1.4 Location

The costs associated with the construction and running of the ILC complex and detectors will far outweigh the capabilities of any single country in the World and funding will need to be on an international basis. Due to this, the potential location for the ILC has not yet been set with sample sites proposed in America, Europe and Asia. However, all of the sites will need to match the same basic criteria:

- be sufficient in length to achieve $\sqrt{s}$=1 TeV (>50km),
- have less than a 100m change in elevation over the whole length,
- not be near any known fault lines of earthquake zones for stability,
- be able to provide all the required power to site, and
- be less than 20 km from towns and close to international links.

The sample sites range from mountainous regions in Japan, which will require horizontal access to the detectors, to conventional tunnels buried deep underground, which require vertical access, to shallow tunnels. The choice of location and therefore the access method will affect all aspects of the construction procedure including the design of the detectors and how and where they are constructed.

2.2 International Large Detector

2.2.1 Introduction and Motivation

The ILD [23] [47] is one of two multi-purpose detector concepts, the other being SiD, designed to be used at the ILC [48]. The ILD concept is based on the GLD [49] and LDC [50] detector concepts. There is also a variant of ILD for use at CLIC [31], with the detector systems modified to accommodate the higher energies.

The demanding physics programme at the ILC, including the precision measurements of the Higgs boson, top quark and heavy flavour physics, as well as measuring the properties of the W and Z bosons, places stringent requirements upon the ILD. In particular, the ILD will need to:

- be fully hermetic,
- have minimal material budget before the calorimeters to enable the use of Particle Flow Algorithms (PFAs),
- have a jet energy resolution, σ_E/E, less than $30\%/\sqrt{E[GeV]}$ to distinguish between the kinematically reconstructed decay products of W and Z bosons in an event,
- have a momentum resolution of $\delta(1/p_T) \approx 2 \times 10^{-5}/GeV/c$,
- have compact calorimeter systems,

- accurately flavour tag the jets, and
- reconstruct complex final states, including a large number of jets, leptons and missing energy.

To achieve this, ILD adopts the typical cylindrical "onion layer" design used by the majority of HEP detectors past and present from ALEPH [51] and OPAL [52] at LEP, to D0 [53] and CDF [54] at the Tevatron, to ATLAS [55], CMS [56], and ALICE [57] at the LHC.

The layout of ILD is illustrated in Figure 2.3 and Figure 2.4. Closest to the beamline are high precision pixel Vertex Tracker (VTX) sensors, followed by a Time Projection Chamber (TPC) sandwiched between the Silicon Inner Tracker (SIT) and Silicon External Tracker (SET). The ECAL and the HCAL complete the detector, which is housed inside a large solenoid producing a 3.5 T magnetic field. Finally, outside of the magnet are the return yokes which act as the muon systems. It was essential to keep the calorimeter systems within the magnet to minimise the amount of material through which particles pass and separate charged and neutral particles before the calorimeters to allow the use of PFAs and achieve the required jet energy resolutions.

The basic concepts of ILD have been decided and baseline technology for all of the detector elements has been developed. However, the final technology choices have not been made for various systems. In keeping with the R&D nature of this thesis, the current options will be described whilst expanding on the required properties of each subsystem of the detector.

2.2.2 Particle Flow Calorimetry

In a conventional calorimeter system the jet energy is calculated by summing the energy deposited in the ECAL and HCAL and then scaling this figure by the relative sampling fraction. This leads to typical jet energy resolutions of $60\%/\sqrt{E[GeV]}$ meaning the traditional methods of calorimetry are not appropriate at the ILC. In

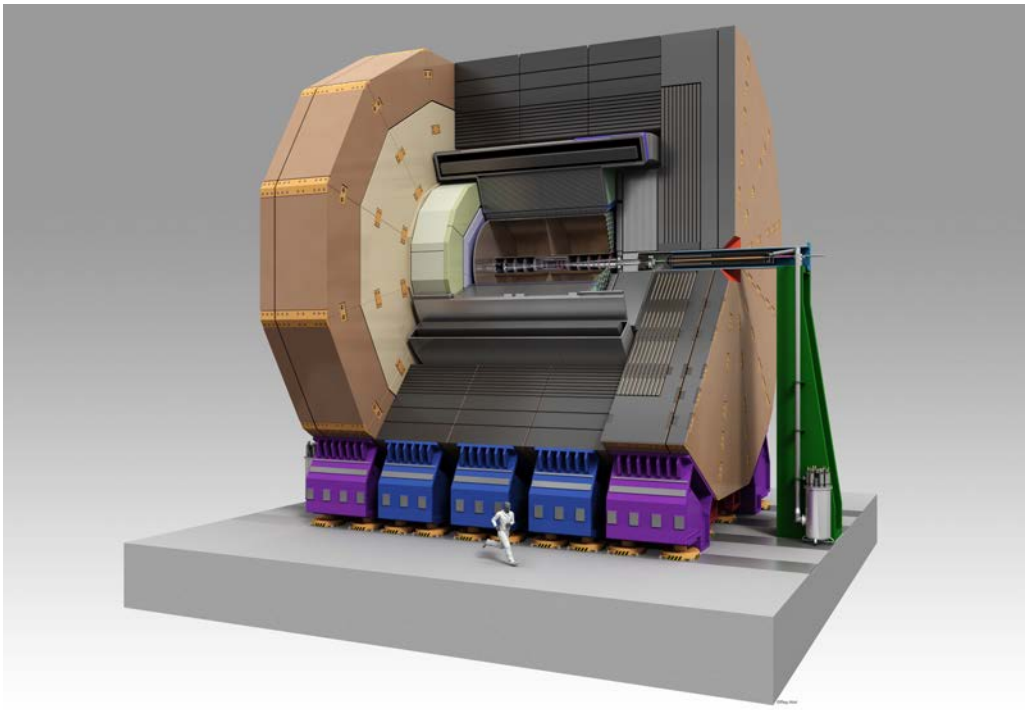

Figure 2.3: Isometric view of the ILD [23].

order to achieve the required jet energy resolutions an alternative method known as particle flow calorimetry has been proposed. The most advanced implementation of which is the Pandora Particle Flow Algorithm (PandoraPFA) [58].

Particle flow calorimetry relies on reconstructing the four vectors of the individual particles within a jet, the sum of which yields the properties of the jet. The energy and momenta of the charged particles are measured with high precision using the tracking systems whereas the neutral components are measured by the calorimeter systems. To achieve this final step, highly granular calorimeter systems are required to separate the photons and neutral hadrons from the charged particles to avoid confusion during reconstruction. There are two sources of possible confusion:

- if a neutral cluster within the calorimeters cannot be resolved from the clusters associated with charged particles then the photon's energy is lost in the reconstruction, or
- if a charged cluster is not associated with a charged track then the energy will

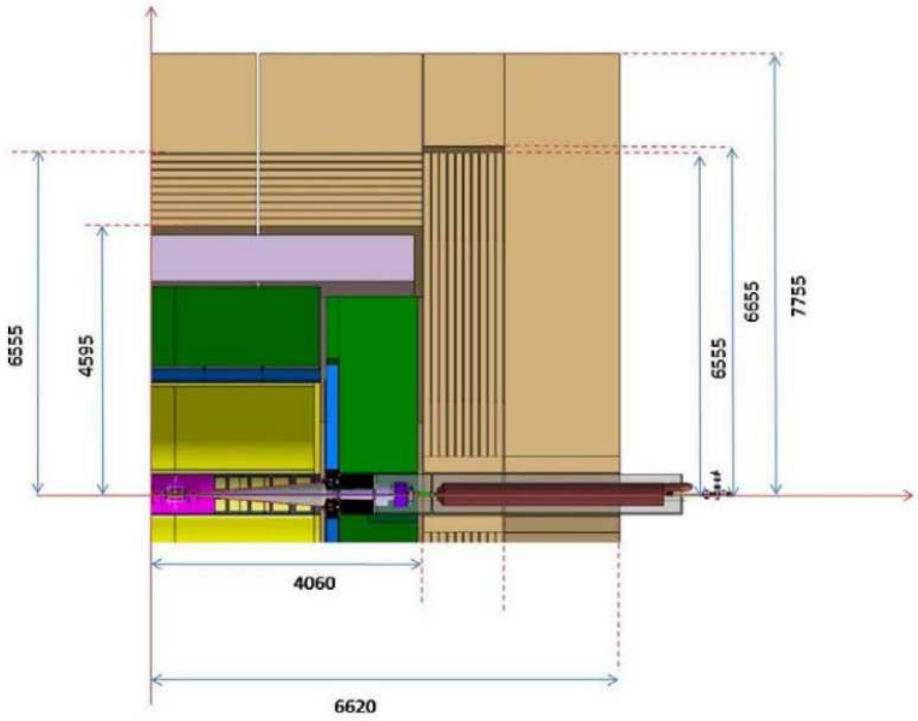

Figure 2.4: One quadrant of the ILD with the silicon tracking system shown in pink; the TPC in yellow; the ECAL in blue; the HCAL in green; the Solenoid in light pink, and the return yoke and muon system in brown. All distances are quoted in units of mm [23].

be double counted.

The overall jet energy resolution within a particle flow calorimeter is therefore a combination of the detector and PFA performance. There are multiple stages to the PandoraPFA clustering and reconstruction and these are summarised below.

Firstly, reconstructed tracks are selected and identified as single charged particles, pairs of tracks from a neutral particle decay, and kinks and prongs within the tracking volume on the basis of their projected start and end positions. The energy and location of all hits within the calorimeters are converted into MIP signals, with any hits below the MIP threshold being neglected. Isolated hits, which may be caused by neutrons in a shower, are removed to improve the performance as they are impossible to associate with a jet due to the potentially large separation of the neutrons and the jets. The remaining MIP signals are then converted back into calorimeter energy

deposits and clustered using various algorithms which utilise the track positions on the entrance of the calorimeters as a seed. The clustering algorithm continues until all of the hits are formed into clusters. Clusters associated with tracks are tagged as charged clusters while unassociated clusters are tagged as neutral. The clustering algorithm is designed to produce clusters which are smaller in size than the true size to avoid incorrectly associating neutral clusters with charged clusters. Neutral clusters which actually belong to a charged cluster are located and amalgamated into the relevant charged cluster via a dedicated cluster merging algorithm.

The charged cluster energies are then compared with the momenta of the associated track to ensure that overlapping clusters and jets have not been merged into one cluster at higher energies. If a situation arises where the cluster energy is much greater than the track energy the cluster is split up and reclustered with different parameters to the clustering algorithm until all of the cluster energies are in good agreement with the track momenta. The neutral clusters are checked for consistency with photons on the basis of their energy profiles and any remaining non-photon neutral clusters are classed as fragments and are merged with charged clusters dependent on the distance between them.

Finally, the Pandora Particle Flow Objects (PandoraPFOs) are created by allocating clusters to the tracks based on the distance of closest approach.

2.2.3 Vertex System

The identification of charm and bottom quarks within ILD is essential to reconstruct short lived particles such as D or B mesons. The VTX system will require a spatial resolution of better than 3 μm and will consist of six sensors, arranged in back-to-back pairs approximately 2 mm apart with an inner radius of 16 mm and outer radius of 60 mm. To minimise the amount of material traversed by the particles before reaching the tracking systems, each layer is limited to a thickness of just 0.15 % χ_0. The parameters of the vertex system as outlined here [23] are shown in

Table 2.3: The ILD vertex detector parameters as outlined here [23] where the resolutions and readout times are estimated from the CMOS sensor option.

	R [mm]	$\|z\|$ [mm]	$\|\cos(\theta)\|$	σ [μm]	Readout time [μs]
layer 1	16	62.4	0.97	2.8	50
layer 2	18	62.5	0.96	6	10
layer 3	37	125	0.96	4	100
layer 4	39	125	0.95	4	100
layer 5	58	125	0.91	4	100
layer 6	60	125	0.90	4	100

Table 2.3. The inner two layers are half the length of the other four to reduce the number of hits arising from background events.

There are currently three sensor technologies under consideration for the VTX detectors. The MIMOSA-26 sensor, a CMOS based sensor with a sensitive thickness of 10–20 μm and a pitch of 18.4 μm, has demonstrated the required properties of the VTX system [59]. Fine Pixel CCD (FPCCD) sensors could offer a reduced pixel size of just 5 μm in the first two layers and 10 μm in the other four sensors but must be operated at -40^{o}C to suppress the radiation damage within the sensors. The third option is DEPFET active sensors which demonstrate an excellent S/N ratio [60] but the current row readout time of 80 ns, equating to a sensor readout time of 200 μm, needs to be reduced.

2.2.4 Silicon Tracking System

The silicon tracking system consists of four parts:

- the SIT, which consists of four strip sensors, is located between the VTX detectors and the TPC and aids in the track matching between the VTX points and the TPC tracks to improve spatial resolution,
- the SET, which consists of two strip sensors and is located between the TPC and ECAL to give an accurate position of the tracks before entering the ECAL,

- the Endplate TPC Detector (ETD) behind the endplate of the TPC, used to measure accurately any tracks going through the endplate, and
- the Forward Tracking Detector (FTD) which consists of seven disks between the beampipe and the TPC.

The parameters for the silicon tracking system, split into individual components, are shown in Table 2.4. The SIT, SET, and ETD requirements can be achieved via basic silicon strip sensors. However, there is a significant R&D effort to achieve thin, edgeless sensors with a low material budget and integrated electronics to minimise the associated dead areas. The FTD consists of 7 disc sensors. The first two of these are highly granular pixel sensors with pixel sizes from 26×29 μm^2 in order to cope with the high multiplicities of forward jets and beam related backgrounds. As with the VTX tracker, the options for the first two layers consist of CMOS, FPCCD, or DEPFET sensors. The five remaining layers will be formed from silicon strip detectors due to their excellent R–ϕ resolutions and the expected reduction in occupancy of these sensors.

2.2.5 Time Projection Chamber

The central tracking system of ILD is a TPC. A TPC is a large gas filled detector in which the ionised gas molecules from charged particle interactions drift to endplates where the charge is collected and read out. A TPC offers many of the desired detector design goals including:

- excellent three-dimensional tracking capabilities,
- a low material budget before the calorimeters,
- the ability to handle large multiplicity events,
- low cost of production, and

Table 2.4: The ILD silicon tracker detector parameters as outlined in [23], split into individual components.

SIT characteristics				
Geometry			Characteristics	Material
R [mm]	$\|z\|$ [mm]	$\|\cos\theta\|$	Resolutions R-ϕ [μm]	χ_0 [%]
153	368	<0.910	R: σ=7.0	0.65
300	644	<0.902	x: σ=50.0	0.65
SET characteristics				
Geometry			Characteristics	Material
R [mm]	$\|z\|$ [mm]	$\|\cos\theta\|$	Resolutions R-ϕ [μm]	χ_0 [%]
1811	2350	<0.789	R: σ=7.0	0.65
ETD characteristics				
Geometry			Characteristics	Material
R [mm]	$\|z\|$ [mm]	$\|\cos\theta\|$	Resolutions R-ϕ [μm]	χ_0 [%]
419.3–1822.7	2420	0.985–0.799	x: σ=7.0	0.65
FTD characteristics				
Geometry			Characteristics	Material
R [mm]	$\|z\|$ [mm]	$\|\cos\theta\|$	Resolutions R-ϕ [μm]	χ_0 [%]
39–164	220	0.985–0.802	σ=3–6	0.25–0.5
49.6–164	371.3	0.991–0.914	σ=3–6	0.25–0.5
70.1–308	644.9	0.994–0.902	σ=7.0	0.65
100.3–309	1046.1	0.994–0.959	σ=7.0	0.65
130.4–309	1447.3	0.995–0.998	σ=7.0	0.65
160.5–309	1848.5	0.996–0.986	σ=7.0	0.65
190.5–309	2250	0.996–0.990	σ=7.0	0.65

- the potential to achieve a momentum resolution of $\delta(1/p_T) \approx 1 \times 10^{-4}/GeV/c$.

The ILD TPC will be over 4700 mm in length with an inner radius of 329 mm and outer radius of 1808 mm and will operate within a magnetic filed of 3.5 T. It will be filled with a gas similar to that of the one used in the T2K TPC [61] due to the favourable prototype performance with long drift times in high magnetic fields.

The endplates serve three purposes; to seal the TPC and contain the gas; to give support to the structure, and to house the read out sensors. The material budget of the endplates has to be kept below 25 % χ_0 in order to avoid degradation in the resolutions of low energy jets. The Large Prototype (LP) [62] has demonstrated the required properties to achieve this. The readout sensors are attached to the

endplates. Currently there are two options for consideration, Gas Electron Multipliers (GEMs), and Micromegas. Both of these technologies have demonstrated the required performance but there are some issues associated with each. A single GEM does not achieve the required amplification and so a stack of GEMs must be used which increases the dead space. Whilst a Micromega can achieve the required amplification and has been shown to run reliably for long periods of time, the design of the Micromega introduces a few percent dead area per sensor.

2.2.6 Electromagnetic Calorimeter

The main goals of the ILD ECAL are to identify and measure the properties of photons and electrons, separate the individual particles as required by PandoraPFA, initiate the hadronic showers, and begin the measurement of such showers. An energy resolution of better than $20/\sqrt{E}\%$ is required to allow the separation of photons a few cm apart. There are multiple parameters which need to be optimised within the design of the ECAL to achieve these goals including:

- the total depth of the calorimeter in χ_0,
- the inner radius of the ECAL,
- the number of layers within the ECAL and the thickness of the tungsten within each layer, and
- the number of readout sensors and their corresponding size.

The inner radius of the ECAL is constrained by the components between the IP and the ECAL. The large TPC sets the inner radius at $\sim$1800 mm. The cost of the calorimeter systems and magnet are the main driving forces behind the total cost of many HEP detectors. In a detector optimised for PFA the calorimeter systems must be kept within the magnet, increasing the size of the magnet and causing a sharp increase in the price of the detector. A total calorimeter depth of 24 χ_0 is required

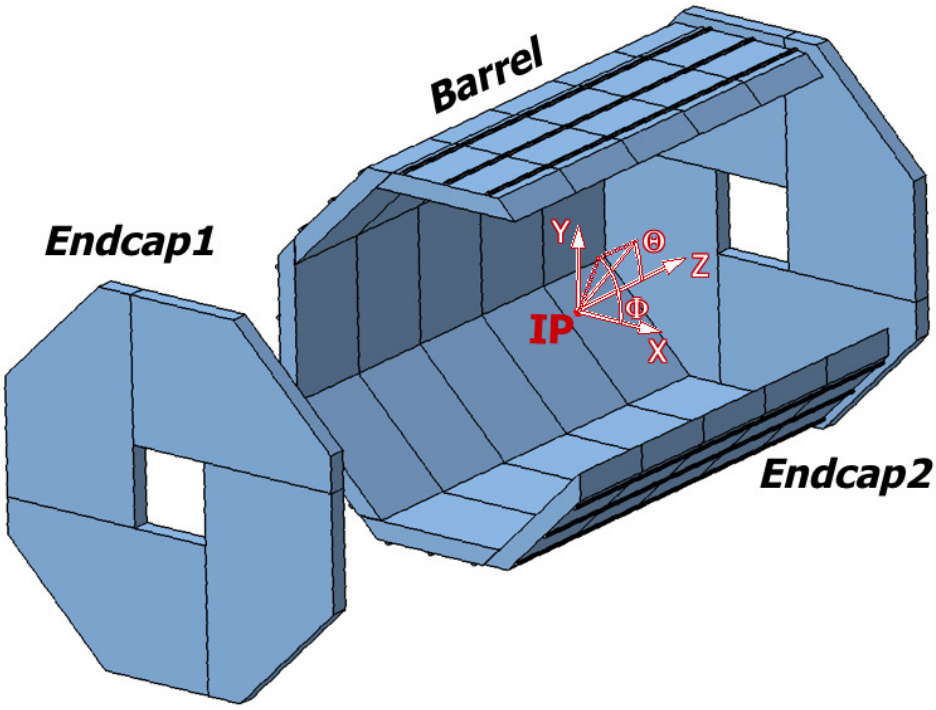

Figure 2.5: Illustration of the ECAL demonstrating the orientation of the staves within the barrel and endcaps [47].

in the barrel to fully capture the electromagnetic showers at typical ILC energies and tungsten, with a χ_0=3.5 mm, is used for the showering material to keep the calorimeter systems as compact as possible.

The complete ECAL system is composed of a central barrel region and two endcaps which slot into the ends of the barrel to achieve as fully an hermetic system as possible. The barrel consists of 29 layers of tungsten sandwiched between 30 readout layers. The first nine layers of tungsten are 2.1 mm in depth to measure accurately the start of the shower, whereas, the final 20 layers are twice the depth to achieve the required thickness. The barrel is segmented into units 1.5 m in length which are divided into eight trapezoidal staves slotted together to make a ring (see Figure 2.5). In this design, the dead areas from the joints between the modules are uncorrelated and do not face the interaction point.

The Molière radius of tungsten is 9 mm. Therefore, to achieve the required separation of photons from photons, electrons from electrons, and photons from electrons the ECAL cell sizes must be smaller than this and a cell size of 5×5 mm^2 will be used in the sensitive layers. The highly granular calorimeter will require a total of 10^8 cells in the barrel and endcaps. Reading the information from this many sensors, the cooling requirements, and dead spaces associated with each cell all present potential design challenges.

The cooling requirements will be minimised by operating the calorimeter in power-pulsing mode where the sensors are only powered whilst beam is present. The power pulsing requires sensors which can rapidly switch states and R&D is currently underway to achieve this. To minimise the amount of dead space associated with each cell, it was essential to integrate as much of the sensor electronics onto the sensors and this has been a large consideration in the sensor technology options.

There are currently two sensor technologies deemed advanced enough for inclusion in the ILD Technical Design Report (TDR), silicon pad readout (SiECAL) and scintillator strips (SciECAL). There are two other technologies which, due to funding and timescales, did not make it into the TDR, these are; a hybrid of the SiECAL and SciECAL where alternate layers of each readout type is used to reduce costs, and a very finely segmented digital readout system which counts the number of particles in the showers (DECAL).

SiECAL

The proposed layout for a SiECAL layer is shown in Figure 2.6(a) where the silicon wafer is bonded onto a PCB and inserted between two layers of tungsten. The required granularity of 5×5 mm^2 and sensor thickness can easily be achieved using silicon wafers. The silicon wafers have a resistivity of 5 kΩcm and require a depletion voltage of 100–200 V.

A large physics prototype containing 30, 18×18 cm^2 layers with cell sizes of 1×1 cm^2,

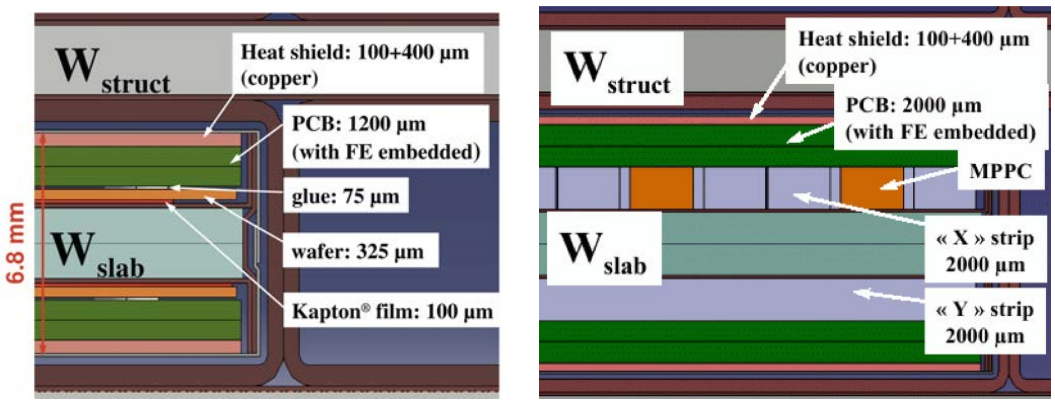

(a) SiECAL module (b) SciECAL module

Figure 2.6: Cross section of a layer within the SiECAL and SciECAL including the tungsten absorbing material, PCB, sensors and readout infrastructure [23].

has been tested at various beam tests and has achieved an electron resolution of $16.6/\sqrt{E[\text{GeV}]}\oplus 1.1\%$ [63].

Whilst the proposed technology has demonstrated capabilities to distinguish two particles from small energy deposits the SiECAL sensors are costly to produce and with a proposed active area of 3000 m^2 a complete SiECAL will be very expensive. In simulations the SiECAL is the default option.

SciECAL

The SciECAL will use strips of scintillators which are 5 mm wide and 45 mm long separated by layers of tungsten. A typical layout for a SciECAL layer is shown in Figure 2.6(b). Alternating strip layers will be arranged orthogonal to each other giving an effective pixel size of 5×5 mm^2. A wavelength shifting fibre will be enclosed in a groove along the strip and the MPPC photosensor embedded into the scintillating strip in such a way where there is only 1.9% dead area.

A physics prototype with 30 layers and a total of 2160 strips, with an equivalent pixel size of 1×1 cm^2, has been exposed at beam tests and has demonstrated an electron energy resolution of $15.1/\sqrt{E[\text{GeV}]}\oplus 1.4\%$ [64].

The use of scintillator strips will reduce the total cost of the ECAL compared to the silicon option. The use of MPPCs demand that the strips must be at least 1 mm deep to generated the require number of photons and accommodate the size of the sensor. If the number of layers is assumed to be the same as for the SiECAL then the outer radius of the SciECAL must increase thus making the HCAL and magnet systems larger and increasing the cost of these modules.

Hybrid

The hybrid ECAL is an option which uses a combination of the silicon wafers and scintillator strips to reduce the cost of the ECAL by restricting the use of the expensive wafers to the essential regions of the ECAL. Various models have been studied using alternate layers of wafers and strips and the wafers for a certain fraction at the front of the ECAL with the backend of the ECAL filled with strips. Work presented here [65] suggests that with a fraction of 50% strips the integrity of the performance is preserved at a potentially reduced cost.

DECAL

Another potential option for the sensitive layers of the ECAL are binary pixel sensors to form a DECAL. The premise of the DECAL, as outlined in Section 1.4.3, is to count the number of particles in a shower rather than the energy deposited by each particle and in doing so removing some of the statistical uncertainties associated with energy deposition. Simulations of the single photon resolution have demonstrated an equivalent performance to the SiECAL option. The use of standard MAPS CMOS sensors will vastly reduce the cost of the sensitive layers of the ECAL as multiple vendors could produce them and CMOS is intrinsically less expensive than the high resistivity silicon used in the SiECAL.

The testing of a MAPS for use in the DECAL forms the basis of this thesis and results from beam tests have proven promising. However, due to severe funding

restrictions within the UK, the tests have so far only focused on single sensor tests and many of the considerations of building a working prototype have not yet been addressed.

2.2.7 Hadronic Calorimeter

In a hadronic shower there are non-negligible contributions from neutral particles, with large fluctuations from shower to shower, and an electromagnetic core. It is essential that the HCAL is able to identify both charged and uncharged particles in the showers as the energy resolution of jets with energy less than 100 GeV is dominated by the uncertainty in the fraction of neutral particles [58]. There are currently two options for the HCAL, both of which use steel as the absorbing material, but one uses scintillator tiles for the sensitive layers (known as the AHCAL) and the other uses Glass Resistive Plate Chambers (GRPC) with semi digital readout (SDHCAL).

Steel was chosen as the absorbing material as it offers the prospect of supporting the calorimeter as well as acting as the absorber material. As steel has an interaction length of 17 cm and χ_0=1.8 cm, the electromagnetic and hadronic showers develop at very different depths, thus aiding the identification and measurement of the electromagnetic core of the hadronic showers and improving the overall performance. To ensure the containment of 250 GeV jets in 1 TeV collisions, the HCAL will be 6 λ_I deep and consist of 48 layers. There are currently two designs for the HCAL structure but the detailed engineering properties are still to be established. The first design separates the barrel into two ring sections with each ring split into 16 modules and the second is similar to the ECAL with the barrel divided into five segments with eight staves. Both of these geometry options are compatible with both the AHCAL and SDHCAL readout options.

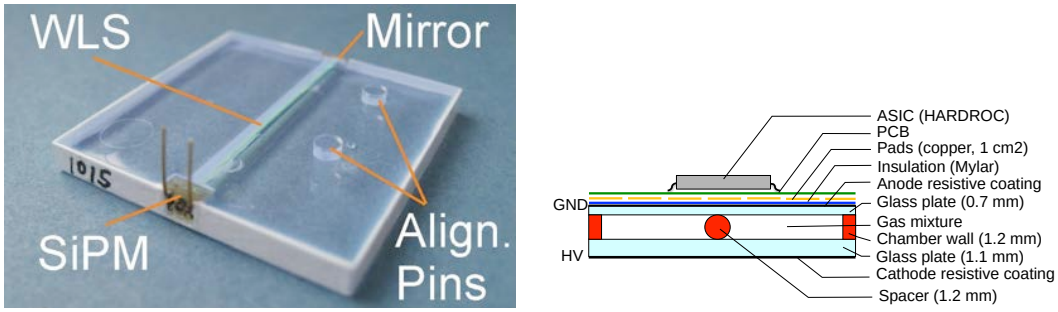

(a) AHCAL module (b) SDHCAL module

Figure 2.7: Readout tiles used within the analogue and semi digital HCAL

AHCAL

The AHCAL uses well-established scintillator technology to form 3 mm thick tiles with a surface area of 3×3 cm^2 which provide both energy and position measurements. The design of such a tile is shown in Figure 2.7(a) where the wavelength shifting fibre integrated into the tile transports the light to the embedded silicon photomultipliers (SiPM). The holes for the alignment pins to fix the tiles in place are also visible. The development of multi-pixel Geiger mode SiPMs allows the robust readout of the signals in the highly granular scintillator tiles and offer excellent MIP tracking capabilities.

The testing of a prototype with 38 layers, each with an area of 90×90 cm^2, using 5 mm thick tiles separated by 2 cm of steel at various pion beams has demonstrated a raw energy resolution of $58\%/\sqrt{E[\text{GeV}]}$ which can be reduced to $45\%/\sqrt{E[\text{GeV}]}$ with software compensation [66] [67].

SDHCAL

The SDHCAL option will use GRPCs filled with a mixture of TFE(93%), CO_2(5%), and SF_6 gas which is readily ionised when a charged particle traverses it. The signal is then read out using specially developed HARDROC ASICs mounted on a PCB [68]. Figure 2.7(b) illustrates the layout of a single GRPC including the

structure to contain the gas and the readout electronics. The GRPCs can achieve very finely segmented devices with excellent coverage.

For a digital HCAL, in the ILD, a cell size of a few mm is required to avoid saturation, leading to 10^8 readout channels. To reduce this number an extra bit of information was added to the readout and the cell sizes increased to 1×1 cm^2. The extra bit of information allows a discrimination between one, multiple, or many particles through the same cell by setting three thresholds. The addition of the extra thresholds proves vital for showers above 50 GeV where saturation becomes an issue for the binary readout [69].

2.2.8 Forward Calorimeters

To increase the coverage of the calorimeter systems and allow measurements of the luminosity to be made there will be two forward calorimeters:

- the LumiCal, which will measure the absolute luminosity to better than 10^{-3} at 500 GeV, and
- the BeamCal, which will measure the beam and provide an estimation of the luminosity.

Both calorimeters will require fast readout to deal with the high occupancy from the large number of particles from beamstrahlung and two photon processes. The BeamCal will also be exposed to radiation deposits from low angle electrons of up to 1 MGy per year and will need to be radiation hard. The forward calorimeters will use tungsten plates of thickness equal to 1 χ_0 interspersed with the sensitive layers to measure accurately the photons and electrons.

LumiCal

The sensitive layers in the LumiCal will be finely segmented silicon sensors to measure accurately the polar angle of the scattered electrons caused by the Bhabha scattering process. The cross section, σ_B, of Bhabha scattering is very well known theoretically [70] and the luminosity is given by $L = N_B/\sigma_B$ where N_B is the numbered of measured events. The LumiCal is divided radially into 64 parts, each with an equivalent angular size of 0.8 mrad, yielding a polar angle resolution of $(2.2\pm0.01)\times10^{-2}$ mrad [71]. The LumiCal will be 30 χ_0 deep and achieve an energy resolution of $(0.21\pm0.02)/\sqrt{E[\text{GeV}]}$.

BeamCal

Polycrystaline CVD diamond sensors and gallium arsenide (GaAs) sensors have been irradiated with a 10 MeV electron beam to evaluate the effects of radiation. The performance of the diamond sensors is maintained up to doses of 7 MGy whereas the GaAs sensors show a dramatic drop in the charge collection efficiencies for the same dose. The design of the BeamCal has not been finalised but a design with the more expensive diamond sensors, close to the beampipe fanning out into the lower cost GaAs sensors, is expected to take precedence.

2.2.9 Magnet

The ILD magnets will need to produce a 3.5 T (potentially 4 T) solenoidal field over a cylindrical volume 6.88 m in diameter and 7.35 m in length. This will be achieved using a superconducting solenoid divided into three equal sized modules. The inner coil radius will be 3615 mm from the IP with the outer radius stretching to 3970 mm. The solenoid will be enclosed by a cryostat vacuum tank filled with liquid helium to control the temperature at 4.5 K.

Outside of the solenoid the iron return yoke constrains the flux and ensures the stray

magnetic field is acceptably small. The return yoke will have an estimated weight of 13400 tons and will also function as the main support structure for the ILD, a tailcatcher, and the muon systems.

The solenoidal field is modified by the presence of an anti Detector Integrated Dipole (DID). The beamstrahlung backgrounds yield low energy charged particles which may be caught in the solenoid field, spiralling through multiple detector components and reducing the precision of the physics measurements; the anti-DID is designed to prevent this. Two dipoles with opposite magnetic field directions are centred on the beam axis and produce a dipole field of 0.35 T which deflects these low energy particles away from the barrel region, reducing the impact of the beamstrahlung particles.

2.2.10 Muon Systems

The detector is completely surrounded by a muon system made up of a barrel region and two endcaps. The muons systems will utilise the return yoke of the magnet interleaved with sensitive layers to identify muons and provide a tailcatcher for highly energetic hadronic particles which are not fully contained within the calorimeters.

To measure accurately the energy of the particles and distinguish between hadronic particles and muons the muon system is separated into two regions. Firstly there are ten layers in which the sensitive layers are 10 cm apart, serving as a calorimeter in both the barrel and endcaps, which are followed by a muon tracker in which the sensors are 60 cm apart. In the barrel region the muon tracker is made up of three sensitive regions whereas there are only two in the endcaps. The most likely technology for the sensitive regions is plastic scintillators with embedded wavelength shifting fibres which feed the collected light to SiPMs. Simulations have suggested that the tail catcher will improve the hadronic resolution of the ILD by $\sim$10% with a 97 % efficiency for identifying muons with energies above 7 GeV.

2.2.11 Performance

The performance of the ILD, as described in the TDR [23], has been established using realistic simulations with updated reconstruction software. Since the Letter Of Intent (LOI) [47], the detector realism has been vastly improved with added dead areas from services, updated geometries, and detector technologies. The tracking software has been completely rewritten to include a new C++ Kalman fitter tool, a rewritten TPC pattern recognition algorithm, and new silicon and forward tracking algorithms. PandoraPFA was completely rewritten to be more flexible and flavour tagging of jets was updated from a multiple step procedure implemented within LCFIVertex into a single package, LCFIPlus. The impact of these changes on the momentum resolution of the tracking systems, the energy resolution of hadronic jets and flavour tagging of jets are shown in Figure 2.8.

The momentum resolution was evaluated for charged particles with energies between 1 GeV and 200 GeV at angles of 7^o, 20^o, 30^o, and 85^o relative to the beamline. As shown in Figure 2.8(a) the momentum resolution at all angles demonstrates the expected performance with the resolution decreases with energy. The momentum resolution improves with angle due to a combination of an increase in the amount of material such as the beampipe before the tracking system and an optimisation of tracking in the barrel region. The momentum goals of ILD have been met for 30^o and 85^o angles (denoted by solid lines) at all energies.

The standard process used to evaluate the performance of PandoraPFA within ILD is to look at the reconstruction of hadronically decaying Z bosons. The events where the Z decays into two up, down, or strange quarks are studied at centre of mass energies of 91, 250, 360, and 500 GeV at all angles within the detector. These events allow the performance of PandoraPFA and the jet energy resolution to be evaluated throughout the entire detector and with increasing jet multiplicities. Back-to-back di-jet events are chosen for this procedure as it minimises the contribution to the performance from confusion within the jet clustering algorithms. The jet energy resolution is defined as $\frac{RMS_{90}}{E_{90}}$ where RMS_{90} is the root mean squared of the central

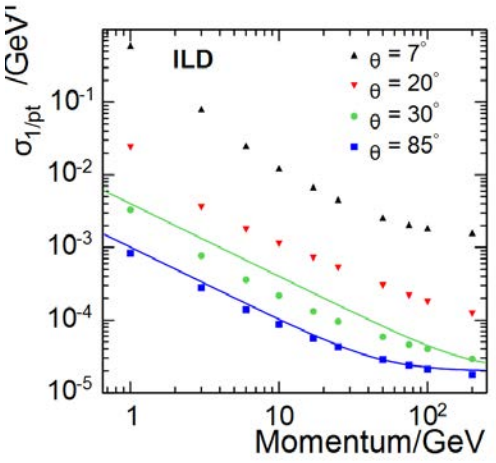

(a) Momentum resolution

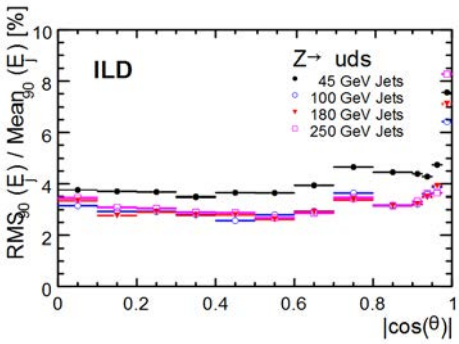

(b) Hadronic jet energy resolution

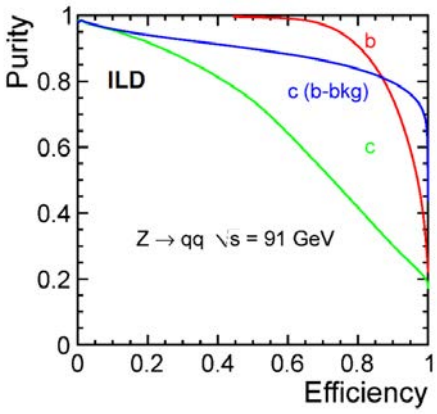

(c) Flavour tagging

Figure 2.8: The performance of ILD with respect to the momentum resolution (top left), PandoraPFA (top right), and flavour tagging of jets (bottom) [23].

90 % of events within the sample and E_{90} is the peak position of this central region. These measures are used to avoid complications which arise from the long tails in the distributions.

A jet energy resolution of <4% is required to separate W and Z boson events which is very important for physics studies at the ILC. Using PandoraPFAs, coupled with the current event reconstruction process within the ILD this has been achieved for all energies studied within the barrel region ($|\cos(\theta)|$ <0.7). There are observed increases in the resolution at 0.7< $|\cos(\theta)|$ <0.8 due to the transition from barrel

to endcaps in the calorimeters and $|\cos(\theta)| > 0.95$ due to a large proportion of the jet escaping down the beamline. Excluding the 45 GeV jets, the desired energy resolution is achieved up to jet angles of $|\cos(\theta)| < 0.95$.

The ROC-curves for the flavour tagging of di-jet events from LCFIPlus are shown in Figure 2.8(c). The flavour tagging is achieved by locating primary and secondary vertices within the events and analysing these with a multivariate analysis [72]. The efficiency and purity of tagging b-jets and c-jets from a mixed background of all quarks is evaluated using $Z \to q\overline{q}$ at $\sqrt{s} = 91.2$ GeV. A very pure sample of b-jets can be obtained with efficiencies of up to 80% which is an excellent result for physics studies with ILD as the accurate tagging of b-jets is essential in many analyses. Also, the separation of b-tags and c-tags is excellent as demonstrated by the ROC-curve for c-tags in a purely b-quark background.

CHAPTER 3

Beam Testing of TPAC

3.1 Introduction

This chapter highlights the results obtained for the TPAC sensor at beam tests at CERN and DESY. Both the motivation for, and setups used at the beam tests are outlined in Section 3.2, the validation of the data both during and after the beam tests is presented in Section 3.3, studies into the electrical properties are explained in Section 3.4.1, the treatment of noise in the sensors in Section 3.4.2, and the results obtained whilst analysing multiple TPAC sensors are summarised in Sections 3.4.3–3.4.5. The primary goal of the DESY beam test was to evaluate the capability of the TPAC sensors to measure the characteristics of electromagnetic showers, including the shower multiplicity and core shower densities, the results of which are given in Section 3.4.6 and Section 3.4.7.

The results from this chapter have been presented at LCWS12 and CALICE 2012,

and preliminary results were shown at TiPP2011 with associated proceedings published here [73].

3.2 Beam Test Overview

3.2.1 CERN August 2009 - pions

Motivation

In August 2009 the Silicon Pixel Detector R&D (SPiDeR) Collaboration tested the TPAC and FOuR Transistor Imaging Sensor (FORTIS) [74] sensors at CERN [75]. The beam test made use of the H6 beam line [76] which delivers pions at up to 120 GeV. The main aims of the test were to investigate the single particle efficiencies of the various TPAC technologies and to characterise the sensor in terms of its monostable lengths (Section 3.4.1) and the noise rates (Section 3.4.2).

Beam overview

The H6 beam line (Figure 3.1) is located in the SPS North Area of CERN and utilises a 450 GeV/c proton beam which has been extracted from the SPS and directed onto a target. The secondary particles from this interaction are then used to provide particles to the P0, H8, and H6 beams. It is possible to choose the energy and particle type of the H6 beam by running in "filter" mode where an additional target (4 mm of Pb) is introduced to form a tertiary beam of 120 GeV/c pions with a momentum spread of 1.5 % [77].

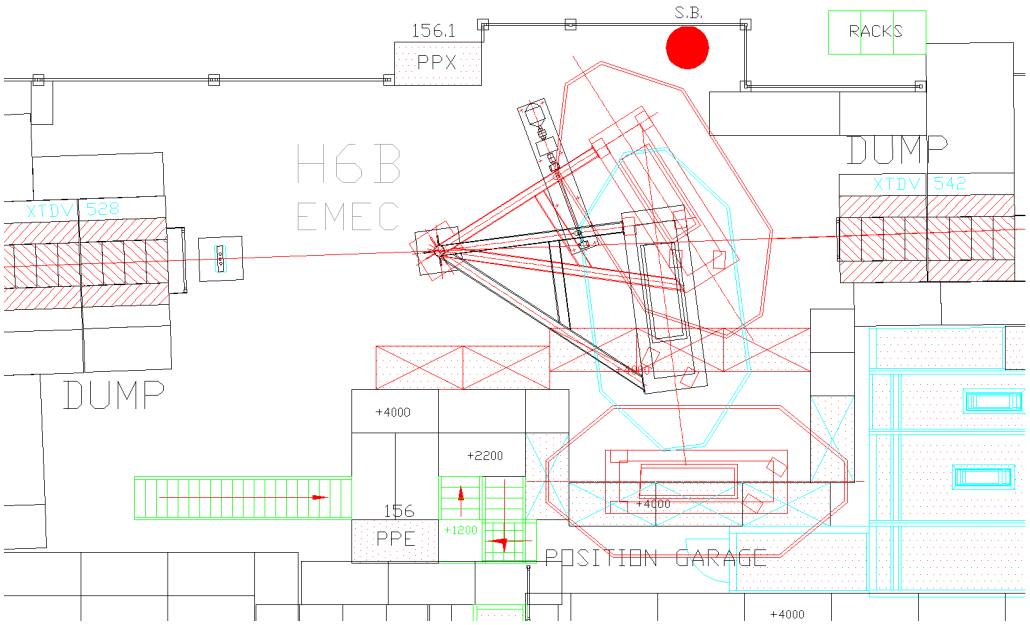

Figure 3.1: A plan view of the H6B test hall at CERN. The beam is incident from the left of the image with the device under test sitting on the moveable table in the centre of the hall.

3.2.2 DESY March 2010 - electrons

Motivation

In March 2010 the TPAC and FORTIS sensors were subjected to further beam testing at DESY [78]. The beam test utilised a beam of 1–5 GeV electrons created from the electron/positron beams of the DESY synchrotron. The main aims of this beam test were to investigate the single pixel efficiencies to electrons, and the response of the sensors to a shower of electromagnetic particles including the multiplicity (Section 3.4.6) and the core density (Section 3.4.7) of the showers.

Beam overview

Four beam lines are available at DESY [79] and these studies utilised the beam controlled from test beam area 21 (see Figure 3.2). The beam was a tertiary beam of electrons originating from the lepton beam of DESY II. The lepton beam was

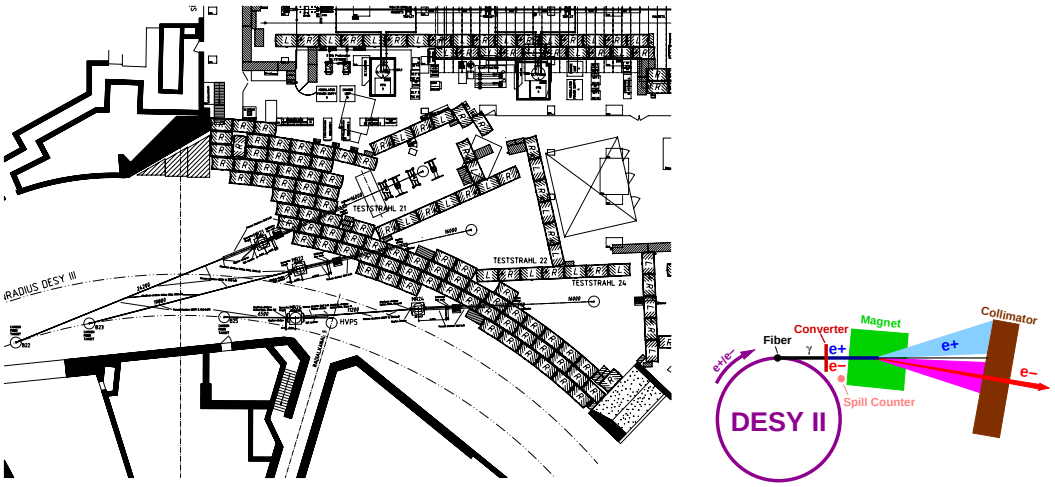

(a) Hall schematic

(b) Beam line cartoon

Figure 3.2: A plan view of the beam lines at DESY. The schematic for the complete experimental hall (3.2(a)) shows the DESY II beamline, the test beam extraction points and the locations of the test beam areas. Test beam area 21 (Teststrahl 21) can be seen towards the middle of the diagram with the control room being the white box with a cross through it to the right of this area. 3.2(b) is a cartoon of beam generation with the carbon fibre target, metal converter plate and magnet to select momenta all shown.

passed through a 25 μm carbon fibre target to create a beam of bremsstrahlung photons. These photons were then converted into electrons and positrons using a metal converter plate. A magnetic field was then used to select the electrons of the appropriate momenta. Using this setup allowed a beam of electrons with a discrete energy of 1-6 GeV with an energy spread of 5 %.

3.2.3 Sensor Setup

During the beam tests the sensors were housed in a TPAC "stack", as shown in Figure 3.3. The stack consisted of 20 evenly spaced slots into which the sensors were inserted. These slots ensured that the sensors were kept firmly in place during operation and the z-position of the sensors were accurately known for tracking purposes. There were four control rods, threaded through the stack and the PCBs on which the sensors were mounted, to ensure all of the sensors were correctly aligned with a relative precision of a few pixels. For consistency between the two beam tests,

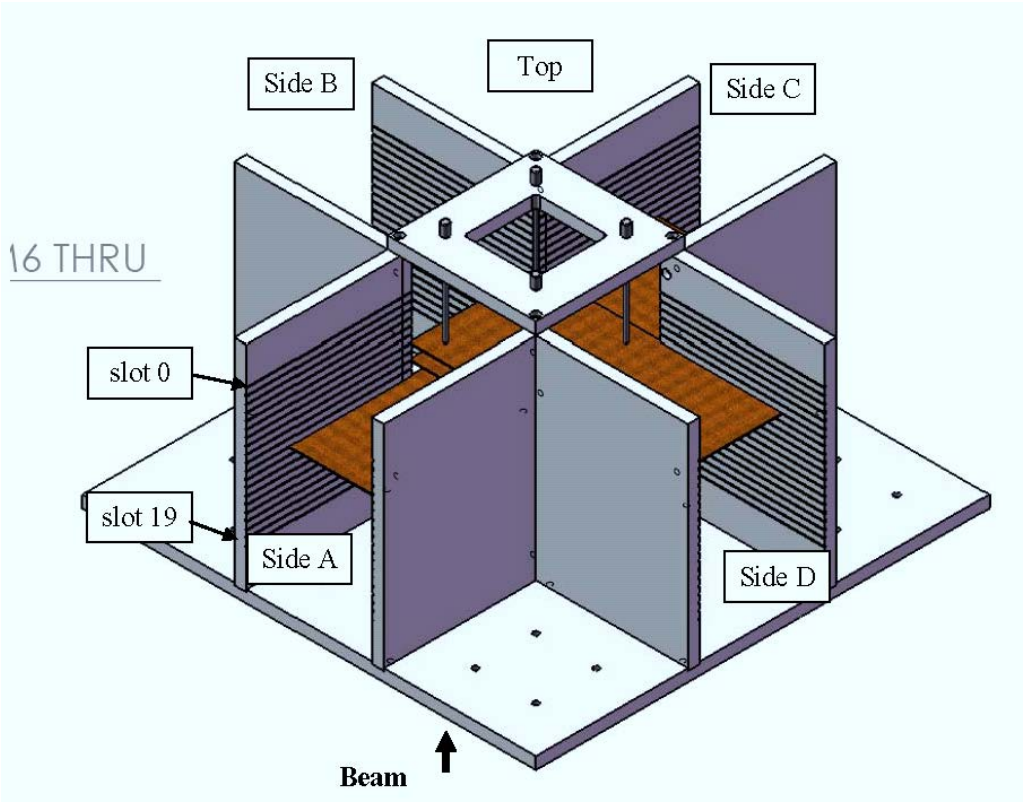

Figure 3.3: A schematic of the test stand where the sensors were housed and PMTs attached to form the TPAC stack. The test stand has four sides accessible to sensors to allow the orientation of the sensors to be easily controlled.

the z coordinate was defined by the centre of slot 14 as this slot housed the sensor closest to the beam at the CERN beam test. The origin of the x and y coordinate system was set to be the centre of the sensor closest to the beam. The stack could comfortably hold 6 sensors at the same time and, with the appropriate orientation, the sensors were located in pairs with a separation in z of approximately 1 mm.

In front of the stack were two overlapping 1 cm^2 plastic scintillators each connected to a PMT. Coupled with an additional scintillator behind the stack, the PMT signals were used for triggering purposes by looking for a coincidence hit between all three scintillators. During the CERN beam test every bunch train was written to disk and the trigger was used offline during the analysis to select interesting events, whereas during the DESY beam test the trigger was developed to write only the interesting events to disk. Details of the PMT hardware configuration are given in

Appendix A.

In general, the sensors in the stack were configured in two operating modes, *Tracking* and *Showering*. In both modes there were six sensors labelled as layer0–5 with layer0 corresponding to the most upstream sensor and layer5 to the sensor furthest downstream of the beam (see Figure 3.5 and Figure 3.7).

Tracking Mode

During tracking mode the six sensors were arranged in three back-to-back pairs (see Figure 3.4 and Figure 3.5). This setup allowed tracks to be formed in the outer two pairs of sensors with the track being projected into the central pair of sensors to allow properties of the sensors to be investigated. The four outer sensors had the standard epitaxial layers operating at a fixed threshold, whereas, the inner sensor types were varied and a range of thresholds were studied.

The stack operated in tracking mode for the entirety of the CERN beam test and approximately half of the DESY beam test.

Showering Mode

During showering mode the six sensors were arranged in a group of four upstream of a block of showering material with the final pair of sensors downstream of this material. In this configuration, tracks were formed in the upstream group of sensors and projected through the showering material into the pair of sensors behind the material.

The showering material was attached to a machined plate (see Figure 3.8) and inserted into slot 5 of the stack. The downstream sensors in the stack were inserted into slots 3 and 2 and kept in the same orientation in such a way as to fix the distance from the downstream surface of the material. This ensured that as extra showering material was added to the stack the solid angle between the downstream

Figure 3.4: Photograph of the TPAC stack setup in tracking mode during the CERN beam test showing six sensors in the TPAC stack with the guide rods visible through the sensors, and the ribbon cables used for readout. The beam is incident from the left of the photograph.

surface of the material and the sensors under test remained constant and removed the need for a correction factor.

During the beam test, three materials were used as the showering material: tungsten, lead, and copper. The amount of material was varied simply by adding extra slabs of each material during data taking. The thickness of the slabs and the corresponding depth in radiation lengths for individual slabs are summarised in Table 3.1. The number of slabs used during running, the total showering material depth, and the corresponding total number of radiation lengths are summarised in Table 3.2. The ratio between the thickness in radiation lengths of the slabs of copper to tungsten was 0.51 and this allowed direct comparisons to be made between the showers induced through the two materials.

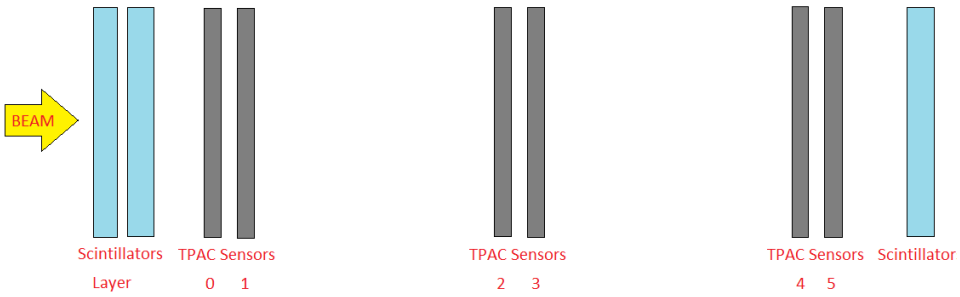

Figure 3.5: A schematic of the TPAC stack setup in tracking mode.

Table 3.1: Summary table of the materials used at the DESY beam test showing the radiation length, slab thickness, and the fraction of radiation lengths of each slab.

Material	χ_0 [mm]	Slab thickness [mm]	$\frac{x}{\chi_0}$
tungsten	3.5	3.0	0.86
lead	0.56	2.0	3.7
copper	14.3	6.3	0.44

3.3 Data Validation

During the CERN (DESY) beam test, a total of 10 (45) million bunchtrains were written to disk over a period of 14 (21) days and it was essential to monitor the quality of the data written to disk. This was of particular importance during the DESY beam test as the data written to disk was selected by the presence of a PMT coincidence. If this trigger was not working as expected it could have biased the data recorded. To test the quality of the data three checks were made:

- the PMTs were checked for coincidences in time,
- the timestamps of the hits within the sensor were compared with the PMT coincidences, and
- the hits within the different sensors were checked for correlations to ensure the timing and alignment of the sensors.

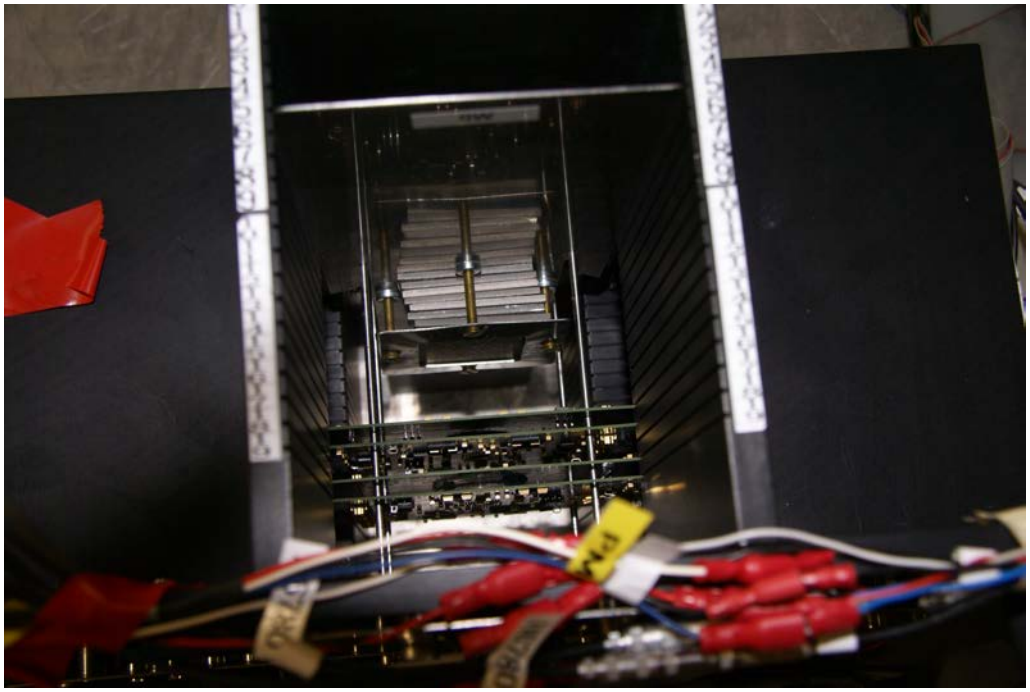

Figure 3.6: Photograph of the TPAC stack setup in showering mode during the DESY beam test showing the four sensors upstream of the showering material and 12 slabs of tungsten as the showering material. The beam was incident from the bottom edge of the photograph.

The PMTs were checked for coincidences in time simply by plotting the timestamps of one PMT against another. This check has been performed for all combinations of PMTs and Figure 3.9 shows strong correlations for all three combinations. This shows that the trigger could be trusted as the PMTs were working efficiently and were well synchronised. It is also important to note the extremely low rate away from the coincidences demonstrating that the PMTs were not just firing randomly all of the time and selecting spurious events. Figure 3.10 demonstrates that the PMT coincidences occurred uniformly throughout a bunchtrain. This is an important feature as it means the results are not biased towards the start of a bunchtrain before sensor effects such as memory filling can occur.

Following the identification of the timestamps with PMT coincidences, the sensors were scanned for interesting events to test both the synchronisation between the sensors and between the sensors and the PMTs. The timestamps of all of the hits in the sensors were plotted relative to the PMT coincidence timestamp, Δ_{ts}, which

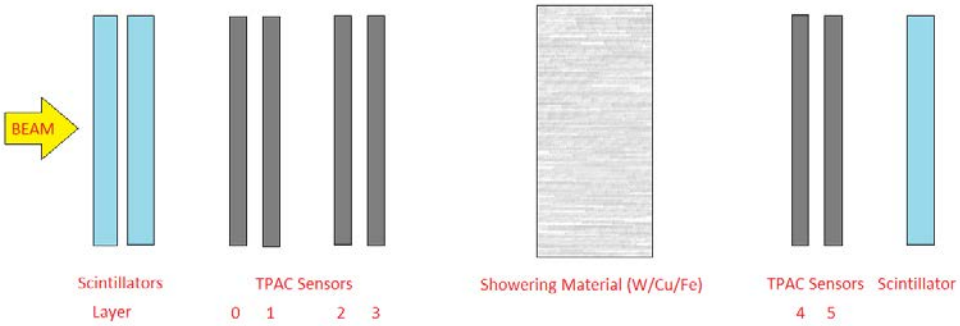

Figure 3.7: A schematic of the TPAC stack setup in showering mode.

Table 3.2: Summary table of the materials and the total depths used at the DESY beam test showing the number of slabs used and the corresponding number of radiation lengths for the three materials

Slabs	$\frac{x}{X_0}$		
	tungsten	lead	copper
1	0.86	3.56	0.44
2	1.71	-	0.88
4	3.43	-	1.76
6	5.14	-	-
8	6.86	-	3.52
10	8.57	-	-
12	10.29	-	-

was quantised in units of 400 ns. As illustrated in Figure 3.11 there is a uniform background in all of the sensors with an excess of hits in a narrow timestamp window of $0 < \Delta_{ts} < 3$. This excess corresponds to genuine hits caused by particles interacting within the sensors and is a powerful tool whilst analysing events. Only hits within this *event window* are considered as signal. As the noise is uniform in time, the noise studies were performed 100 timestamps away from the event window in a *noise window* of three timestamps.

The pixel hits in an event window were checked for correlations in the x-pixel and y-pixel coordinates to ensure that the sensors were aligned. Figure 3.12(a) demonstrates strong correlations between the sensor in layer0 and the sensor in layer3 during showering mode with good alignment. Alignment coefficients were calcu-

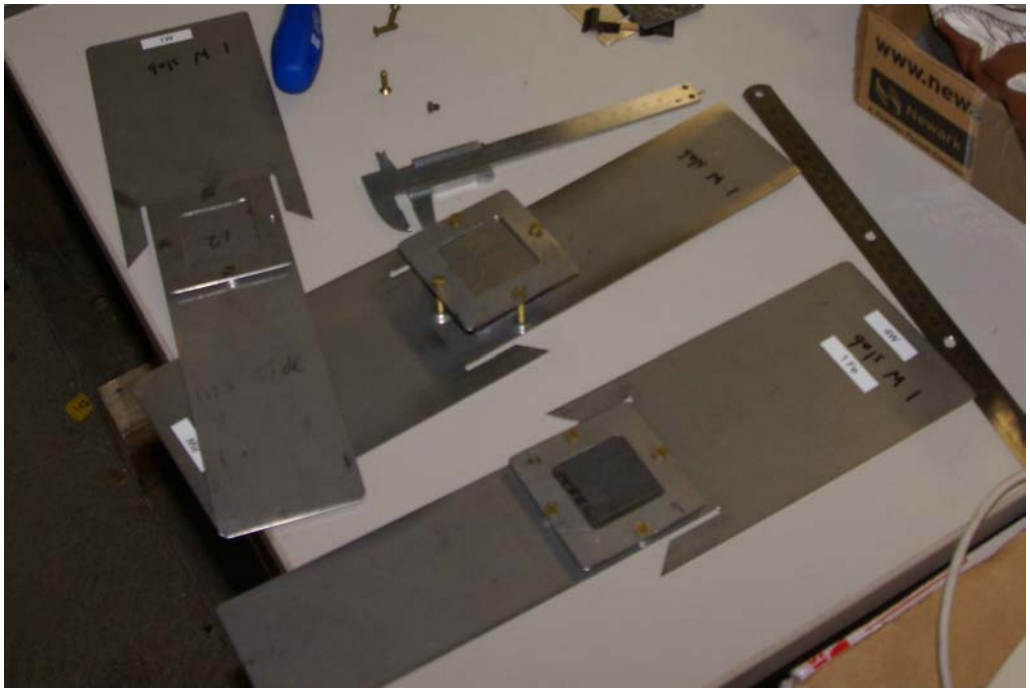

Figure 3.8: Showering material attached to insertion blades to allow easy insertion into the TPAC stack. The grooves in the blades slotted over the guide rods in the stack allowing minimal disturbance to the stack whilst changing the material.

lated by other members of the collaboration to ensure that the slight offsets in the alignment were accounted for in the analyses. When showering material is introduced to the stack the correlations are broader in the sensors downstream of the material due to the incident particles showering (see Figure 3.12(b)).

3.4 Beam Test Results

The results of the various analyses performed using the beam test data collected at CERN and DESY are presented in this section. The CERN data was primarily used to evaluate the monostable length of the pixels and as a comparison of the noise rates in the sensors between the two beam tests. The noise studies and creation of noise masks to compare with the CERN results, and the studies into the properties of the clusters, single particle efficiencies, and the reconstruction of tracks used data with the stack configured in tracking mode at DESY. Finally, with the stack con-

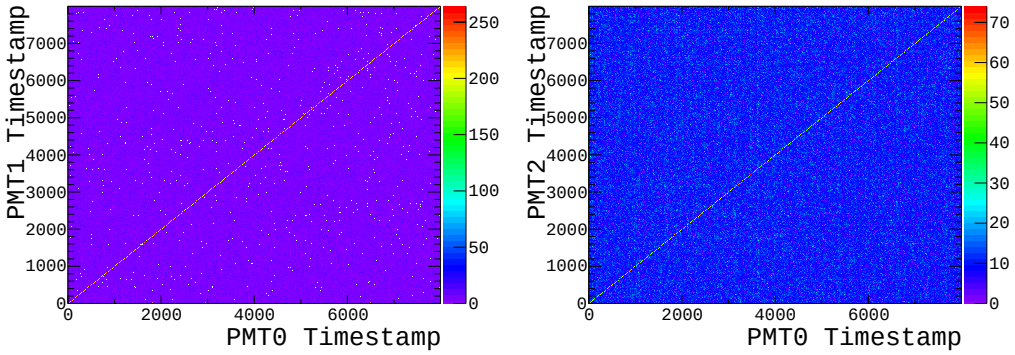

(a) PMT0 versus PMT1

(b) PMT0 versus PMT2

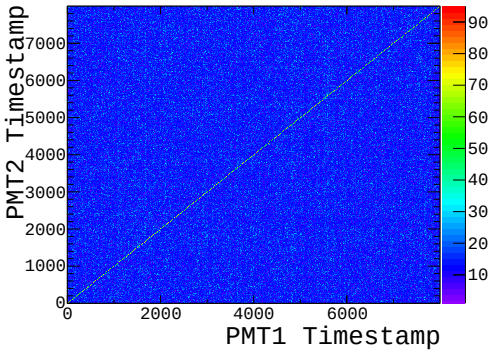

(c) PMT1 versus PMT2

Figure 3.9: PMT timing correlations within a single run for all possible combinations of the PMTs

figured in showering mode at DESY the properties of the showers induced through an absorbing material were studied including the shower multiplicities and particle densities.

3.4.1 Monostable Length

When the total charge in a pixel goes above threshold, a flag is set, which stays active for a fixed timescale set by the monostable length of the pixel. It is essential that this timescale is set correctly to avoid inefficiencies during sensor operation. If the monostable length is shorter than the time between successive readouts (400 ns) then it is possible for a hit to occur at the beginning of a timestamp but not be read out due to the hit flag not being active at the end. However, if the monostable

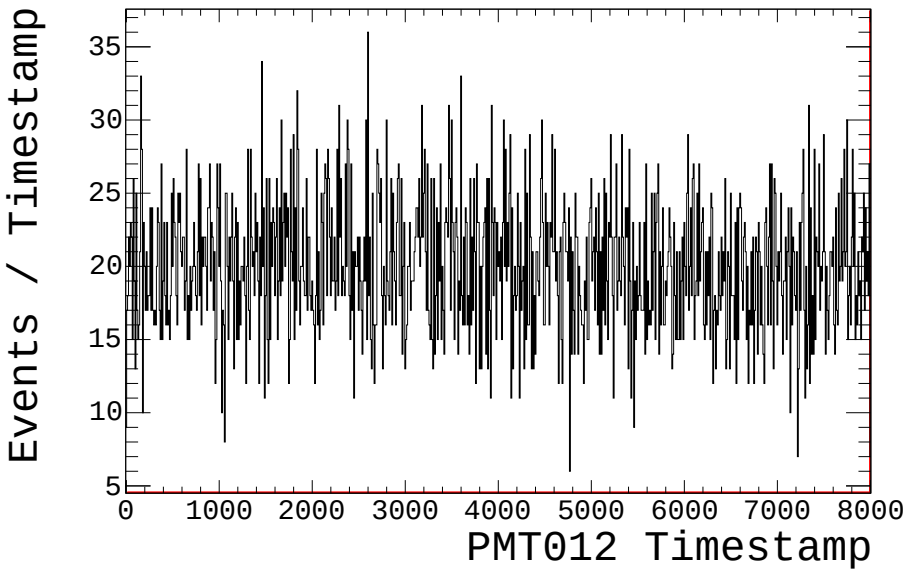

Figure 3.10: The timestamp of a PMT coincidence in all three PMTs

length is too long it is possible that genuine hits could be lost in a timestamp due to the pixel still being active from a previous hit.

Selected runs from the CERN beam test have been analysed where all of the sensors in the TPAC stack were deemed to be "good" and there were more than 10000 PMT coincidences in the run. A "good" sensor is defined to have at least 70 % of the pixels active and a global threshold set to < 999 DAQ Threshold Unit (DTU). All of the hits per pixel in a bunch train were sorted into time order. Chains of successive timestamps for a pixel were then found and any pixel with a chain longer than three was marked as noisy and discarded for the rest of the run. If a pixel had a chain of two successive timestamps then the event was investigated further.

There are four possible ways that a pixel could have a chain of two hits:

- a noise hit followed by a genuine hit (or vice-versa),
- two successive noise hits,
- two successive genuine hits, or

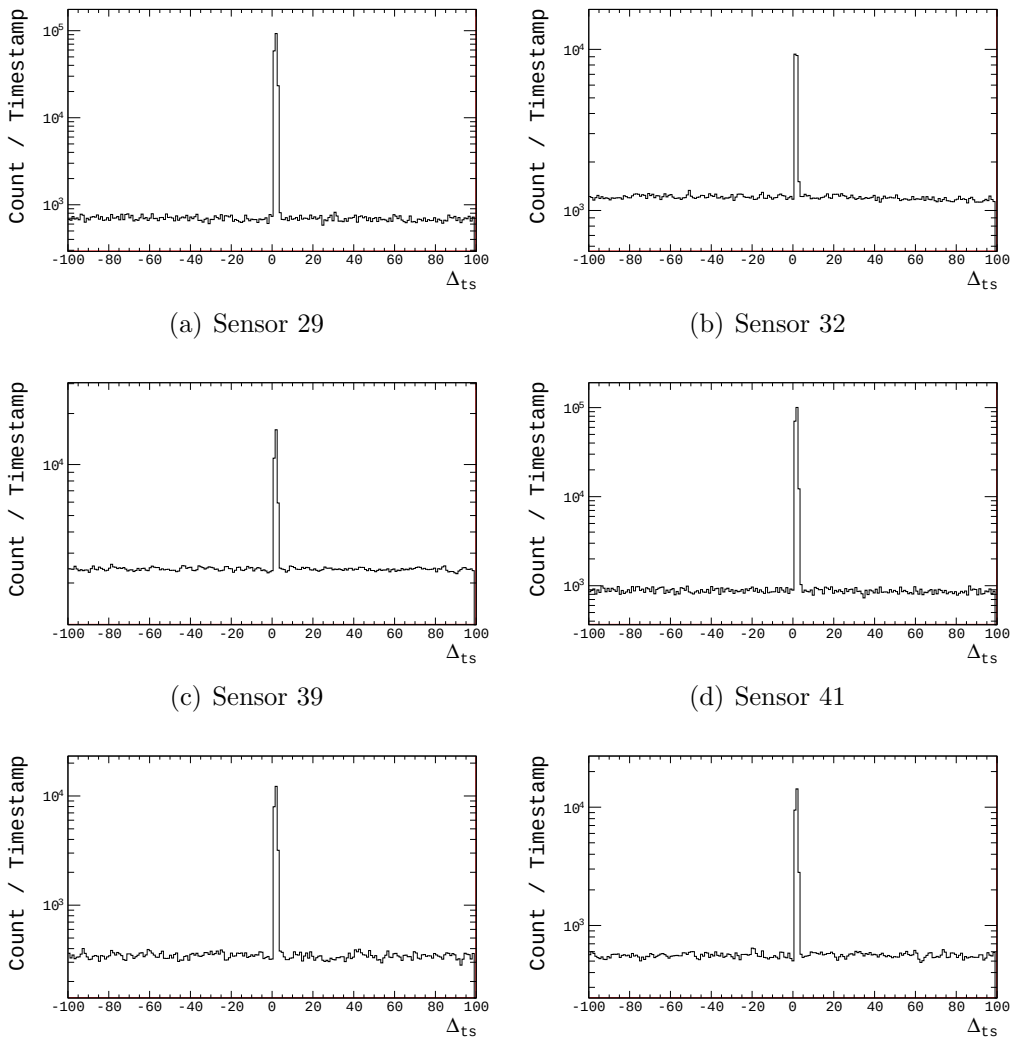

(a) Sensor 29

(b) Sensor 32

(c) Sensor 39

(d) Sensor 41

(e) Sensor 43

(f) Sensor 44

Figure 3.11: Timestamp offset between pixel hits and triple PMT coincidences for all six sensors in the stack for a given run. There are more hits in Sensor 29 and Sensor 41 due to these sensors being down stream of the showering material.

- a genuine hit where the hit flag is still high due to the monostable still being active in the second timestamp ("double-fire").

As the noise rate was extremely low during the CERN beam test (see Section 3.4.2) the probability of the first two options occurring are extremely low and as such the contribution was assumed to be negligible. As the timing of the bunches in the beam test made two successive genuine hits unlikely, and there was no way of distinguishing between two genuine hits and a single hit that double-fired, every

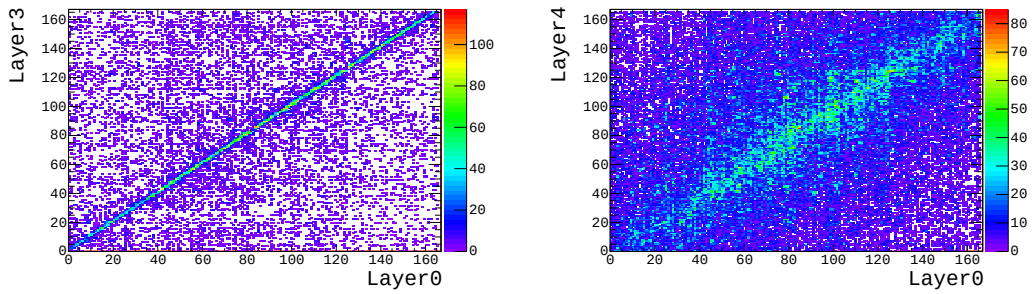

(a) Layer0 versus Layer3

(b) Layer0 versus Layer4

Figure 3.12: Hit correlations between the first sensor in the stack and; the sensor directly upstream of the showering material (Figure 3.12(a)); the sensor directly downstream of the showering material (Figure 3.12(b)).

chain of two hits was assumed to be from a pixel that double-fired.

By looking at the number of times that a pixel fired on average before it double-fired an estimate of the monostable length was obtained. Assuming that the chance of the monostable flag being set is uniform within a bunch crossing, the time between successive readouts is divided into a number of sections equal to the number of times a pixel must fire before it double-fired. Due to the isotropic nature, each of these sections are of equal size and represent a time of 400 / (number of hits to double-fire) ns. As the pixel has already double fired the monostable must be at least 400 ns and the extra segment of time is added to this to give the monostable length. The calculated monostable lengths per sensor are shown in Table 3.3 where the error applies only to the portion of time calculated using the above method and not the complete monostable length.

The monostable lengths of all of the tested sensors are in very good agreement with the target length of 400 ns. This was a very satisfying result as the monostable length is set by hundreds of electrical components and as such is a proof that the sensors were working well. The monostable length in Sensor 39 is slightly larger than in the other sensors and the increased length means there was an increased probability of 10 % over the other sensors of losing hits due to an already firing pixel. However, the probability of this occuring was still small at just 4 %.

Table 3.3: The mean number of hits required for a pixel to double fire and the corresponding calculated monostable length

Sensor	Mean Hits to DF	Monostable (ns)
21	248.3	401.6 ± 0.1
26	1585.8	400.3 ± 0.1
29	177.0	402.3 ± 0.1
32	1599.1	400.3 ± 0.1
39	27.6	414.5 ± 0.6
41	312.3	401.3 ± 0.2
43	263.3	401.5 ± 0.1
48	207.9	401.9 ± 0.1

3.4.2 Noise Rates

As demonstrated in Section 3.3 there is a flat noise dependency away from a PMT coincidence. Only timestamps which were greater than 100 timestamps away from a PMT coincidence were used to study the noise rates in the sensors. This ensured that the mean noise per timestamp was not biased by true hits in the sensor. The noise rates were studied for various sensor types, each running at a range of thresholds between 140 DTU and 250 DTU.

Figure 3.13 shows the mean noise rate in a sensor per timestamp for three sensors during the CERN beam test. Prior to the beam test, pathologically noisy pixels in these sensors were masked to reduce the noise rate and minimise memory filling. The noise rate has an exponential dependence on the thresholds and as such the sensors need to be operated at a high threshold to keep noise to a minimum during data taking. Whilst the noise rate is vastly reduced at these higher thresholds, the efficiency of recording a genuine hit is also reduced (see Section 3.4.4). A more detailed study into the dependency of the efficiency versus threshold can be found here [35].

The noise rate is largely independent of the choice of epitaxial layer. For the development of a DECAL this is extremely important as it means that none of the three TPAC technologies which utilise the INMAPS process would give a significantly higher number of noise hits in a DECAL.

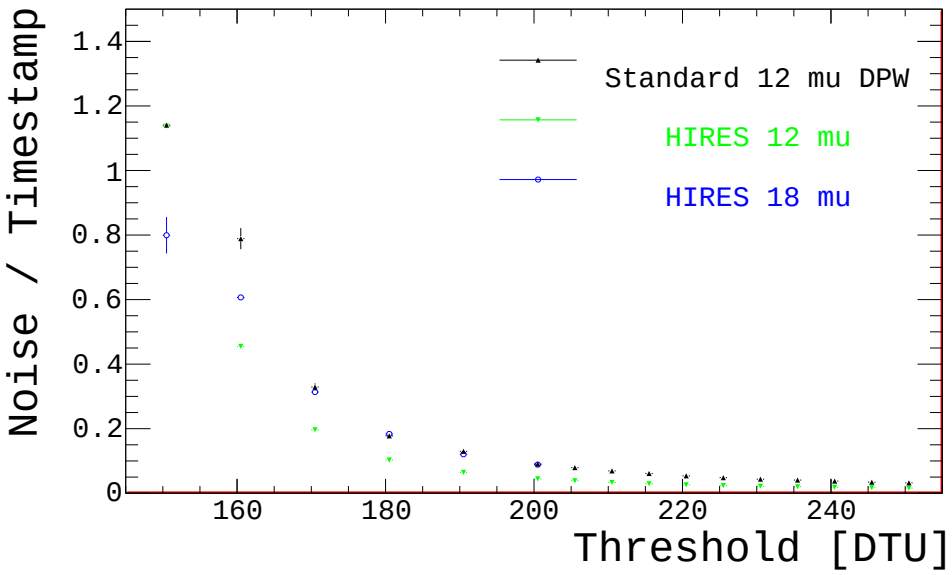

Figure 3.13: Noise rate versus threshold in DTU for sensors with noisy pixels masks active during data taking. The standard 12 μm sensor is shown in black, the 12 μm high resistivity sensor is shown in green, and an 18 μm high resistivity sensor shown in blue.

Due to time constraints prior to the DESY beam test, and the masking process for a single sensor being very time consuming, the sensors operated without the pixel masks at DESY. Figure 3.14 shows an increase in the noise rate caused by not having the pathologically noisy pixels masked for the four sensors which operated at the full range of thresholds at both the CERN and DESY beam tests. The noise rate is much higher across the whole range of thresholds without the pixel masks.

A high noise rate was far from ideal for the studies conducted using the DESY beam test data. For the shower multiplicity studies a high noise rate, given a low shower multiplicity due to the low energies of the incident particles, could add a huge bias to the results. Likewise, if there are too many noise hits, the shower density calculations could be affected through increasing the search area, increasing the number of hits in the core of the shower, or a combination of both. To avoid these problems the DESY data was processed before analysis to create post run noise masks which excluded pixels from the analyses.

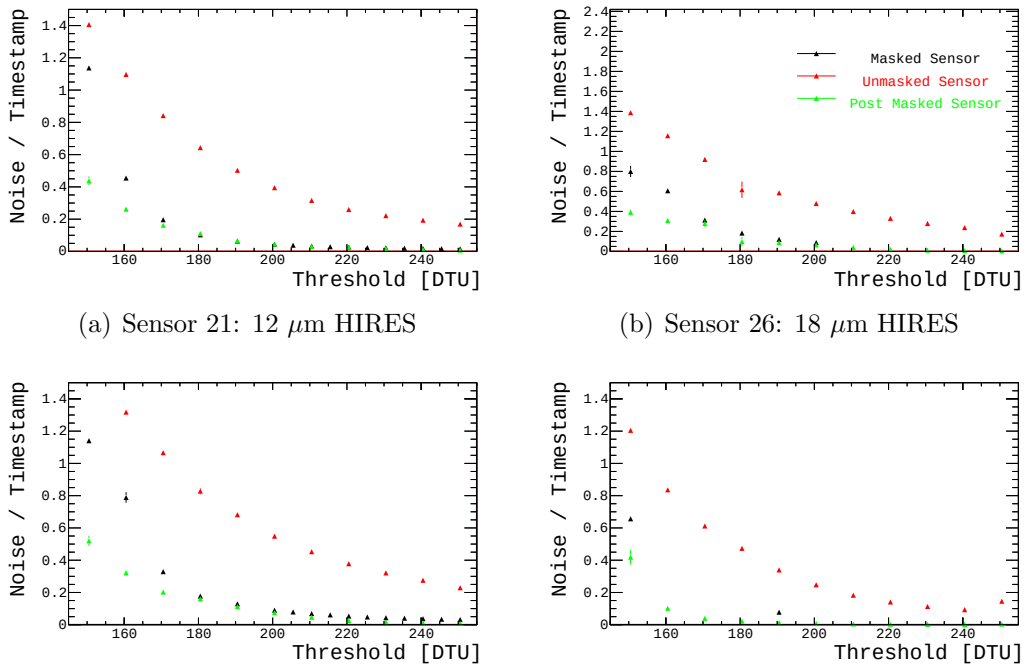

(a) Sensor 21: 12 μm HIRES

(b) Sensor 26: 18 μm HIRES

(c) Sensor 39: 12 μm DPW

(d) Sensor 43: 12 μm DPW

Figure 3.14: Noise rate versus threshold for masked and unmasked sensors. The masked sensors used at the CERN beam test are shown in black, the unmasked sensors used at the DESY beam test are shown in red, and the unmasked sensors used at the DESY beam test with the post run noise masks are shown in green.

Noise Masks

Three criteria of selecting the noisy pixels were implemented for each sensor to ensure that the post run noise masks were robust, efficient, and pure. These were:

- a pixel fires in three consecutive timestamps,
- the total number of noise hits in a pixel is greater than ten times the average for the sensor in question, or
- a pixel is in the top 1000 (of 28224) of the noisiest pixels in each sensor.

For a pixel to be masked at least two of the three criteria needed to be satisfied. This would, for example, prevent a pixel being masked after a genuine hit which

double fired followed by a noise hit which, although extremely unlikely, had a finite probability of occuring.

To evaluate the efficiency of noise removal, the noise was studied in a window offset from the PMT trigger by 100 timestamps for an unmasked sensor, with and without the post run noise masks applied. The efficiency of the noise removal is given by

$$\epsilon_{noise}^{removal} = 1 - \frac{N_{unmasked}}{N_{all}} \ , \tag{3.1}$$

where N_{all} is the total number of hits in the noise window for all pixels and $N_{unmasked}$ is the total number of hits in the noise window for the pixels which were unmasked after applying the post run masks.

Sensor 39 demonstrated a lower noise removal efficiency compared to the other sensors studied (see Figure 3.15). However, this is due to the noise in this sensor being spread more uniformly across all pixels rather than being dominated by the pathologically noisy pixels. At the higher threshold the efficiency of the noise removal is comparable to the other sensors as the higher threshold has reduced the noise rate in the unmasked pixels.

The purity of the noise removal was evaluated using the Δ_{ts} of all hits relative to the PMT coincidence timestamps (for examples see Figure 3.11). The mean noise was evaluated by fitting the noise outside of the event window with a simple polynomial. The mean noise was then removed from the total hits within the event window. This calculation was performed for all pixels without the masks applied, and all pixels which were unmasked after the mask had been applied, with the purity given by

$$\rho_{noise}^{removal} = \frac{S_{unmasked}}{S_{all}} \ , \tag{3.2}$$

where $S_{unmasked}$ is the number of signal hits for all unmasked pixels and S_{all} is the number of signal hits for all pixels. When evaluated for multiple sensors during

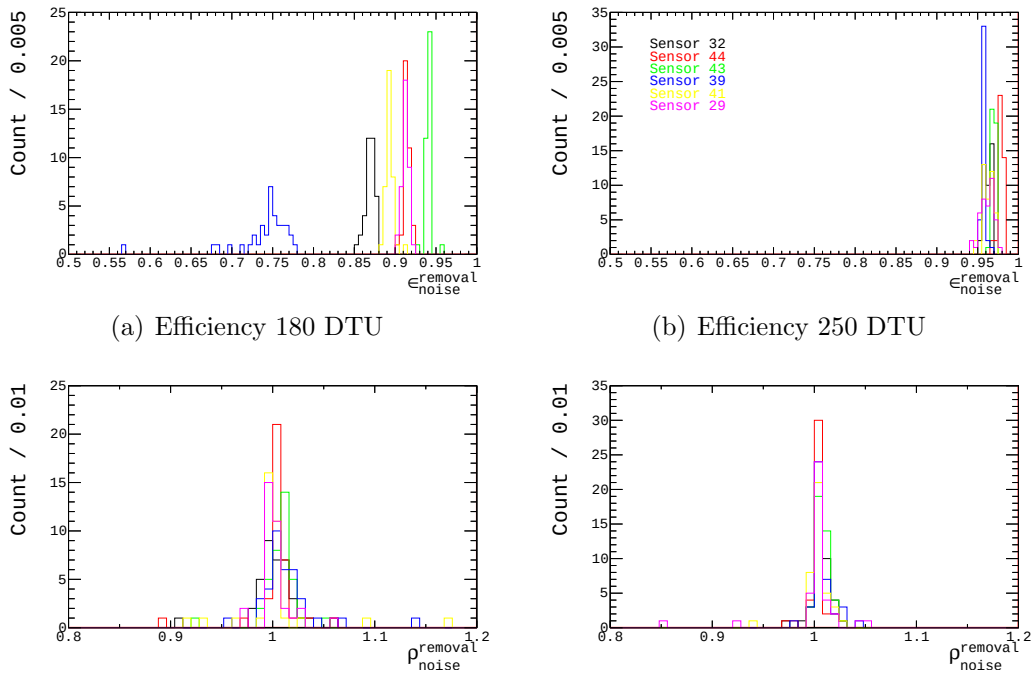

(a) Efficiency 180 DTU

(b) Efficiency 250 DTU

(c) Purity 180 DTU

(d) Purity 250 DTU

Figure 3.15: Efficiency and purity of noise removal when applying the post run noise masks for the six standard 12 μm DPW sensors used whilst the stack operated in tracking mode during the DESY beam test calculated using Equations 3.1–3.2.

multiple runs, the mean purity of removing just noise hits was greater than 98 % for all sensors.

Figure 3.14 demonstrates that when the post run noise masks were applied to the data collected at DESY the noise rate was comparable to that of the same sensors operating with the noise masks active during data taking at CERN. The noise rate is actually lower in the post run masked sensors below 170 DTU. This is a sign that the masks are removing good pixels due to their increased noise rate at the lower thresholds. However, this is not a problem in the analysis as the post run noise masks were primarily used in the shower multiplicity and shower density studies, where the sensors only operated at 180 DTU and 250 DTU.

Table 3.4: The efficiency and purity of noise removal via the post run noise masks for all six sensors studies whilst the TPAC stack operated in showering mode.

Sensor	180 DTU		250 DTU	
	$\epsilon_{noise}^{removal}$	$\rho_{noise}^{removal}$	$\epsilon_{noise}^{removal}$	$\rho_{noise}^{removal}$
21	0.91	1.00	0.96	1.01
32	0.87	1.00	0.96	1.00
39	0.74	1.01	0.96	1.01
41	0.89	1.01	0.96	1.01
43	0.94	1.00	0.97	0.99
44	0.91	0.99	0.98	0.98

3.4.3 Tracking

For the remaining studies in this chapter forming tracks in the data was an essential stage of the analysis. Sections 3.4.4–3.4.5 relied on tracks formed in the outer two pairs of sensors with the tracks projected into the central sensors. Sections 3.4.6–3.4.7 utilised tracks formed in the first four layers which were then projected through the showering material into the final two sensors.

In all of these analyses, tracks were formed using at least three of the four tracking sensors with the z-positions set by the sensor orientation and the slot in which the sensor was housed. The hits within a sensor were forced into clusters using the method described in Section 3.4.5. The global x-positions and y-positions were then calculated using the centre of gravity of the cluster, sensor orientation, and alignment coefficients. Within a discrete continuous distribution of uniform width the error on the position is given by $1/\sqrt{12}$ [80]. Therefore, the error on the points used for the tracks was simply their width$/\sqrt{12}$. A track is defined as a straight line trajectory fitted through the clusters with the track probability calculated using the residuals of the centre of gravity of the clusters relative to the straight line.

Optimal tracks were found by iterating over all of the clusters within the tracking sensors and selecting all tracks with a track probability of greater than 0.1. The tracks were then filtered for the best tracks with no repeated clusters to ensure double counting of hits did not occur. The probability distribution of all tracks in

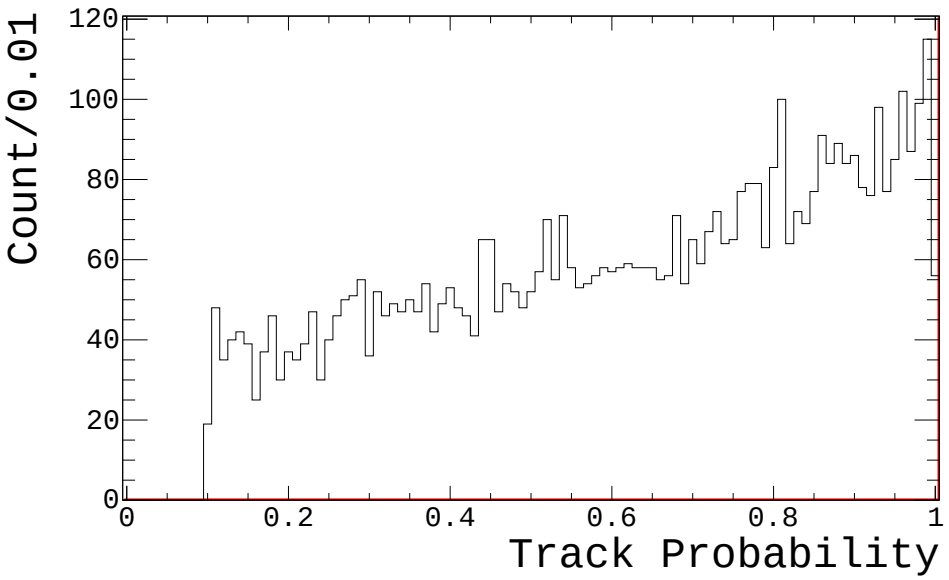

Figure 3.16: The track probability for all tracks with probability greater than 0.1 for an example run taken during showering mode.

a run is shown in Figure 3.16. Ideally the distribution should be flat, the excess of tracks at high probability being an indication that the errors on the track hits are slightly overestimated. A full study into the hit positions versus cluster shapes would have improved the position resolution, this however, was not possible due to limited statistics in data and imperfect modelling by simulations (Section 3.5).

3.4.4 Single Pixel Efficiencies

A complete study into the single particle efficiencies for the different TPAC sensors has demonstrated the importance of the INMAPS process to the operation of sensors utilising full CMOS components [35]. In this section a simplified method of calculating the single particle efficiency of the sensors is presented to allow a comparison between data and simulation.

Tracks were formed in the outer four sensors and projected into the middle sensors. The pixels in a 7×7 grid around the track projection were then examined for dead areas such as memory full pixels, masked pixels, or edge pixels. If the search area

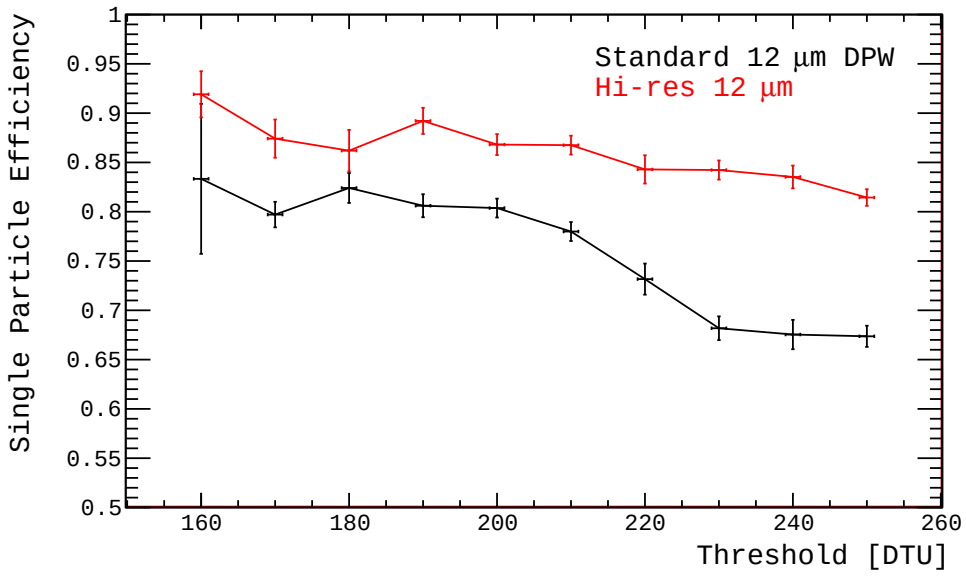

Figure 3.17: Single particle efficiencies for a standard sensor (black points) and a high resistivity 12 μm sensor (red points) calculated using the counting method.

was clear the event was deemed to be usable and a counter, N, was incremented. When genuine hits were identified within a 2σ search area of the track projection a second counter, n_{hits}, was incremented. The efficiency, ϵ_{sp}, was given by

$$\epsilon_{sp} = \frac{n_{hits}}{N} \quad . \tag{3.3}$$

The study used a subset of runs from the DESY beam test operating in tracking mode where the central two sensors (a standard INMAPS sensor and a 12 μm high-resistivity sensor) operated at a variety of thresholds from 150 DTU to 250 DTU.

The efficiencies calculated using the simplified method are summarised in Figure 3.17 and are comparable to the results in [35]. The high-resistivity sensor demonstrates an improved efficiency due to a decreased charge collection time leading to less charge being collected parasitically or escaping the sensor. This effect is even more apparent at the higher thresholds.

3.4.5 Cluster Sizes

The lack of a physical barrier between the pixels in the TPAC sensor allows charge to diffuse into neighbouring pixels. This leads to the potential of multiple pixels firing for a single particle. This, coupled with the possibility of pixels firing in consecutive timestamps, can lead to an overestimation of the number of particles in the sensor. The extra pixel hits in the event and noise windows were removed by forming three dimensional clusters (x-position, y-position, and timestamp). The time dependence was clustered by initially searching for pixels in the window which double fired and removing the second hit. Due to the narrow event window the timestamps of all the remaining hits in the window were assumed to be equal. The spatial clustering utilised a simple nearest neighbour algorithm where the eight pixels around a seed pixel were checked and any firing pixels were clustered together and removed from the hit list. The clustering continued until no further clusters were formed. There are four possible outcomes of this clustering algorithm:

- a cluster of size one in a single timestamp (single pixel),
- a cluster of size one in two consecutive timestamps (double fire),
- a cluster of size greater than one in a single timestamp, and
- a cluster of size greater than one in multiple timestamps.

The mean cluster sizes obtained are shown in Figure 3.18 as a function of threshold for two sensors, one standard 12 μm sensor and one high resistivity sensor. An increase in the mean cluster size for the high resistivity sensor over the standard sensor was observed due to the increased charge diffusion speed and charge collection efficiency. The cluster sizes are found to increase with the threshold of the sensor. This is unexpected as the higher thresholds are expected to lead to smaller cluster sizes because fewer pixels will contain sufficient charge to fire. This exposed a limitation in the clustering method: noise hits are treated as clusters of size one. As the noise rate drops as a function of threshold, the fraction of clusters of size

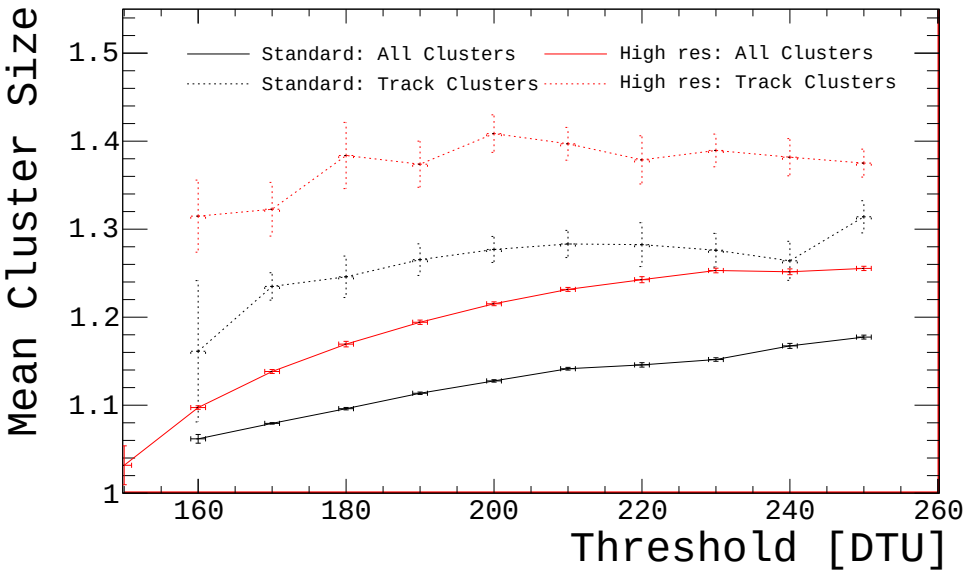

Figure 3.18: The mean cluster sizes versus threshold for a standard sensor (black points) and a high resistivity 12 μm sensor (red points), for all clusters (solid lines) and only clusters associated with tracks (dashed lines).

one caused by noise decreases leading to a higher mean cluster size. As the mean multiplicity in the sensors during tracking mode is of order one, the effect of the noise is substantial to this study.

To remove the side-effect of the noise clusters, all clusters not associated with a track were removed, as shown in Figure 3.18 (dotted lines). With the noise clusters removed the mean cluster sizes for the sensors increased across the whole range of thresholds. The mean cluster sizes still increased at the low thresholds where the noise rate is higher but plateaus around 180 DTU.

3.4.6 Shower Multiplicities

The shower multiplicities for various radiation lengths of tungsten and copper were studied with the stack setup in showering mode and all six sensors operating at the same threshold (180 DTU or 250 DTU dependent on the run configuration). Clusters were formed using the nearest neighbour algorithm described in Section 3.4.5 and tracks were formed in the four sensors upstream of the showering material using the

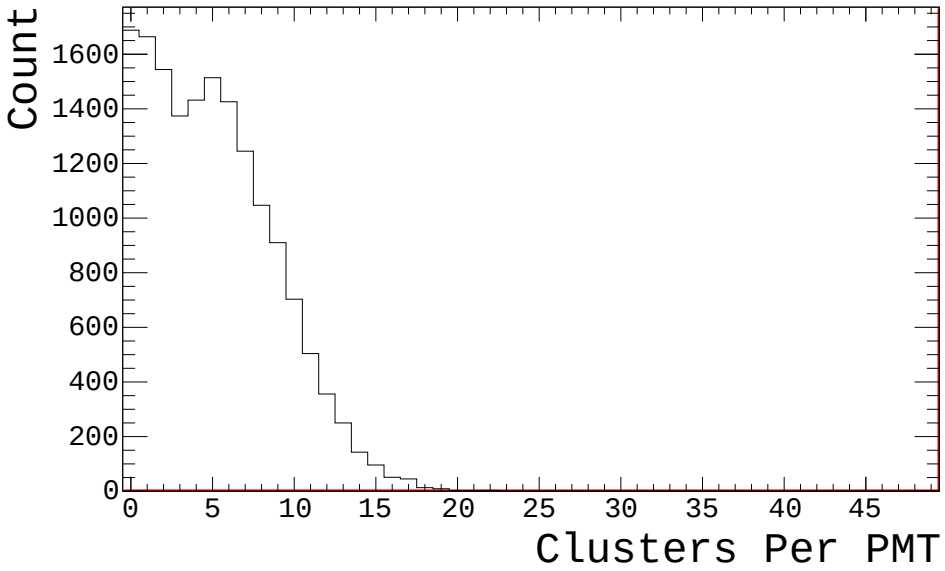

Figure 3.19: Number of clusters in a sensor placed downstream of 3.86 χ_0 tungsten for all PMT coincidences operating at 180 DTU.

method from Section 3.4.3. The shower multiplicity was then given by the ratio of the number of clusters found in the event window of a sensor to the number of tracks formed in the same window.

Figure 3.19 shows the typical distribution of the number of clusters found in the sensor directly downstream of the showering material for all events where there was a PMT coincidence in a typical run at DESY. The peak in the distribution around zero was initially associated with events in which no track was formed, leading to only noise hits in the sensors. However, due to the low noise rate the proportion of events at low multiplicity is much too high. The low multiplicity events are therefore associated with events in which tracks were formed but a large proportion of the shower missed the sensor. These events were rejected by projecting the tracks into the downstream sensors and only keeping the events where the number of tracks through the central region of the sensors was equal to the total number of tracks. When this cut was applied the low multiplicity peak is removed (see Figure 3.20), leaving a simple Gaussian distribution. This distribution was fitted to extract the mean shower multiplicity for each configuration of material and material depth.

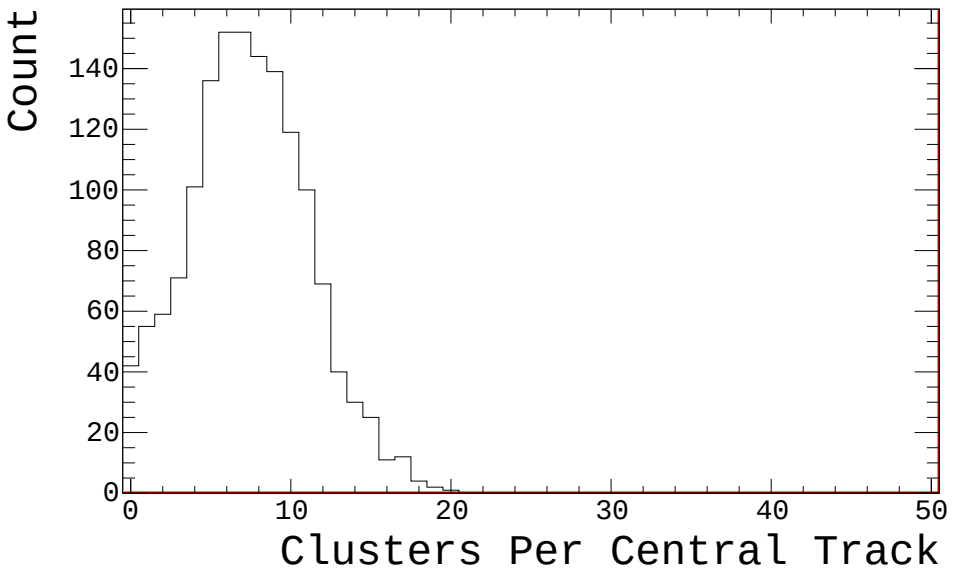

Figure 3.20: Number of clusters in a sensor placed downstream of 3.86 χ_0 tungsten for events where the projection of all tracks in the event were required to pass through the central region of the sensor operating at 180 DTU.

The shower multiplicities were extracted from the fits and studied as a function of material depth, t, for 1–4 GeV electrons with the sensors operating at two thresholds, 180 DTU and 250 DTU. Figure 3.21 shows the multiplicity distributions alongside the fit results of all material depths of tungsten for 4 GeV electrons and a sensor operating at 180 DTU. It can be seen that the number of clusters measured in the sensors downstream of the showering material increases with the amount of material up to a peak of approximately 4 χ_0, above which the number of clusters decreases again. This is summarised in Figure 3.22.

Figure 3.22 demonstrates a fundamental requirement of the DECAL concept: *the multiplicity in the sensors increased across the whole range of t as the incident electron energy increased.* The same behaviour was observed when the sensors operated at the higher threshold of 250 DTU (see Figure 3.23). Figure 3.24 demonstrates a reduced multiplicity in the downstream sensors at the higher threshold. This was expected due to the reduced single particle efficiency at the higher threshold.

The shower multiplicity plots in Figures 3.22–3.24 were fitted with Equation 1.12

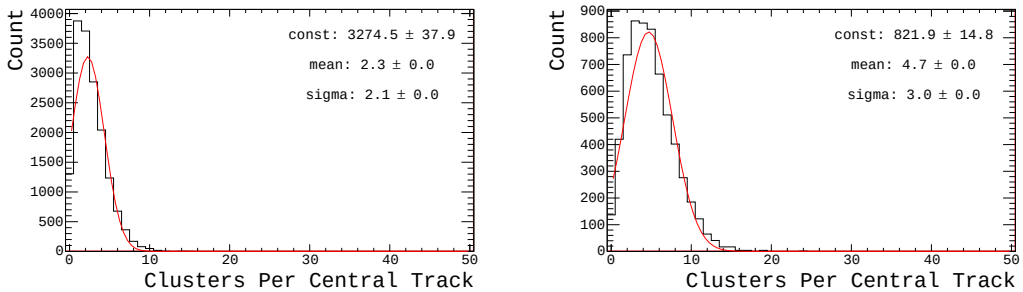

(a) 0.86 χ_0

(b) 1.71 χ_0

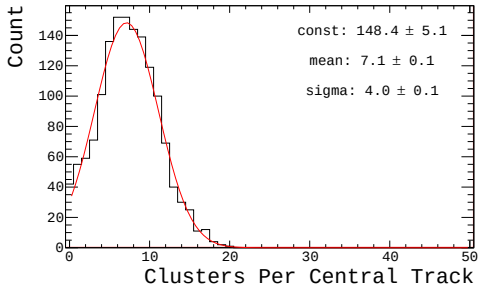

(c) 3.43 χ_0

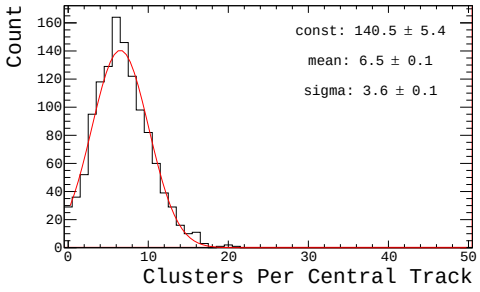

(d) 5.14 χ_0

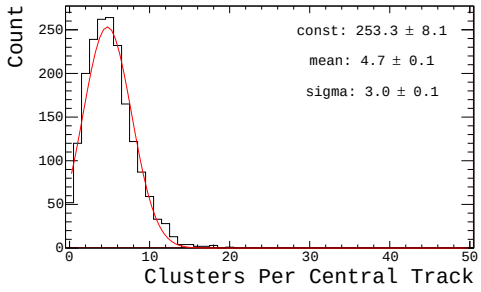

(e) 6.86 χ_0

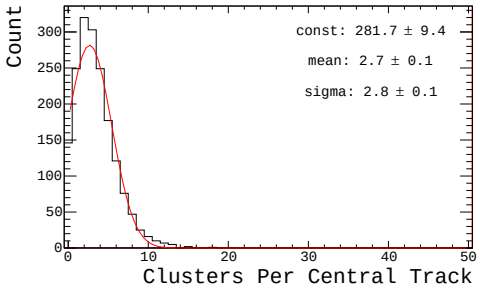

(f) 8.57 χ_0

Figure 3.21: Fitted number of clusters in a sensor placed downstream of the tungsten material for various depths of material for all tracks projected into the central region of the sensor operating at 180 DTU and 4 GeV electrons.

to allow a calculation of t_{max} from Equation 1.14 to be made. Ordinarily, the b parameter in Equation 1.12 should be approximately 0.5 [8]. However, as a single sensor does not achieve complete lateral containment of the shower, it was reasonable to allow this parameter to float to achieve the best fits. At 250 DTU the fits for 1 GeV failed for values of t above four as a result of the small incident energy. Figure 3.25 shows the values of t_{max} have the required logarithmic behaviour with the incident energy for both of the thresholds. This implies that the assumptions made during the fit are valid.

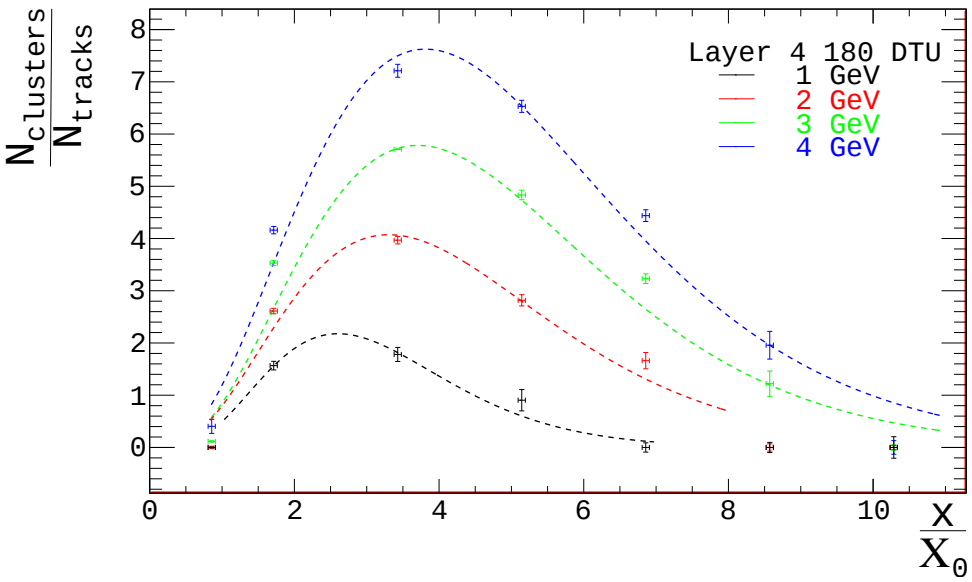

Figure 3.22: Shower multiplicities fitted with Equation 1.12 for the sensors operating at a threshold of 180 DTU with all energies overlaid.

The only exception to the setup in showering mode was when 3.52 χ_0 of copper was inserted into the stack. Due to the physical depth of the material and mechanical constraints of the stack, the material was inserted into slot 4 leading to a reduced solid angle to the sensor in layer4. For this configuration the sensor in layer5 was approximately the same distance from the material as the sensor in layer4 had been previously and, as such, the sensor in layer5 was used to calculate the multiplicity. The shower multiplicities calculated for the copper runs are displayed in Figure 3.26 and demonstrate the same trend as the tungsten data with an increase in multiplicity up to approximately 4 χ_0. Data for material depths thicker than this was not taken due to the lack of physical space in the stack so an assumption is made that the shower multiplicity decreases above this value as per the tungsten data.

Figure 3.26 shows that the particle showers induced through copper have a lower observed multiplicity than those in tungsten. In theory, on a statistical basis, the particle showers should be identical as they have been created using the same number of radiation lengths. However, the radiation length of a material, calculated using Equation 1.11 is just an approximation as the cross sections of the interactions with matter vary from material to material. The cross section of the photoelectric effect,

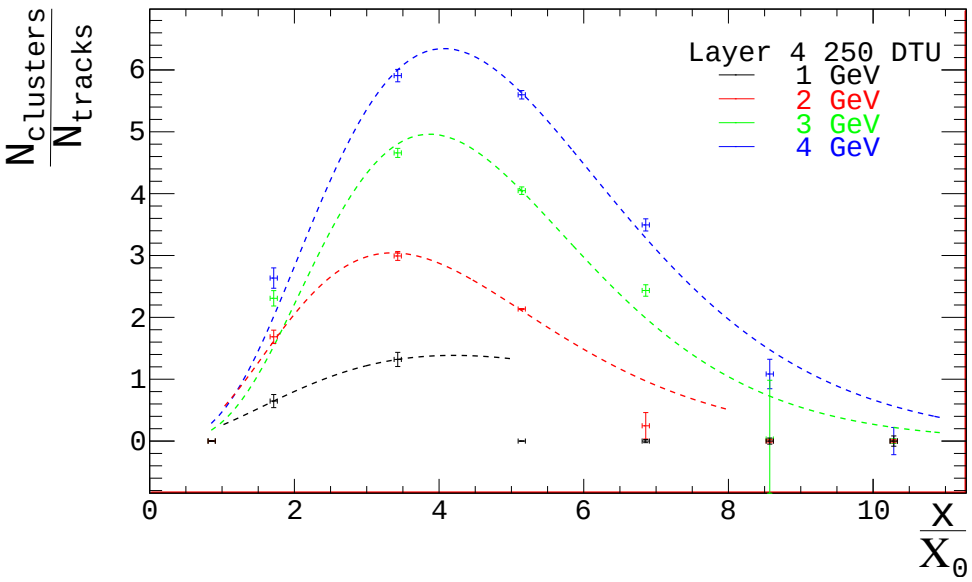

Figure 3.23: Shower multiplicities fitted with Equation 1.12 for the sensors operating at a threshold of 250 DTU with all energies overlaid.

$$\sigma_{PE} \propto Z^4 \ , \tag{3.4}$$

Bremsstralung,

$$\sigma_{Brem} \propto Z^2 \ , \tag{3.5}$$

and pair production,

$$\sigma_{pair} \propto Z^2 \ , \tag{3.6}$$

are dependent on the atomic number, Z, of the material. Tungsten has a much larger atomic number (Z=74) compared to copper (Z=29) leading to different cross sections and as such different shower profiles. A similar effect has been observed in the CALICE HCAL protoypes where differences in the showers have been observed when the absorber material has been changed from iron to tungsten [81].

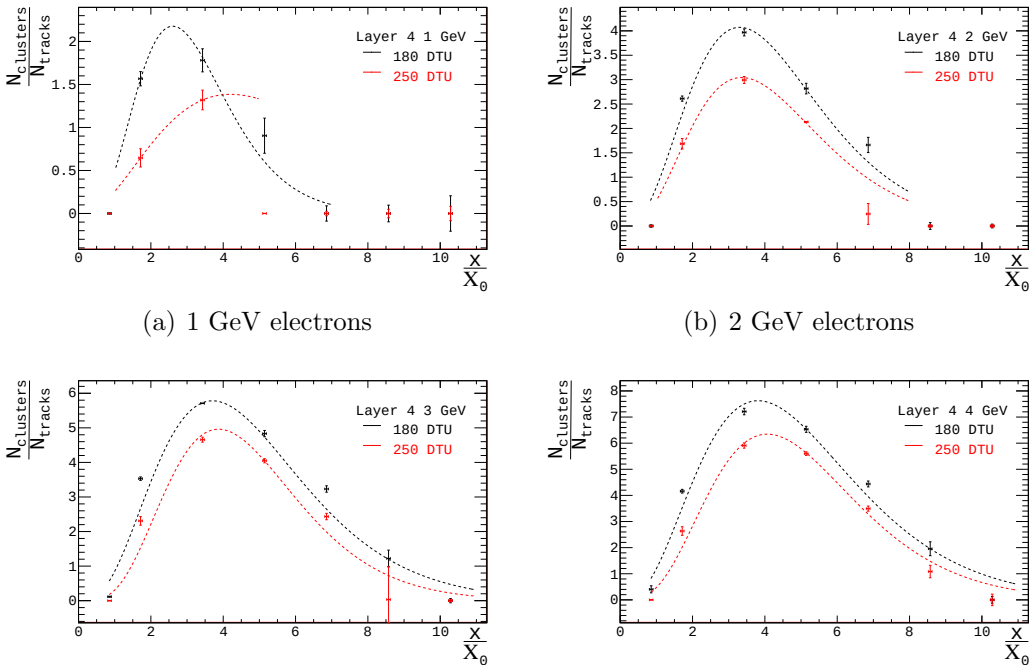

(a) 1 GeV electrons

(b) 2 GeV electrons

(c) 3 GeV electrons

(d) 4 GeV electrons

Figure 3.24: Shower multiplicity for each energy with the 250 DTU (red points) and 180 DTU (black points) threshold results overlaid demonstrating the reduced multiplicity at the higher threshold.

3.4.7 Shower Densities

The ultimate goal of the DESY beam test was to measure the core shower density of low energy electromagnetic showers with high granularity. This was an essential study as the very low thresholds in the sensors, coupled with the modelling of low energy electromagnetic showers, could have lead to saturation in the sensors due to a large number of unexpected low energy particles in the shower.

Tracks were formed using clusters in the four sensors upstream of the tungsten (in this study only the tungsten data was used) and projected through the material into the central region as per the multiplicity studies. To remove the possibility of overlapping showers, only events with a single track formed in the upstream sensors were analysed. The projection of the solitary track into the downstream sensors was defined to be the centre of the shower and the core densities within a circular search area were calculated relative to this point. The radius of the search area, r, was

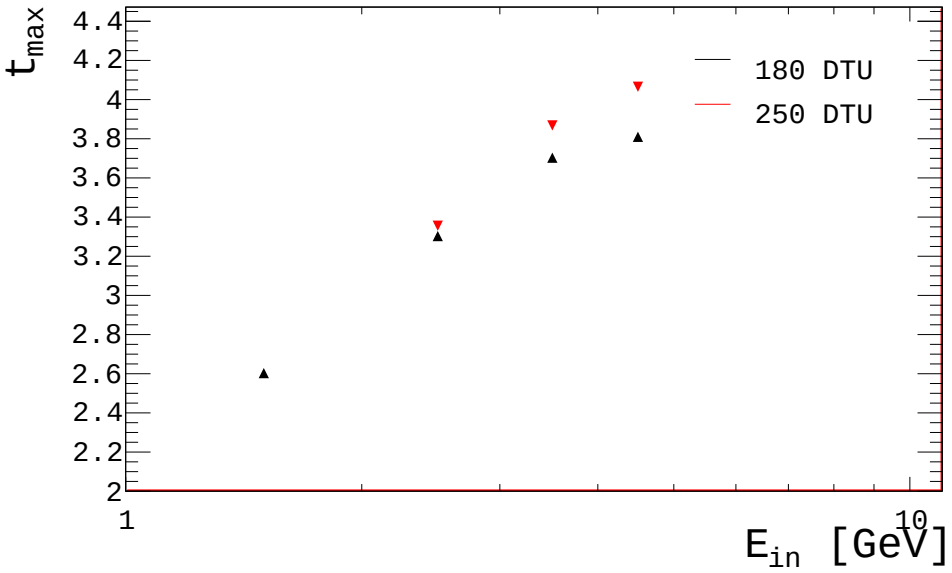

Figure 3.25: The values of t_{max} calculated using Equation 1.14 with the parameters extracted from the fits of Equation 1.12 in Figure 3.24 for the two thresholds; 180 DTU (black points), and 250 DTU (red points).

incremented in steps of 100 μm, the number of clusters, $N_{clusters}$, within this search area counted, and the core density, ρ_{core}, was calculated using Equation 3.7

$$\rho_{core} = \frac{N_{clusters}}{\pi r^2} \quad . \tag{3.7}$$

Figure 3.27 demonstrates the expected behaviour where the peak core density increases with energy for a fixed amount of material (in this case, 3.86 χ_0). The peak core density increases from 0.3–1.3 clusters/mm^2 for 1–4 GeV for radial distances of approximately 0.1 mm. The values for the peak core density are extremely low and suggest that the shower multiplicities are not high enough to draw any reliable conclusions about the core densities of showers from electrons with energies of less than 5 GeV.

Figure 3.28 contains the core density plots for 4 GeV electrons for various depths of tungsten and supports the previous observation that the shower multiplicities are too low. In general the peak core density increases with the amount of material

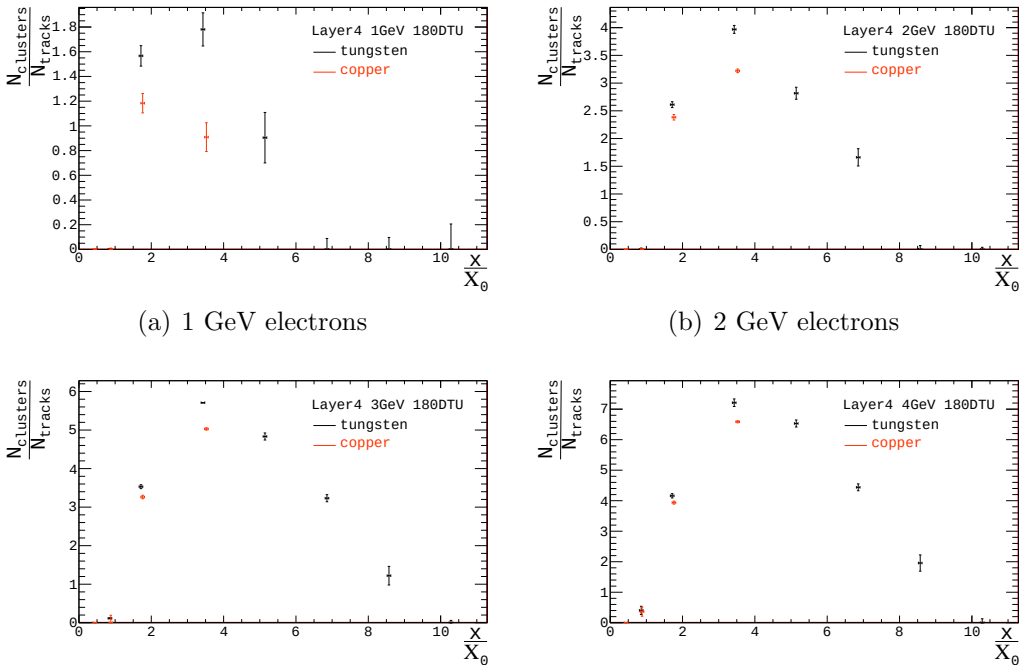

(a) 1 GeV electrons

(b) 2 GeV electrons

(c) 3 GeV electrons

(d) 4 GeV electrons

Figure 3.26: Shower multiplicities from tungsten, shown in black, compared to copper, shown in orange, for the data corresponding to equal numbers of radiation lengths.

up to approximately 4 χ_0 and decreases above this value, mirroring the shower multiplicities. The peak multiplicity in the whole dataset taken at DESY occurred with 3.86 χ_0 of tungsten with a beam energy of 4 GeV. In this configuration, the peak core multiplicity is just 1.3 clusters/mm^2.

The actual peak core density in Figure 3.28 occurs at 0.1 mm with 0.86 χ_0 of tungsten with a mean shower multiplicity of less than one. It is believed that this is due to the reduced probability of a shower having occurred and the beam particle, which has undergone multiple scattering through the tungsten, being detected. The small amount of scattering material produces a small scattering angle and therefore increases the number of clusters observed at small distances from the track projection. This is further evidence that the shower densities need to be studied at higher energies to remove this anomaly.

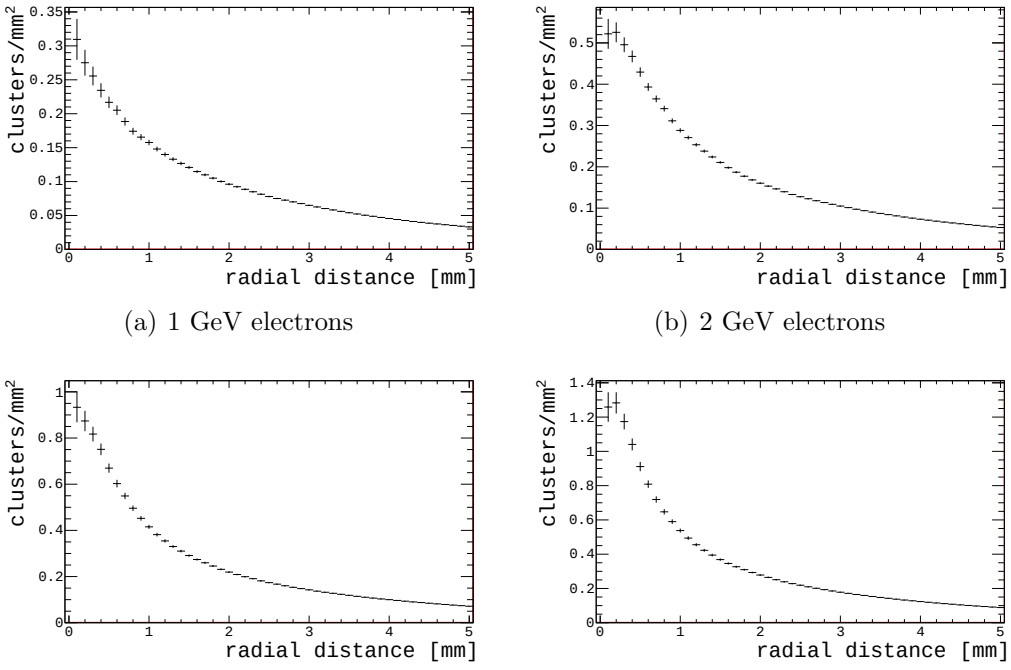

(a) 1 GeV electrons

(b) 2 GeV electrons

(c) 3 GeV electrons

(d) 4 GeV electrons

Figure 3.27: Core shower density with 3.86 χ_0, for 1–4 GeV electrons.

3.5 Simulation

A simulation based on tools within calicedaq[1] was developed to validate the beam test results and attempt to understand the shower density issues. The simulation was divided into two parts:

- *gntSimulation* - A description of the geometry of the beam test setup at DESY (as illustrated in Figure 3.7) was implemented within Geant4.9.4.p02 [82] which utilised the recommended CLHEP 2.1.0.1 [83]. The CALICE validated QGSP_BERT physics list was implemented to handle hadronic interactions whilst six electromagnetic lists were tested for data validation. These electromagnetic lists were; emstandard (default), emstandard_opt1, emstandard_opt2, emstandard_opt3, emlivermore, and empenelope [84]. The incident particle type and energy, alongside the choice of physics list and number of events

[1]the standard readout and data acquisition suite of the TPAC sensors

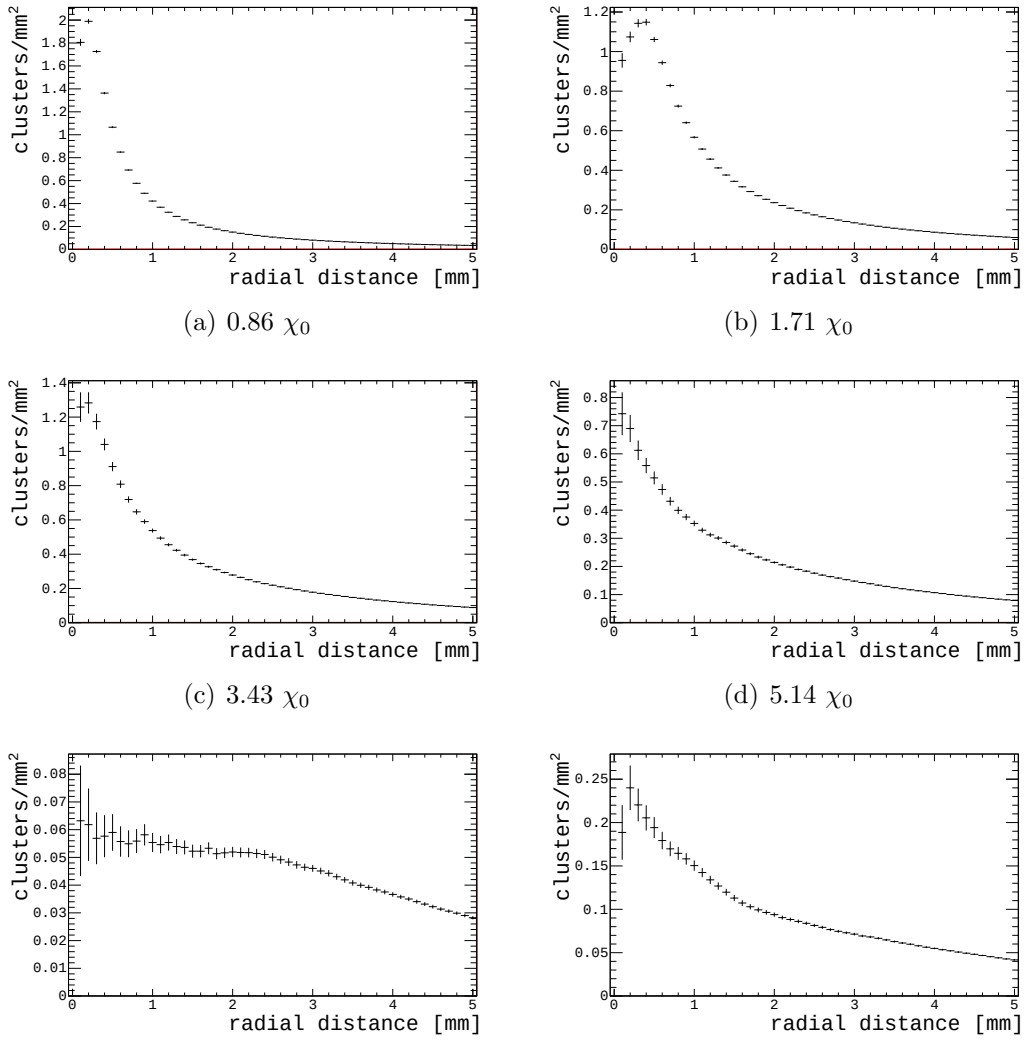

(a) 0.86 χ_0 (b) 1.71 χ_0

(c) 3.43 χ_0 (d) 5.14 χ_0

(e) 6.86 χ_0 (f) 8.57 χ_0

Figure 3.28: Core shower densities for 4 GeV electrons for various amounts of tungsten.

were loaded into gntSimulation via a configuration file.

- *simDigitisation* - The output of gntSimulation was used as an input to simDigitisation where the tracks through the silicon epitaxial layers of the sensors was digitised. Firstly, the charge deposited in a 50×50 μm^2 cell was spread using a 21 point grid acquired from Sentaurus to model the diffusion of the charge within neighbouring pixels [34]. Noise described by a Gaussian distribution was added randomly to the sum of the charge in each pixel. A threshold was set per pixel using calibration factors obtained here [34] to convert charge into

DTU. The hits passing the threshold cut were written to disk in the same format as the beam test data. This allowed identical analyses to be run on both simulation and data.

Simulations were conducted for all of the configurations used during the DESY beamtest with energies of 1–5 GeV, seven material depths of tungsten (1, 2, 4, 6, 8, 10, 12 χ_0) and two digital thresholds (180 and 250 DTU). The simulations were conducted using the Birmingham BlueBEAR [3] cluster. On average, the digitisation process required one minute per event and runs were limited to 1000 events due to time constraints. In total (with all six electromagnetic lists simulated) there were over 500,000 events simulated and digitised across 5000 runs and a total of 548 GB of data.

3.5.1 Energy Deposition

The truth energy deposited in the epitaxial layer of a typical sensor is shown in Figure 3.29. The energy deposition for all lists follows theory as they are heavily Landau dependent due to the ultra thin layers that the particle is traversing. The lists split into two categories when the features of the distributions are analysed. The *emstandard*, *emstandard_opt1* and *emstandard_opt2* lists are all in very good agreement with each other, whereas, the *emstandard_opt3*, *emlivermore* and *empenelope* lists have a much steeper rising edge and higher peak values. The second grouping of lists has an increased number of bins in the physics tables (220 instead of 84) and shorter default ranges of secondary particles compared to the first group [84]. The trailing edge of all the distributions are in a good agreement with each other. There is potential for the digitisation process to have a variable effect dependent on physics list and where the digital thresholds cut the distributions.

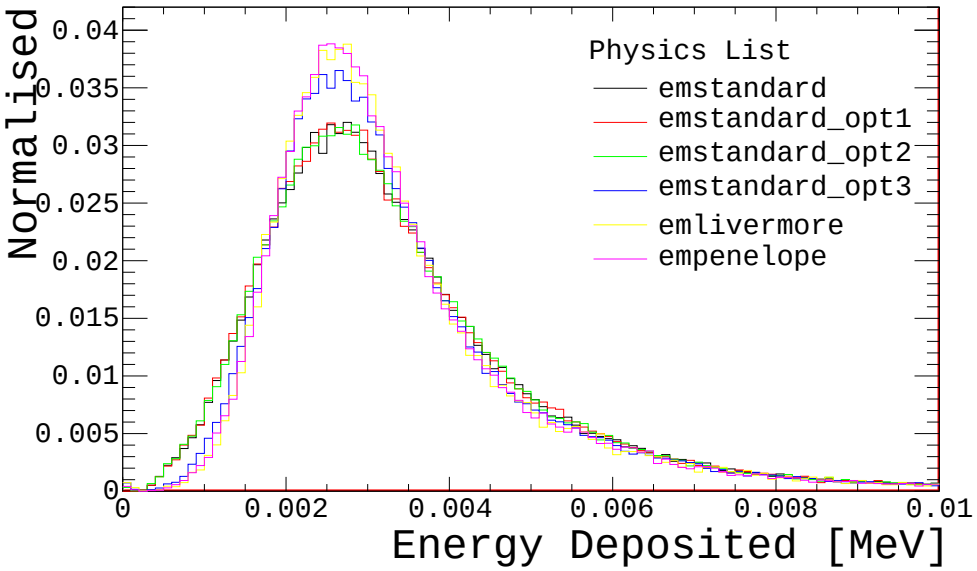

Figure 3.29: Truth energy deposited in the epitaxial layer of a typical sensor for all six electromagnetic physics lists.

3.5.2 Shower Multiplicity

Figure 3.30 demonstrates that the multiplicities of the 180 DTU digitised events as a function of material depth in the various physics lists are in general good agreement with each other, with the exception of the empenelope physics list. However, all of the physics list display a large reduction in the multiplicity compared to the data. Across a large range of material depths the multiplicities in the simulations are roughly a factor of two lower than observed in data, with an even larger discrepancy arising from the empenelope list. The effects are even more evident when looking at the 250 DTU digitised events, where the maximum multiplicity was of order one.

Multiple sources for the discrepancy were postulated and tested in order to improve the simulation including:

- the number of truth particles being modelled incorrectly,
- the sensors suffering from saturation,
- the cluster algorithm clustering multiple hits into one cluster,

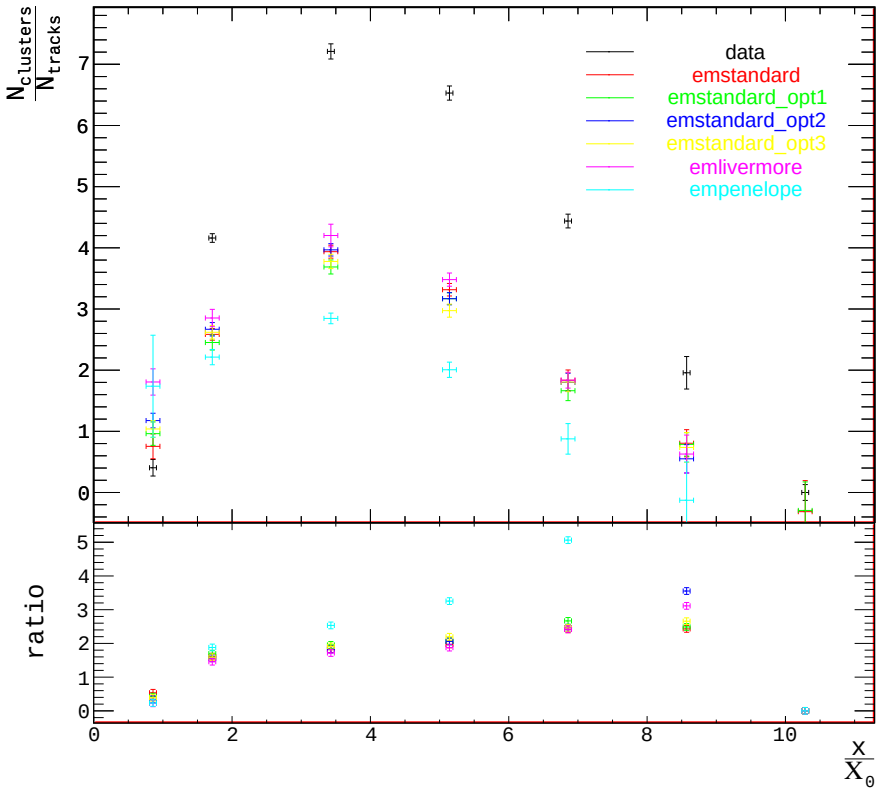

Figure 3.30: The mean multiplicities as a function of material depth for data taken with tungsten targets and digitised simulations for various physics lists at a threshold of 180 DTU

- the energy deposited in the 12 μm of silicon being modelled incorrectly,
- the charge spread within the pixels being too large, and
- the threshold calculations being wrong.

The charge spread models and threshold conversion factors have previously been validated against data taken with the TPAC sensor. For completeness the effect of these factors are still considered a source of discrepancy here.

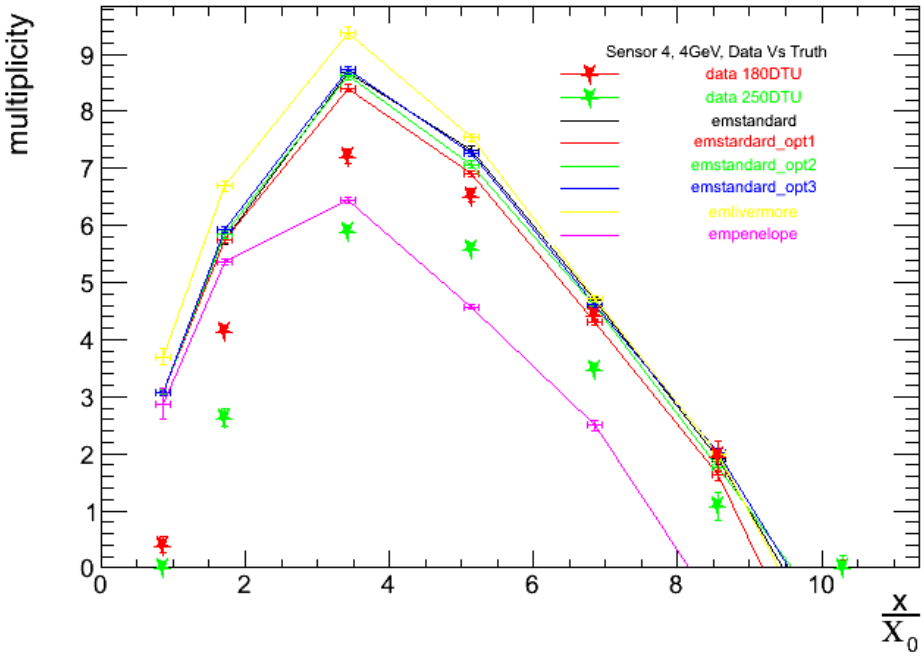

Figure 3.31: The simulated number of truth particles reaching the sensor in layer4 for various physics lists compared to the number of particles in the same sensor observed in data taken at DESY.

Number of Truth Particles

The number of truth particles reaching the sensor located in layer4 of the stack are compared with data in Figure 3.31. The emlivermore physics list yields the largest shower multiplicities with the four emstandard lists being in good agreement and empenelope yielding a much lower truth multiplicity. This trend follows the same pattern as the digitised hits in Figure 3.30 and is an indication that the differences in the rising edge of the energy deposition profile are not important in the digitisation process.

All of the physics lists (except empenelope) produce more truth particles than are observed in data for values of x/χ_0 <5. This is indicative of technical issues with the modelling of low energy particles through a large amount of material in Geant4.

Saturation and Clustering

The truth tracks were superimposed onto the digitised pixel hits and the mean number of truth tracks per pixel was found to be $\leq$1.01 for all physics lists across all energies and material configurations. In much the same way, the truth tracks were projected through all found clusters to observe the effect of the clustering algorithm on nearby tracks. A mean number of tracks per cluster of $\leq$1.01 was also observed for all configurations. Therefore, the effect of saturation and the clustering algorithm does not account for the loss of hits during the digitisation process.

Energy Deposition, Charge Spread and Thresholds

On average, 35% of the energy deposited in the struck pixel remained in the pixel after charge spread had been applied. The distributions for the remaining energy in the struck pixel after the charge spread had been applied are shown in Figure 3.32, where the differences in the shapes from Figure 3.29 have been mostly washed away. The peak heights for emstandard_opt3, emlivermore and empenelope are still marginally greater than the other lists. Also shown are the threshold cuts of 180 DTU and 250 DTU. These thresholds cut at undesirable points on the distributions. To maintain a high efficiency one would like the cuts to be applied in the lower region of the rising edge. However, the cut at 180 DTU occurs in the peak removing a huge amount of hits and the cut at 250 DTU sits on the tail and removes almost all of the hits. The efficiencies achieved are summarised in Table 3.5.

At this stage the positions of the cuts relative to the energy deposition could be explained by any combination of three variables:

- the energy deposition in Geant4, which at these low energies and thin materials is unverified and could be wrong,
- the modelling of the charge spread algorithm is incorrect, although these were performed using industry approved methods, and (or)

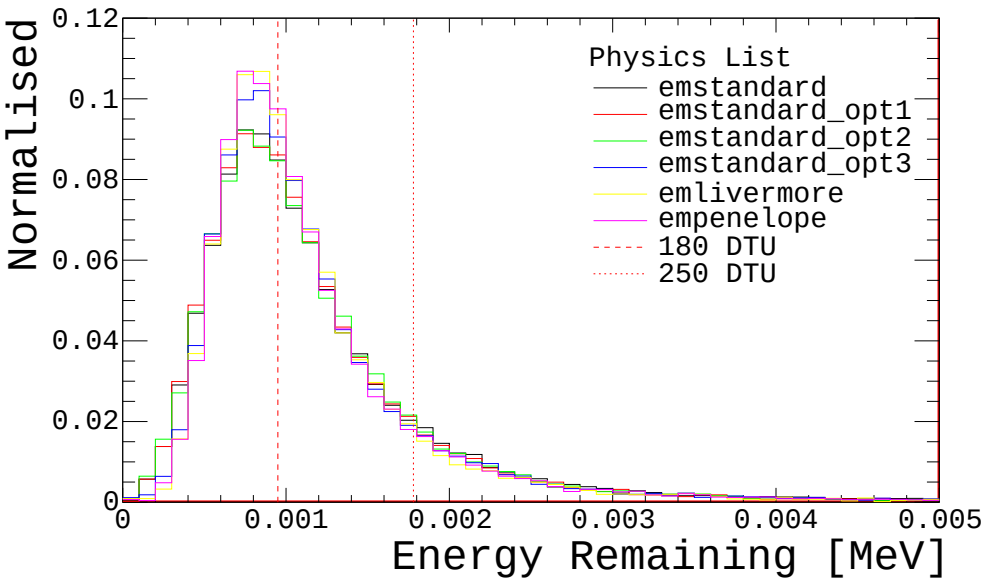

Figure 3.32: Energy remaining in the struck pixel in a typical sensor for all six electromagnetic physics lists after charge spreading has been applied. The threshold cuts for 180 DTU and 250 DTU are also shown.

- the conversion between threshold to charge is incorrect but this has been verified with beam test data for the TPAC sensors.

The balance between these effects is very fine due to the tiny amounts of energy which are being deposited in the silicon and many attempts were made to identify the underlying reasons as shown in Appendix B. As none of the attempts could improve the realism of the simulation, a lack of time and man power meant the simulations to describe the beam test results had to be abandoned.

Table 3.5: Calculated efficiencies for the six physics lists at 180 DTU and 250 DTU alongside the values in data for reference.

	180 DTU	250 DTU
data	0.82±0.02	0.67±0.01
emstandard	0.38±0.03	0.11±0.01
emstandard_opt1	0.35±0.03	0.08±0.01
emstandard_opt2	0.36±0.03	0.10±0.01
emstandard_opt3	0.36±0.03	0.09±0.01
emlivermore	0.31±0.03	0.09±0.01
empenelope	0.33±0.03	0.08±0.01

In recent releases of Geant4 a new extremely low level electromagnetic physics list has been implimented which aims to describe the interactions of low energy particles in thin layers of silicon (MuElec [85]). Although the testing of this list is beyond the scope of this thesis, a description of particles down to energies of just 5 eV could have an impact on the performance.

3.6 Conclusions

The performance of the TPAC sensors has been successfully tested with the sensors being subjected to beam tests using pions and electrons at CERN and DESY respectively.

Testing of the electrical properties of the sensors have yielded results consistent with the design specification. In particular, the monostable length and noise rates, which are controlled by multiple electrical components, have been studied and demonstrate that the internal workings of the sensors are well understood. Running at DESY was conducted with unmasked sensors leading to higher noise rates than at CERN, which provided additional complications for the shower multiplicity and density studies. The properties of this noise were investigated and the noisy pixels were successfully removed during the analysis, restoring the low noise performance to the DESY data above 180 DTU.

A stack of six sensors operated successfully and tracks were formed through the stack to allow properties such as cluster sizes and single particle efficiencies to be studied. The high resistiviy sensors demonstrated an improved single particle efficiency over the standard sensors at higher thresholds.

The tracks were then used as part of the event selection to study the multiplicity of electrons showering through a tungsten target. An increased multiplicity was observed for electrons with higher incident energies in the sensors downstream of the showering material, demonstrating an essential property of a DECAL. For a fixed

energy the multiplicity for increasing amounts of material follows the same trend as the energy deposition rate in a conventional ECAL. This result is especially pleasing due to the shower being wider than the sensor size causing an incomplete measurement of the shower. With a larger physics prototype excellent, highly granular measurements of an electromagnetic shower should be possible.

Initial measurements of the core shower densities were made but a combination of the low incident energies and incomplete shower containment prevented conclusive measurements being made.

A two stage simulation was developed in an attempt to validate the beam test results. However, due to the fine interplay between tiny energy deposits, charge spreading and threshold conversion factors the efficiency of digitised hits returned vastly lower than expected particle efficiency results. A large amount of time was invested in trying to improve the simulation before it was finally abandoned due to time constraints, concluding that the underlying problem was likely to be in the modelling of energy deposition in Geant4.

CHAPTER 4

Radiation Testing of TPAC

4.1 Introduction

The TPAC sensor was primarily designed for use within the ECAL system of a detector at the ILC. However, funding restrictions prevented the development of a full scale prototype to fully characterise the sensors performance within a calorimeter setup. Alternative uses for the technology in the TPAC sensors have been proposed such as the upgraded Inner Tracking System (ITS) of the ALICE detector at the LHC [86], the calorimeter systems of the CLIC ECAL, and the vertex systems of the proposed SuperB Collider [87]. The sensors for such applications need to be radiation hard to ensure that they operate with the required performance for the lifetime of the sensors in high radiation environments. Previous studies have demonstrated a wide tolerance of CMOS sensors to radiation, ranging from sensors that can withstand greater than 1 Mrad [88] to sensors that can withstand just a

few krad [89] [90]. Creating a radiation tolerant sensor was not one of the key design goals of the TPAC sensor due to the low radiation levels within the ECAL at the ILC and, as such, it was essential to characterise the response to radiation for future applications.

This chapter describes the modifications made to the sensors to allow the radiation hardness tests to be carried out, and the verification of such modifications; the methods used to characterise the sensors; the procedures carried out to irradiate the sensors and the measures which where taken to control the results; the analyses carried out, and the results obtained, including the changes to the noise and pedestal of the sensors, the signal readout and finally the signal to noise ratio of the pixels.

Preliminary studies with the data obtained for this chapter were shown at TiPP2011 [73] and the final results were published in the Journal of Instrumentation [1].

4.2 Sensor Modifications

The sensor PCBs were modified for the radiation studies to allow the sensors to be replaced quickly and easily between tests. In the old design, a sensor was bonded directly onto the PCB. Once the sensor had been tested to destruction, the process to remove it and have a new one bonded onto the PCB was expensive and time consuming. Figure 4.1 illustrates the new PCB layout. Figure 4.1(a) shows the simple Chip on Board (CoB) onto which the sensors were bonded and Figure 4.1(b) shows the new pins that were added to the PCB to allow these CoBs to be clipped into place. For the remainder of this chapter the modified PCB will be referred to as the "mainboard" and the words CoB and sensor will be used interchangeably. The cost of the CoBs was significantly less than the mainboards and therefore a large number were ordered and 12 sensors bonded onto these. Two mainboards were used during the studies, one to readout the sensors, and one to power the sensors during irradiation. This setup ensured that the mainboard used to read out the sensors did not receive any dose, and as such its characteristics did not change between tests.

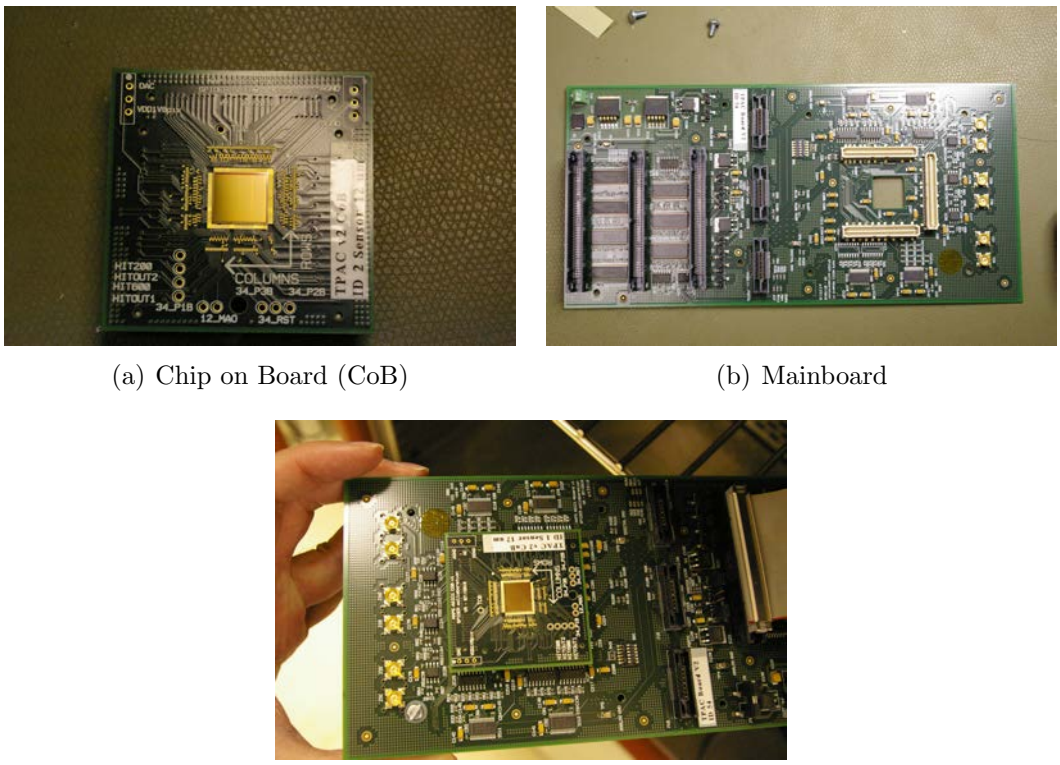

(a) Chip on Board (CoB)

(b) Mainboard

(c) CoB and Mainboard

Figure 4.1: Photographs of the new CoBs (4.1(a)), the modified mainboard with the new long white pins for the CoBs to clip into (4.1(b)), and a CoB clipped into place in the mainboard (4.1(c)).

4.3 Sensor Characteristics

Each pixel is characterised by its pedestal and noise value. Both of these are found by performing a threshold scan on each pixel and looking at the number of hits as a function of the threshold. The threshold scans were conducted in a darkened box to ensure that there was no interference from background photons causing genuine hits in the sensors. The results of such a scan for a typical pixel are shown in Figure 4.2 where the mean value is the pedestal of the pixel and the width is the associated noise. Carrying out scans for all pixels in a sensor gives two corresponding spectra for each device (Figure 4.3). The pedestal spectra were fitted with a simple Gaussian and the mean value extracted along with the corresponding error. The noise spectra were fitted using a Gaussian convoluted with a Landau distribution where the noise

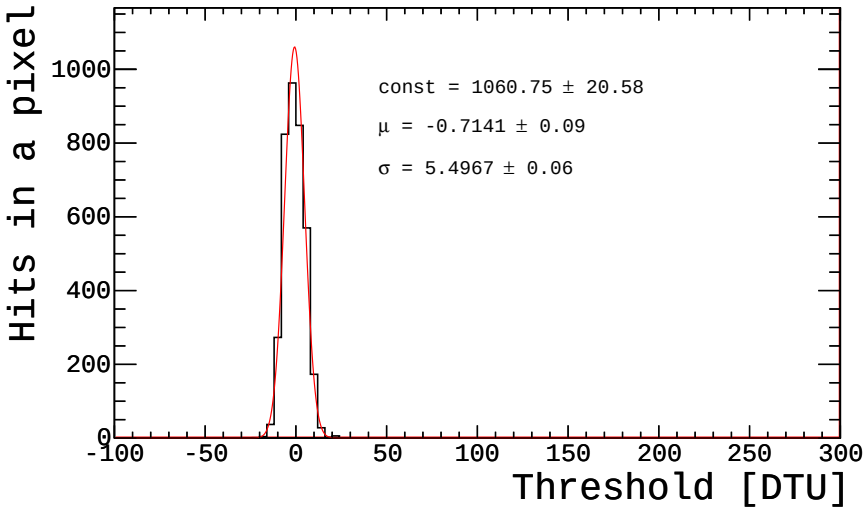

Figure 4.2: The results of a typical threshold scan on a single pixel where the mean is the pedestal and the width of the Gaussian is the noise in the pixel.

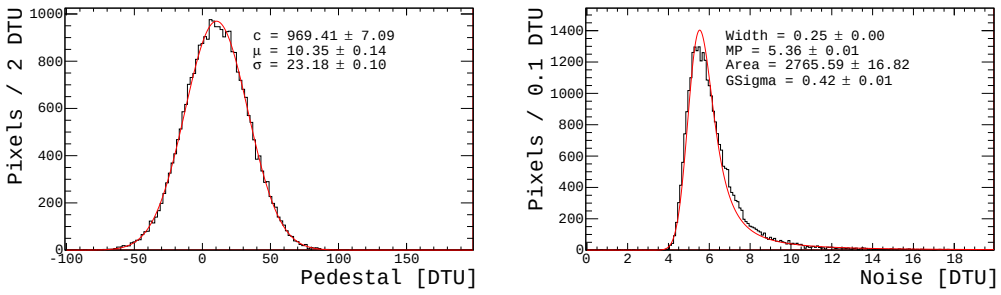

(a) Pedestal

(b) Noise

Figure 4.3: Example of the pedestal and noise spectra formed from scanning all 28224 pixels in a sensor with the fits overlaid.

corresponds to the fit maxima.

4.3.1 Sensor Trimming

Prior to the radiation tests the performance of the new mainboard–CoB system needed to be verified. One of the fundamental tests to achieve this was to assess the quality of the sensor trimming process. In the old PCB setup, the sensors were trimmed such that the pedestals of all the pixels were consistent during operation [34]. This was achieved by loading optimised trim values into the pixels via the shift

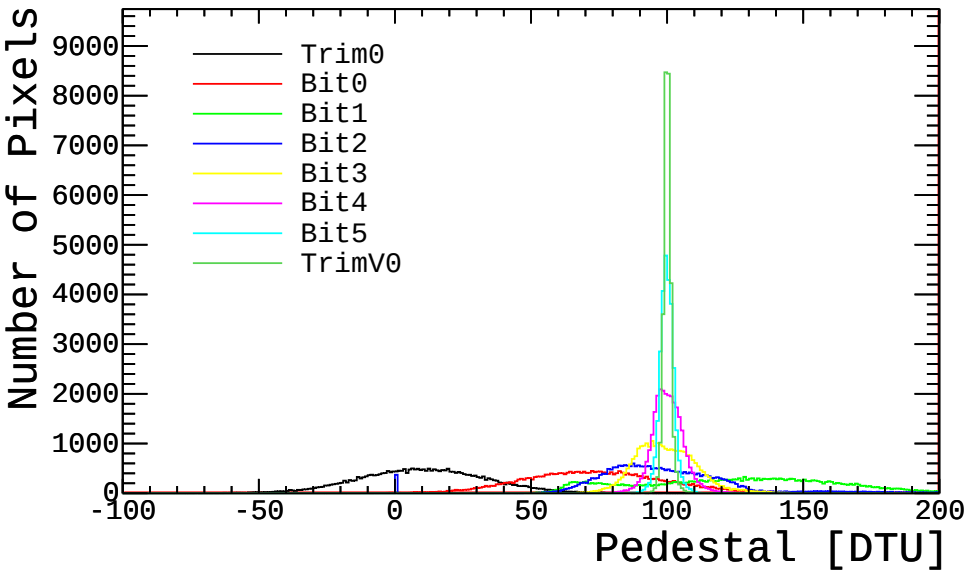

Figure 4.4: The progression of the pedestals during sensor trimming of the new mainboard–CoB system for no trim values (Trim0), optimising the 6 trim bits (Bit0–5), and after the optimised trim values have been applied to the sensor (TrimV0).

register. The trim value is a six bit number which adjusts the pedestal of the pixel.

The trim values were optimised by iterating over the six bits for each pixel. This required 8 full scans of the sensor, one with a zero trim value, six to iterate the bits, and one with the trim values loaded into the pixels to check the performance. Figure 4.4 shows the progression of the pedestals as the trim values were optimised. When compared to the sensor trims in [34] the results of the trimming procedure are improved. This is not a result of the new CoB and mainboard but the addition of two extra trim bits from the TPACv1.0 to TPACv1.2 sensors. It does however demonstrate that the readout from the new setup works and could be used for the radiation studies.

4.3.2 Effect of Mainboard

As the sensors could now be switched between mainboards it was essential to investigate and understand any differences in the behaviour of each mainboard–CoB pairing.

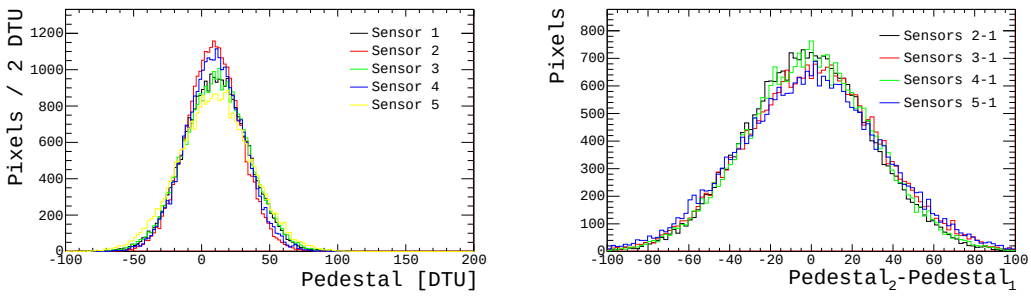

(a) Pedestal: Whole sensor

(b) Pedestal: Pixel comparisons

Figure 4.5: Comparisons between the pedestal values of different sensors on the same mainboard for sensor wide properties and on a pixel by pixel basis where the pedestal values of sensors 2–4 were compared with the values from sensor 1.

Threshold scans were performed using five sensors bonded to different CoBs plugged into the same mainboard. Figure 4.5(a) shows that the overall sensor characteristics are the same when different CoBs are paired with the same mainboard. However, Figure 4.5(b) shows that the pixel-by-pixel threshold comparison are very different between sensors. Although this result in not unexpected, it does indicate that the trimming procedure would need to be carried out on each individual sensor on a mainboard. Due to time constraints this was not possible and untrimmed sensors were used during the radiation tests.

4.4 Radiation Tests

During the radiation tests the sensors were irradiated with 50 keV x-rays created using a Seifert RP149 radiation source. Figure 4.6(a) shows the experimental setup used. The sensors were positioned in such a way that the distance from the sensor surface to the tube window was 17.5 cm, producing a circular beam 8 mm in diameter with a uniformity of 10 %. The dose rate was varied by adjusting the operating current, with a dose rate of 60(6) rad/s achieved with a current of 50(5) mA. As the beam diameter is smaller in size than the sensitive area of the TPAC sensor care had to taken to ensure that the beam was aligned correctly between runs to

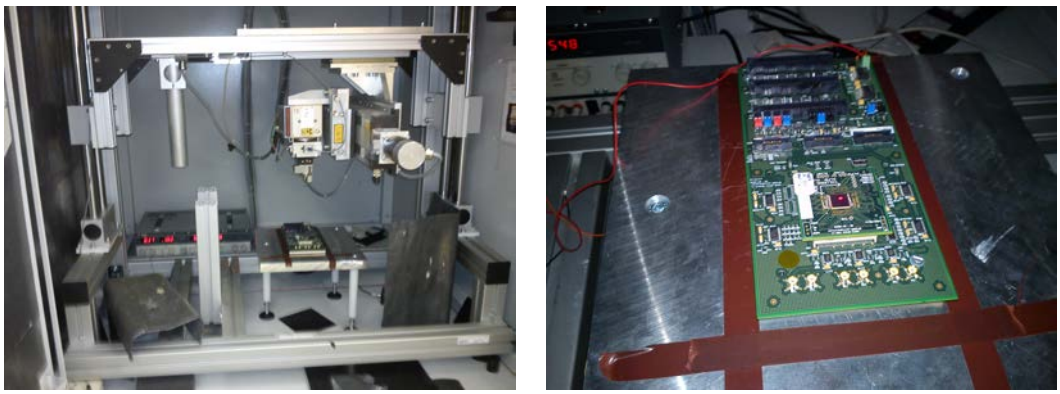

(a) Experimental setup (b) Sensor alignment

Figure 4.6: Photographs of the experimental setup used to irradiate the sensors. 4.6(a) shows the inside of the Seifert RP149 box with the PCB placed on a stand beneath the x-ray source, the required power supplies and the lead shielding. The alignment tools are shown in 4.6(b) where the laser point can be seen on the sensor surface.

achieve the highest possible uniformity in the integrated dose. Figure 4.6(b) shows the tape marks used for the rough alignment of the sensors and a laser pointer for fine tuning. The mainboard was protected from the x-rays using a lead shield with a 1.5×1.5 cm square window located above the sensor.

The x-rays in this setup will liberate electrons in the silicon with a maximum energy of 50 keV which in turn, will impart a maximum of 0.19 eV upon a recoiled silicon atom. In silicon, the displacement damage threshold is 21 eV [91] and as such the damage to the sensors cannot be in the bulk and must be due to surface effects such as charge trapping at boundary interfaces.

Eight sensors were irradiated, under two different bias voltages, 0 V and 1.8 V (ground and operating voltages) up to doses of 5000 krad and 200 krad respectively, as summarised in Table 4.1. Also studied were the effects of dose rate, with the sensors exposed at 60 rad/s and 6 rad/s, and the effect of using a high resistivity epitaxial layer. The sensors held at ground were exposed in various dose steps of between 200 krad and 1000 krad, while the sensors held at 1.8 V were exposed in steps of 20 krad.

After each dose the pixels were measured to quantify the effect of the radiation.

During the radiation tests the sensors were used untrimmed and the *changes* in the noise and pedestal, rather than their absolute values, were the characteristics of interest. The fractional changes to the noise were calculated using:

$$f\Delta_{Noise} = \frac{X_{\text{Dose}} - X_{\text{0krad}}}{X_{\text{0krad}}} \quad , \tag{4.1}$$

and the pedestal shift was calculated using:

$$\Delta_{Pedestal} = X_{\text{Dose}} - X_{\text{0krad}} \quad , \tag{4.2}$$

where X_{Dose} and X_{0krad} are the noise (pedestal) values for a specific dose and zero dose respectively. The fractional changes to the pedestal were not calculated as the pedestal of an untrimmed sensor is approximately zero leading to large relative values.

Between irradiations the sensors were kept in a freezer at $-20°$C to limit the amount of annealing. As a threshold scan on all of the pixels in the sensor took approximately 6 hours only a quarter of the sensor was scanned following each irradiation. This was essential as the annealing in the sensors was accelerated during scanning due to the increased operating temperature of the sensors and this could have caused discrepancies in the results.

4.4.1 Noise and Pedestals - Bulk Pixels

Unpowered sensors

Four standard sensors were held at ground during the exposure, with two receiving integrated doses of 1000 krad and the others receiving 5000 krad, all at a dose rate of 60 rad/s. These studies were conducted as a preliminary investigation into the sensors behaviour and allowed a comparison to be made between the effects of bias

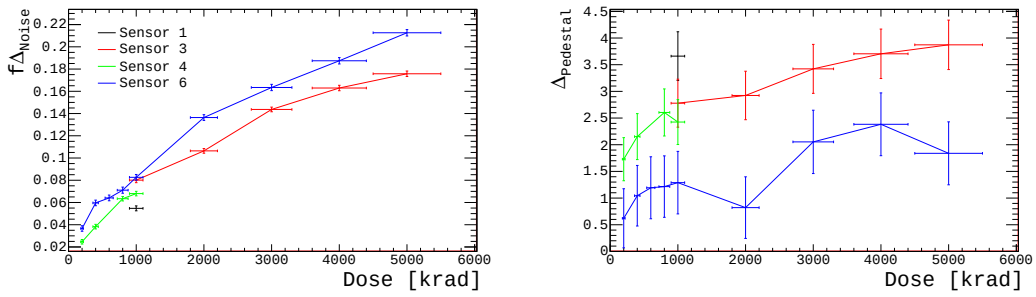

(a) Fractional noise changes

(b) Pedestal shifts

Figure 4.7: The variation in noise and pedestal for sensors held at ground during irradiation. 4.7(a) shows the fractional changes in noise and 4.7(b) the absolute changes in pedestal from zero dose for the four sensors held at ground during exposure.

in the sensors during exposure. The sensor was held at ground to avoid charge build up in the sensors by connecting the grounds on the CoB to a power supply.

At 1000 krad the noise increased in all sensors by between 5 % and 8 %. Pairs of sensors 3 and 6, and sensors 1 and 4 were in good agreement within each pairing. At 5000 krad the noise in sensor 3 had increased by 18 % and sensor 6 by 21 % as shown in Figure 4.7(a).

Over the same range of doses, Figure 4.7(b) shows that the pedestals also increased between 1.3 DTU (10 %) and 3.7 DTU (25 %) at 1000 krad, rising to a maximum increase of 3.9 DTU (35 %) at 5000 krad. As the changes in the noise and pedestals were different this suggests that there could be multiple sources of damage to the sensors caused by the radiation.

Powered sensors

Four additional sensors were exposed to radiation whilst held at their operating voltage of 1.8 V. Two of these were standard sensors, and the third was a high resistivity 18 μm sensor; all three were irradiated at a dose rate of 60 rad/s. The fourth sensor was a standard sensor with a dose rate of 6 rad/s in order to test whether the results were rate dependent. Due to problems with loading configuration

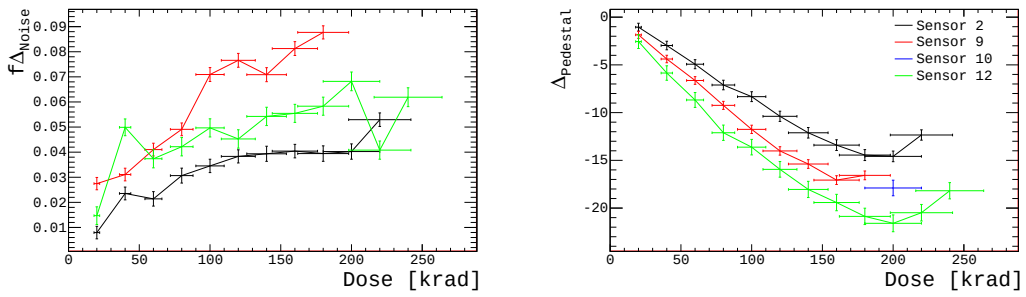

(a) Fractional noise changes

(b) Pedestal shifts

Figure 4.8: The variation in noise and pedestal for the sensors powered during irradiation. 4.8(a) shows the fractional changes in noise and 4.8(b) the absolute changes in pedestal from zero dose for the four sensors held at operating voltage during exposure. Sensor 10 was exposed at the lower rate of 6 rad/s and sensor 12 was the 18 μm high resistivity epitaxial layer.

data on to the sensors (see Section 4.4.1) the powered sensors were only exposed to small integrated doses of between 200 krad and 240 krad in stages of 20 krad.

Figure 4.8(a) shows that the noise once again increases as a function of dose, with a maximum increase of 9 % in sensor 9. The noise changes in the powered sensors at 200 krad (4% to 8 %) coincide with the noise changes in the unpowered sensors at 1000 krad (5 % to 8 %) implying that bias in the sensors accelerates the increase in the noise (see Table 4.1). The noise in sensor 10 was observed to fall slightly. Although this sensor was exposed at the low dose rate it is believed that the decrease is more likely to be an artefact of the fit used to extract the noise.

The behaviour of the pedestal when the sensors were powered during irradiation was found to be very different to those that were held at ground. Figure 4.8(b) demonstrates that, when powered, the pedestal actually decreases with dose in all of the sensors up to ∼200 krad. A lower pedestal during sensor operation will lead to an increase in the noise rate of the sensors and this could be a very important feature at higher doses. The dose rate does not affect the pedestal shifts as the change in sensor 10 is in good agreement with the other sensors.

In the high resistivity epitaxial layer (sensor 12) the fractional changes in the noise are in agreement with the standard sensors. The pedestal actually decreases more

than the standard sensors. This once again implies that there could be multiple sources for the damage to the sensor, an epitaxial layer independent source (noise) and an epitaxial layer dependent source (pedestal).

The pedestal changes actually decreased at the higher doses because problems with the shift register meant that the sensors underwent annealing whilst waiting for the sensors to be scanned. This set the limit on the maximum dose for which reliable characterisation of the sensors could be performed, as described below.

Shift Register Problems The configuration data is loaded on to the pixels by a three-phase clock shift register and these data contain the trim values of each pixel as well as the pixel masks, which can be used to define a set of pixels to be excluded from the readout. In the TPAC sensor, if more than a few hundred pixels fire at the same time, noise pick-up is observed in the pixels [35]. To work around this problem, during a threshold scan only one column of 168 pixels was unmasked at a given time. At the higher doses the values read in to and subsequently returned from the shift register were different in some pixels. Due to the nature of the shift register structure, a single bad register in a column of pixels can corrupt the whole column. This leads to the possibility of the mask values in an entire column being invalid and unmasking an additional 168 pixels during the scan. If there are too many bad columns it can prevent the sensor being reliably read out until the shift register is repaired. There are two potential ways of repairing the shift register; adjusting the voltage that drives the shift register; or allowing the sensor to anneal.

Figure 4.9 shows the number of bad columns in the shift register for various shift register supply voltages at doses of 0, 100, 200, and 220 krad for sensor 2. This sensor had one bad column in the shift register before exposure so it was essential not to develop any more. It is clear that at 100 krad there is a large range of voltages over which just one bad column is present in the register, so the sensor functions correctly. At 200 krad this behaviour has changed so that there is no voltage at which the register has just one bad column and with a further increase in dose up

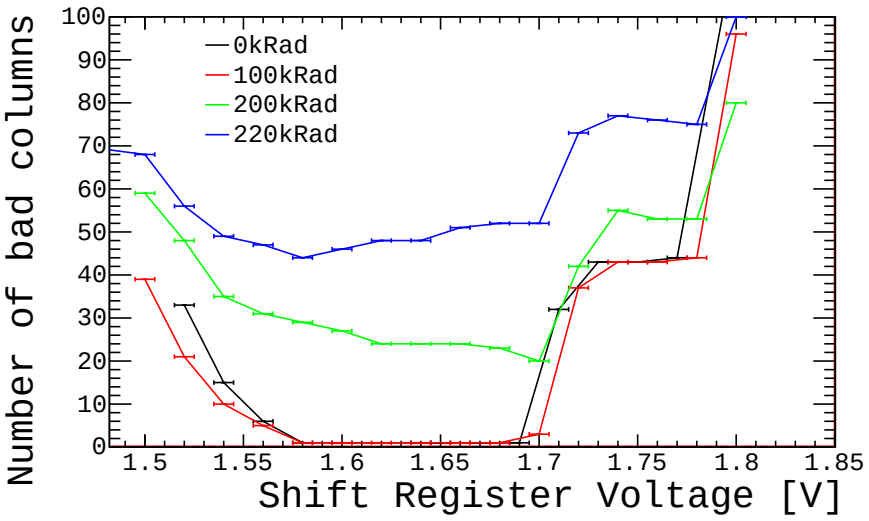

Figure 4.9: The number of bad columns in the shift register as a function of supply voltage for various doses of a standard 12 μm sensor.

to 220 krad the number of bad columns has significantly increased. At these higher doses, adjusting the supply voltage does not solve the issue and as such the register must be allowed to anneal.

With the shift register supply voltage fixed at the design voltage of 1.65 V, the behaviour was studied in 30 minute intervals until the number of bad columns was sufficiently small that the sensor could be reliably read out. Figure 4.10 reiterates the increased number of bad columns with a higher dose and shows the progression of the recovery of the shift register. The time to recover increased from 300 minutes to 1400 minutes for 200 and 220 krad respectively. Because these large waiting times allow the damage to the sensor to anneal away, it was not possible to carry out measurements at the larger doses.

When the dose rate was reduced by a factor of 10, the shift register problems were vastly reduced. At 200 krad there were just three bad columns in the sensor exposed at the reduced rate compared to more than 20 for the other two standard sensors (see Figure 4.11). This suggests that the shift register is annealing during exposure. When the sensors are held at ground during exposure the shift register behaves as expected up to very high doses so the bias in the sensor is impeding the

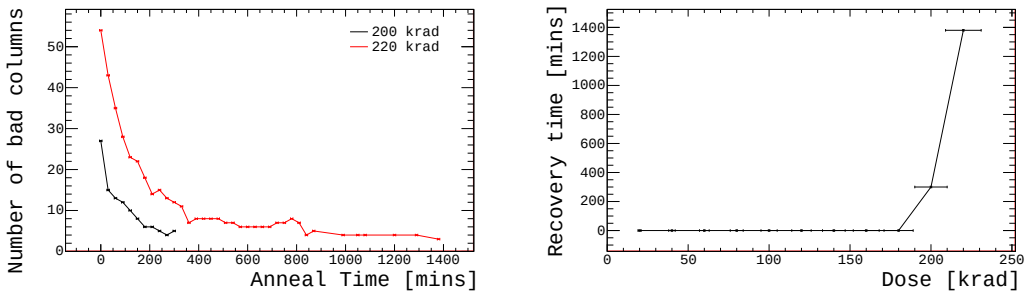

(a) Bad columns versus anneal time

(b) Recovery time versus dose

Figure 4.10: 4.10(a) shows the number of bad columns versus anneal time for two different doses and 4.10(b) demonstrates the total anneal time before the sensor could be reliably scanned versus dose for the same sensor.

recombination of the electron-hole pairs created by the radiation. As the pedestal shift in the low dose rate sensor is equivalent to the shift in the other sensors this implies that the damage to the shift registers is rate dependent and the damage causing the pedestal changes is rate independent. Due to this, in the low radiation level environments of a calorimeter system the sensor should be able to withstand integrated doses higher than those tested as the dose rate will be significantly lower.

4.4.2 Signal - Analogue Test Pixels

The shape and the characteristics of the signal in the pixels were studied using the two analogue "test" pixels. The sensors were once again placed in a darkened box to reduce the hits in the sensors from light photons and an Fe-55 source was placed adjacent to the test pixels. The two test pixels were connected to a high rate oscilloscope, a threshold of 140 mV was set in the pixels and any signal in the pixels greater than this threshold had the shape measured and recorded. As the test pixels do not possess the capability to trigger on a signal the oscilloscope used the two inputs from the pixels as a trigger. To ensure there was a genuine event in one of the pixels the trigger required a signal from one of the sensors above threshold whilst the other remained below. The minima of the signal was found by fitting a second order polynomial (see Figure 4.12(a)) and Figure 4.12(b) shows the resulting

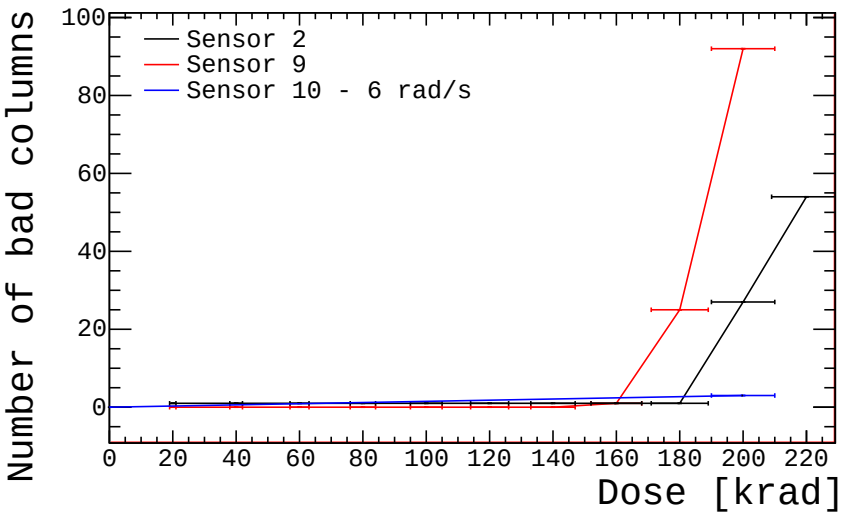

Figure 4.11: The number of bad columns versus dose for the two standard sensors exposed at a rate of 60 rad/s and the standard sensor at 6 rad/s (sensor 10).

energy spectrum which was built up over multiple events.

Fe-55 produces gamma radiation with two characteristic photons, k_α and k_β, having energies of 5.9 keV and 6.5 keV respectively. The k_α peak is the dominant decay with the k_β having a reduced rate. When the photons deposit energy in 12 μm silicon at normal incidence they will liberate 1620 e^- and 1778 e^- respectively. When one of the photons from the decay interacts directly with one of the diodes in the sensor, all of the energy is collected and the full characteristic energy peaks are observed in the spectrum. If the photon interacts in the epitaxial layer outside of the diodes, charge diffusion leads to charge being lost into neighbouring pixels. The amount of charge lost is dependent on the location of the initial photon and therefore there are many events which see a charge collection below the characteristic peaks [34]. The gain of the sensors can be calculated using the k_α peak, where all 1620 e^- are collected by

$$Gain = \frac{Signal[\mathrm{mV}]}{1620e^-} \quad , \tag{4.3}$$

where *Signal* is the mean value of a Gaussian fit to the k_α peak.

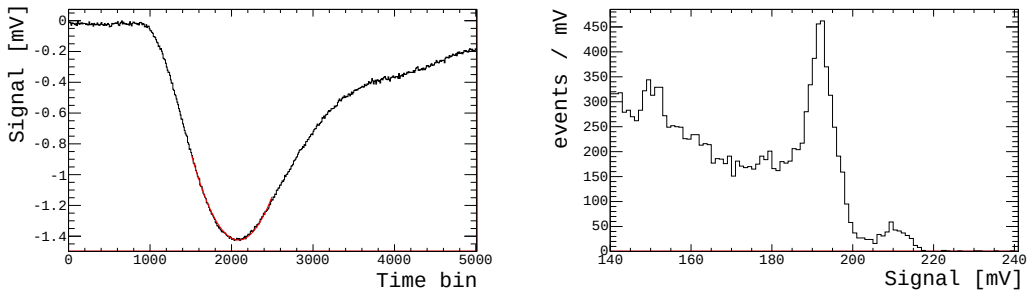

(a) Fitted oscilloscope trace

(b) Example signal spectrum

Figure 4.12: An example of the oscilloscope trace of an Fe-55 event with fit overlaid (4.12(a)), and the resulting spectrum created using the minima of each event (4.12(b)).

To collect a sufficient number of events to resolved the k_α peak a single Fe-55 scan took approximately 24 hours. For this reason the signal could only be studied after a long period of annealing to ensure that the sensors were in a stable state. The signal was studied in four sensors. Three of the sensors were powered during the exposure and the fourth was held at ground and received a much higher integrated dose. Figure 4.13 shows the spectra aquired for all four sensors. Prior to the sensors being exposed, the k_α peak positions agreed within an acceptable spread of 10.8 mV. The k_α peak in sensor 12 has an increased width due to the additional charge collection adjacent to the sensor diodes in the high resistivity silicon. Post exposure, the position of the k_α peak increased in all of the sensors with a final spread of 9.4 mV.

4.4.3 Signal to Noise

Table 4.2 gives a summary of the signal and gain for the test pixels obtained with the Fe-55 scans, and the noise of the bulk pixels from the threshold scans in DTU. Although the observed signal and gain increased with radiation, the critical quantity is the signal to noise ratio (S/N). The fractional change was calculated using Equation 4.1 whilst S/N was given by

$$\frac{S}{N} = \frac{Signal[\text{mV}]}{Noise[\text{mV}]} \quad , \tag{4.4}$$

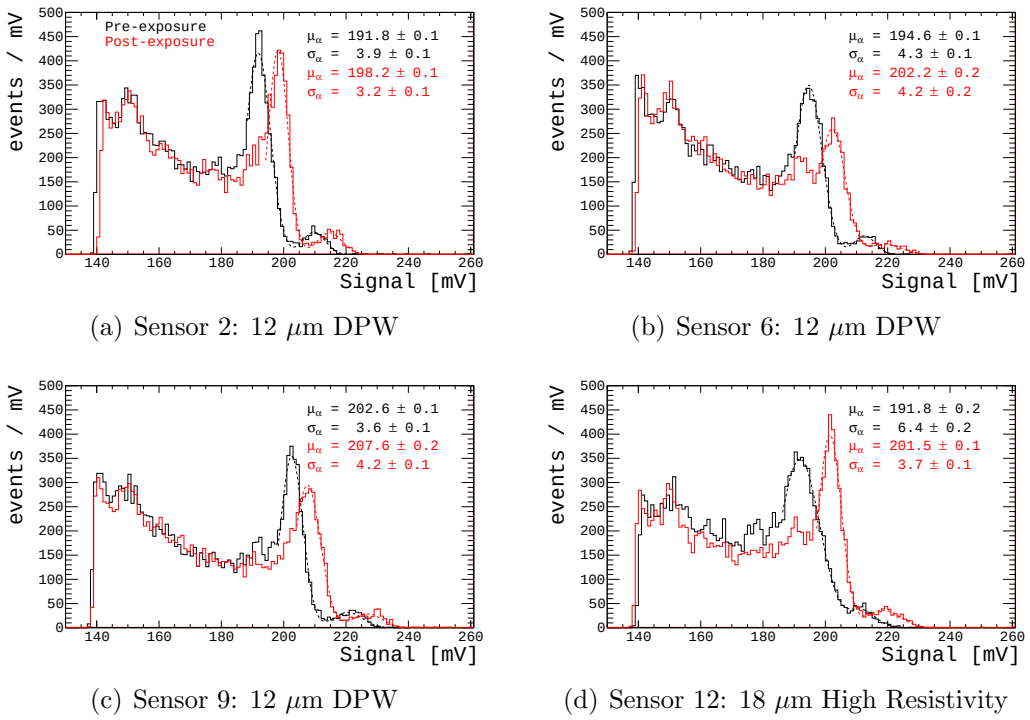

(a) Sensor 2: 12 μm DPW

(b) Sensor 6: 12 μm DPW

(c) Sensor 9: 12 μm DPW

(d) Sensor 12: 18 μm High Resistivity

Figure 4.13: The charge collection spectra for all sensors before and after irradiation and annealing where black is pre and red post exposure for sensors 2, 6 (unpowered), 9, and 12 (high resistivity).

where *Signal* is the position of the k_α centroid and *Noise* is the noise taken from the threshold scans (in DTU) converted into mV by

$$Noise[mV] = Noise[\text{DTU}] \times C[e^-/\text{DTU}] \times Gain[\text{mV}/e^-] \quad , \tag{4.5}$$

where C is the conversion factor of DTU to electrons (3.3 e^-/DTU [35]), and *Gain* is calculated using Equation 4.3. The values of the noise in electrons and mV are also given in Table 4.2.

Across all four sensors, S/N was observed to decrease after irradiation. When the sensor was powered during irradiation S/N decreased by between 4 % and 8 %. The results for the high resistivity sensor (6±1 %) were consistent with the two standard sensors (4±1 % and 8±1 %) demonstrating that the changes in S/N are independent of the epitaxial layer. The sensor irradiated at ground up to 5000 krad underwent a

S/N decrease of 15±1 % showing that the sensor is capable of receiving large doses with a relatively small effect on S/N.

4.5 Conclusions

It has been shown that the noise in the TPAC sensors has increased by between 2.5 % and 8 % at 200 krad for various sensor bias rising to 21 % at 5000 krad for a sensor held at ground during exposure. The S/N has been shown to fall by a maximum of 8 % in sensors at a dose of 200 krad. At 5000 krad, the S/N has reduced by just 15 % which is very promising for future applications.

It has been demonstrated that changes in S/N are independent of epitaxial layer type as the sensors irradiated whilst powered were all in agreement. When the sensors are irradiated whilst powered, problems develop in the shift register leading to the need for a redesign of the shift register in future iterations of the sensors. The reduced dose rate gave rise to a vastly reduced number of configuration errors in the shift register. A dose rate of 6 rad/s yielded just three bad columns compared to greater than 20 bad columns for a dose rate of 60 rad/s. The dose rate expected for the SIT, SET, and the ECAL in CLIC ILD, and the ECAL in ILC ILD is orders of magnitude lower than 6 rad/s and as such the shift register issues would not present a problem even using the current TPAC technology.

Table 4.1: The variations in the noise and pedestals shifts from zero dose after irradiation. Sensors 1, 3, 4, and 6 were unpowered during irradiation; sensors 2, 9, 10, and 12 were powered; sensor 10 had a lower dose rate of 6 rad/s; and sensor 12 had an 18 μm high-resistivity epitaxial layer.

Sensor	Epitaxial Layer		Dose Rate [rad/s]	Parameter	Dose [krad]		
	Thickness [μm]	Type			200	1000	5000
1	12	standard	60	Noise	-	0.055 ± 0.002	-
				Pedestal	-	3.7 ± 0.5	-
3	12	standard	60	Noise	-	0.080 ± 0.002	0.176 ± 0.002
				Pedestal	-	2.8 ± 0.5	3.9 ± 0.5
4	12	standard	60	Noise	0.025 ± 0.002	0.068 ± 0.002	-
				Pedestal	1.7 ± 0.4	2.4 ± 0.4	-
6	12	standard	60	Noise	0.037 ± 0.002	0.083 ± 0.003	0.213 ± 0.003
				Pedestal	0.6 ± 0.5	1.3 ± 0.6	1.8 ± 0.6
2	12	standard	60	Noise	0.040 ± 0.003	-	-
				Pedestal	-14.6 ± 0.6	-	-
9	12	standard	60	Noise	0.088 ± 0.003	-	-
				Pedestal	-16.6 ± 0.5	-	-
10	12	standard	6	Noise	-0.030 ± 0.004	-	-
				Pedestal	-17.9 ± 0.8	-	-
12	18	high resistivity	60	Noise	0.068 ± 0.004	-	-
				Pedestal	-21.6 ± 0.9	-	-

Table 4.2: Summary of the noise and signal results from Section 4.4.1 and Section 4.4.2, and the S/N ratios calculated using Equation 4.4. Sensor 6 was unpowered and received a much larger integrated dose when compared to the other sensors.

Sensor	Sensor State		k_α [mV]	Gain [mV/e$^-$]	Noise [DTU]	Noise [e$^-$]	Noise [mV]	S/N
	Dose [krad]	Annealing [hours]						
6	0	-	194.6 ± 0.1	0.1202 ± 0.0001	5.44 ± 0.02	17.94 ± 0.07	2.16 ± 0.01	90.3 ± 0.4
	5000	168	202.2 ± 0.2	0.1248 ± 0.0001	6.37 ± 0.03	21.03 ± 0.10	2.62 ± 0.01	77.0 ± 0.4
2	0	-	191.8 ± 0.1	0.1184 ± 0.0001	5.63 ± 0.01	18.58 ± 0.04	2.20 ± 0.00	87.2 ± 0.2
	220	282	198.2 ± 0.1	0.1223 ± 0.0001	5.88 ± 0.04	19.42 ± 0.13	2.38 ± 0.02	83.4 ± 0.5
9	0	-	202.6 ± 0.1	0.1250 ± 0.0001	5.53 ± 0.02	18.26 ± 0.07	2.28 ± 0.01	88.7 ± 0.4
	200	250	207.6 ± 0.2	0.1282 ± 0.0001	6.02 ± 0.03	19.87 ± 0.11	2.55 ± 0.01	81.5 ± 0.5
12	0	-	191.8 ± 0.2	0.1184 ± 0.0001	5.50 ± 0.03	18.16 ± 0.11	2.15 ± 0.01	89.2 ± 0.5
	240	144	201.5 ± 0.1	0.1244 ± 0.0001	5.85 ± 0.04	19.30 ± 0.12	2.40 ± 0.01	83.9 ± 0.5

CHAPTER 5

Determination of the top Higgs Yukawa Coupling

5.1 Introduction

The previous chapters have introduced and motivated the ILC and described the technologies which will be used in the ILD with particular focus having been paid on the R&D towards a DECAL. In the remaining chapters of this thesis the physics potential of ILD and the impact of the DECAL will be evaluated using full scale detector simulations.

In this chapter the results of full scale detector simulations to determine the precision with which the ILD detector can measure the top Higgs Yukawa coupling are presented. The work has been completed as a part of the ILD Physics and Analysis Collaboration. The study was completed using centrally generated samples and forms the basis of the semileptonic analysis of the $e^+e^- \rightarrow t\bar{t}H$ interaction for the ILD TDR [23]. The results were combined with the hadronic channel into an LC

Note which can be found here [2].

Section 5.2 explains the motivation behind the analysis, Section 5.3 presents the signal and background processes studied with Section 5.4 describing the methods used to generate the samples. An overview of pile-up removal in the events is given in Section 5.5, the event reconstruction is explained in Section 5.6 and the variables used to separate the signal and backgrounds are described in Section 5.7. Finally results are presented in Section 5.8 using both an optimised cut based analysis and a multivariate technique.

5.2 Motivation

Figure 5.1 demonstrates the expected strength of the Yukawa couplings of the Higgs boson and the expected experimental uncertainties on the measurement after a complete ILC physics programme at 250 GeV, 500 GeV, and 1 TeV [39]. As the top quark is currently the heaviest known particle in the SM, the Yukawa coupling to the Higgs boson is expected to be the strongest. Any deviations from the SM in the couplings would be an indication of new physics. It is thus essential to evaluate the performance of the ILD for measuring the top Higgs Yukawa coupling. The final state of the $t\bar{t}H$ decay consists of eight fermions with at least four jets, potential leptons, and missing energy and this study also demonstrates the ability of the ILD detector to reconstruct complicated topologies.

5.3 Signal and Backgrounds

Figure 5.2(a) and Figure 5.2(b) illustrate the lowest order Feynman diagrams for the process $e^+e^- \rightarrow t\bar{t}H$. For these studies the top quarks were assumed to decay into a W boson and a b-quark 100 % of the time. The W bosons can decay either into two light quarks or a lepton and a neutrino. The $t\bar{t}$ system can therefore decay

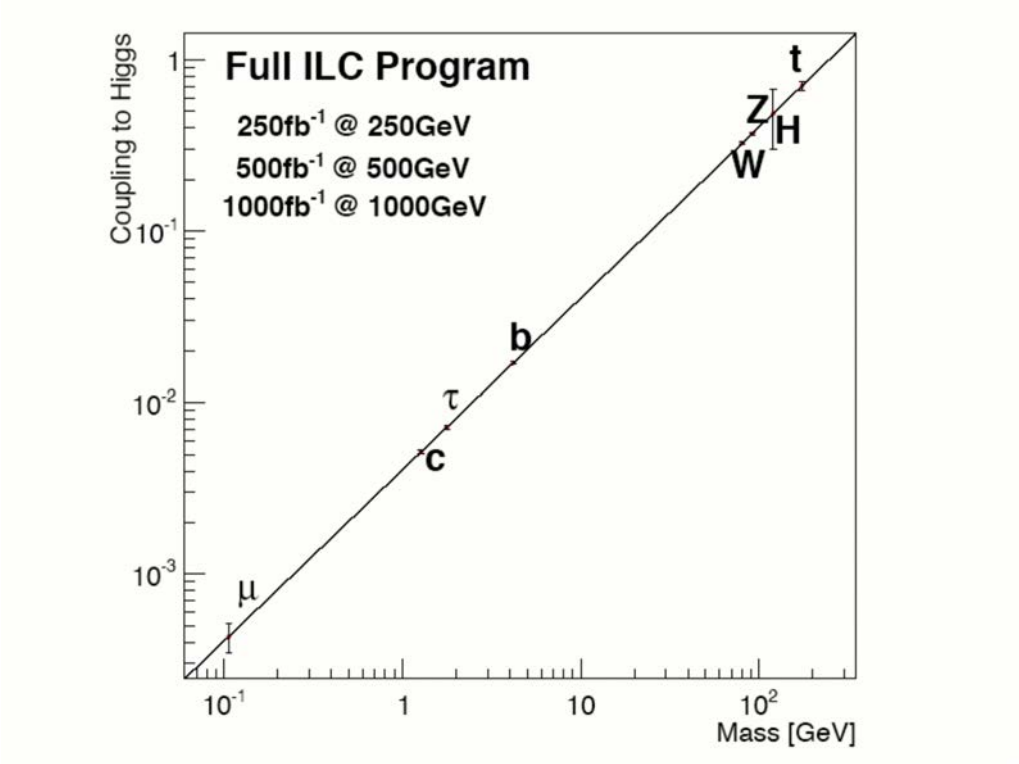

Figure 5.1: Expected experimental precision of the Yukawa couplings of the Higgs boson following a full ILC program running at 250 GeV, 500 GeV, and 1 TeV [39].

into six quarks (hadronic); four quarks, a lepton, and a neutrino (semileptonic), or two quarks, two leptons and two neutrinos (leptonic). There will always be exactly two b-quarks in the final state of the $t\bar{t}$. The semileptonic decays of the $t\bar{t}$ system were studied, with the Higgs decaying via the dominant $b\bar{b}$ decay mode. The final signal in the detector consists of six jets, four of which should be tagged as b-jets, an isolated lepton, and missing energy and momentum from a neutrino.

Irreducible backgrounds to this process arise from the eight fermion final states of $t\bar{t}Z$ where the Z decays into a $b\bar{b}$ pair and $t\bar{t}b\bar{b}$ where the $t\bar{t}$ system radiates a gluon which forms a $b\bar{b}$ pair. A large background contribution arises from $t\bar{t}$ due to the huge cross-section relative to the signal. There is also a contribution from the other decay modes of the $t\bar{t}H$ system where the Higgs boson does not decay to a $b\bar{b}$ pair and the fully leptonic and hadronic decays of the top quarks.

The cross-sections of these processes for unpolarised beams as a function of centre of

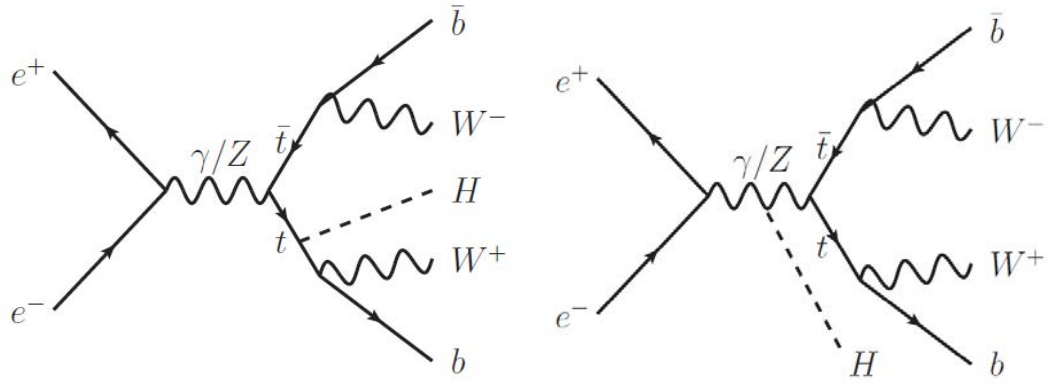

(a) $e^+e^- \rightarrow t\bar{t}H$ (b) $e^+e^- \rightarrow t\bar{t}H$ (Higgs-strahlung)

Figure 5.2: The lowest order Feynman diagrams for the process $e^+e^- \rightarrow t\bar{t}H$ with a $t\bar{t}$ pair radiating a Higgs from one of the top quarks (5.2(a)), and the Higgs-strahlung process where the Higgs is radiated from a Z boson which the decays to a $t\bar{t}$ pair (5.2(b)) [40].

mass energy are shown in Figure 5.3. Although the cross-section for $t\bar{t}H$ production peaks at centre of mass energies between 700 GeV and 800 GeV the study has been conducted at 1 TeV for consistency with other physics analyses performed at the ILC such as the WW fusion production process of a Higgs boson where the cross-section increases with energy.

The conversion between the precision on the measurement of the cross-section into the precision on the top Yukawa coupling is given by

$$\frac{\Delta y_t}{y_t} = \left(\frac{\sigma/y_t}{|d\sigma/dy_t|} \right)_{y_t = y_t(SM)} \frac{\Delta\sigma}{\sigma} \quad . \tag{5.1}$$

Previous studies at lower energies [40] [41] [92] have neglected the contribution to the final state from Higgs-strahlung, with $Z \rightarrow t\bar{t}$, due to the tiny cross-section relative to the production of a top pair with a radiated Higgs. Therefore, the prefactor on the right hand side of Equation 5.1 was assumed to be exactly 0.5. At 1 TeV, this assumption no longer holds as the Higgs-stralung process contributes approximately 4% [2] of the $t\bar{t}H$ events, modifying the prefactor to 0.52. The precision on the cross-section is related to the significance with which the signal can be measured and the top Yukawa coupling is the therefore given by

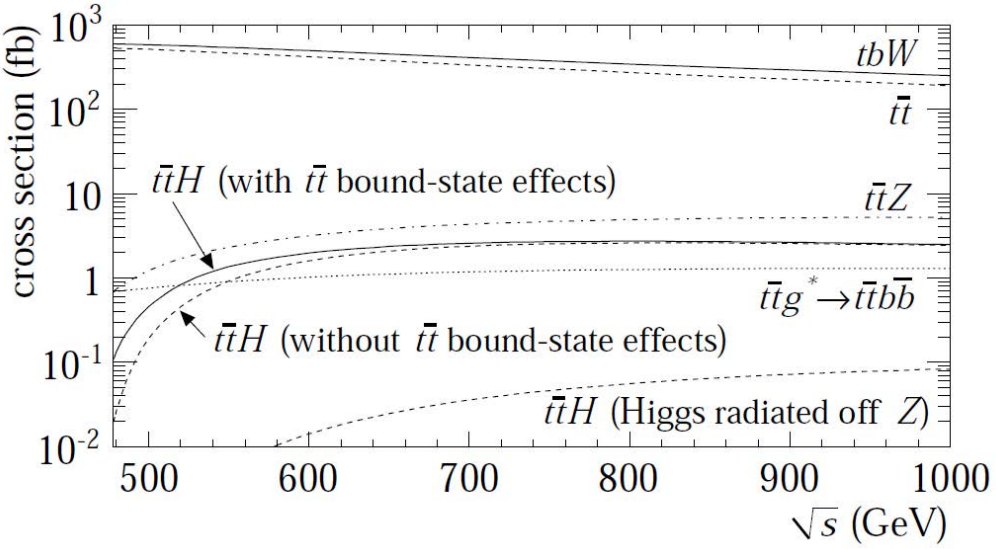

Figure 5.3: Summary of cross-sections for signal and background processes for unpolarized initial beams with initial state radiation and beamsthrahlung effects included [40].

$$\frac{\Delta y_t}{y_t} = \frac{0.52\sqrt{S+B}}{S} \quad , \tag{5.2}$$

where S and B are the numbers of signal and background events selected in the final sample.

5.4 Sample Generation

The samples for this study were generated using two event generators, Whizard-1.95 [93], and Physsim [94]. The $t\bar{t}$ samples were generated using Whizard-1.95 whereas the $t\bar{t}H$, $t\bar{t}b\bar{b}$, and $t\bar{t}Z$ samples used Physsim due to the capability of including "Non Relativistic QCD" effects and an improved phase space integration time for the eight fermion final states compared to Whizard. The $t\bar{t}$ samples generated with Whizard contain all six fermion final states which are consistent with a $t\bar{t}$ system but is dominated by the $t\bar{t}$ process. For the purpose of this study the six fermion final states are refered to as $t\bar{t}$. The samples were generated assuming M_H=125 GeV and M_t=173 GeV.

Table 5.1: The cross-sections for all processes used in this analysis for different polarisation states assuming a Higgs boson mass of 125 GeV and a top quark mass of 173 GeV. The $t\bar{t}H$ →other entry here contains all decays of the system which are not the signal including fully leptonic and hadronic modes and non $b\bar{b}$ decays of the Higgs boson.

Process	$\sigma(e^-,e^+)$ [fb]		
	(-1.0, +1.0)	(-0.8, +0.2)	(+0.8, -0.2)
$t\bar{t}H$ semileptonic	1.4956	0.8345	0.4229
$t\bar{t}H$ →other	4.3474	2.4559	1.2446
$t\bar{t}Z$	14.020	7.7458	2.9191
$t\bar{t}b\bar{b}$	3.4293	1.9125	0.9566
$t\bar{t}$	808.31	448.91	168.88

The Data Summary Tables (DST) used in this analysis were centrally produced at DESY. The simulations used software consistent with iLCSoft v01-14-01-p00, namely Geant4.5.p01 and Mokka v08-00-03. The geometry model ILD_o1_v5 was used. This model consists of a SiW ECAL with 5×5 mm^2 cell sizes, and a Steel-Scintillator HCAL with 3×3 cm^2 readout pads. The model had also been checked for consistency with the required material budgets and any unexpected overlaps had been removed. The reconstruction was performed using packages consistent with the production release of iLCSoft v01-16 including; MarlinTrk, a new Kalman-filter based track finder; PandoraPFA, and LCFIPlus to reconstruct primary and secondary vertices and perform jet clustering and flavour tagging. The information contained within the DST included the vertex information, Monte Carlo particles, calorimeter cluster information, and PandoraPFO collections.

The samples were reweighted to achieve polarisation states of $(e^-, e^+) = (\pm 0.8, \mp 0.2)$. Samples corresponding to 500 fb^{-1} for each polarisation were used and the results combined. The corresponding cross-sections for these polarisations are given in Table 5.1 alongside the values for fully polarised beams.

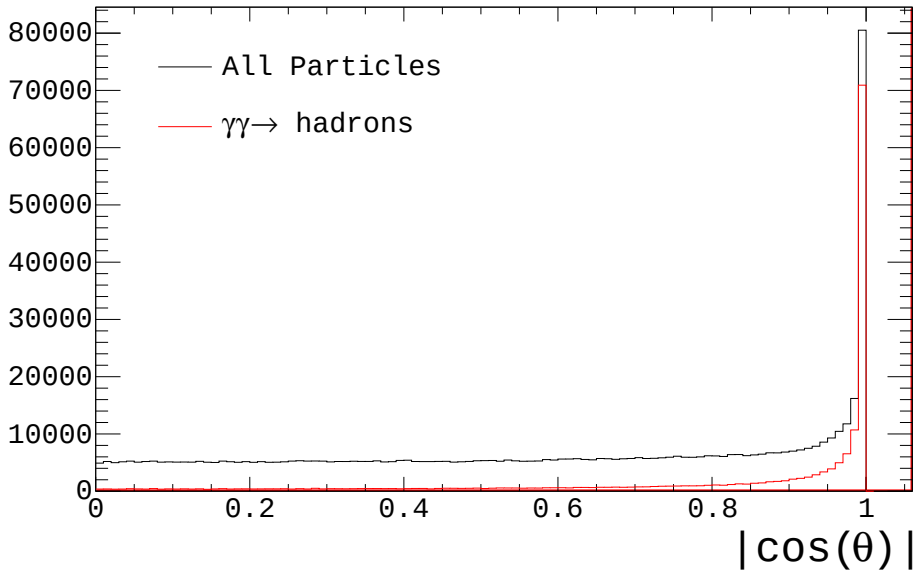

Figure 5.4: The simulated polar angle of all MCParticles in $e^+e^- \rightarrow t\bar{t}H$ events at 1 TeV (black), and the $\gamma\gamma \rightarrow$hadrons pile-up only (red).

5.5 Removal of $\gamma\gamma \rightarrow$hadrons Overlay

In addition to the primary process, there is an extra component from unrelated $\gamma\gamma \rightarrow$hadrons "pile-up". On average there are 4.1 pile-up events per bunch-crossing at $\sqrt{s}$=1 TeV, leading to an additional 50 GeV of energy in the reconstructed event. The particles in the pile-up events are generally low p_T and are concentrated at angles close to the beam axis as shown in Figure 5.4.

Figure 5.5 shows that without the removal of the pile-up the reconstructed energy in the event is overestimated. This is due to the Durham algorithm [95] forcing all of the particles in an event into jets. In order to use the Durham algorithm implemented within LCFIPlus these pile-up events needed to be removed.

As the pile-up events are separate from the primary process it should be possible to remove them and three methods were tested to achieve this. Firstly, due to the angular dependence, all PandoraPFOs with a polar angle smaller than a certain value were removed. The second method builds on the first approach. The events were forced into eight Durham jets, six of these were associated with the event and

Table 5.2: Summary of selected $\gamma\gamma$ →hadrons removal methods including the optimal PandoraPFOs and Durham eight jet methods cut at $|\cos(\theta)|$ <0.98, and various values of R for the kt six jet method.

Method	prob	ϵ	ρ	$\sqrt{\epsilon\rho}$
$\lvert\cos(\theta)\rvert < 0.98$	0.24	0.963	0.894	0.928
Durham $\lvert\cos(\theta)\rvert < 0.98$	0.07	0.904	0.922	0.913
kt R=1.0	0.20	0.894	0.925	0.910
kt R=1.1	0.30	0.912	0.920	0.916
kt R=1.2	0.96	0.927	0.915	0.921
kt R=1.3	0.75	0.939	0.911	0.925
kt R=1.4	0.65	0.949	0.907	0.928
kt R=1.5	0.18	0.957	0.903	0.929

the remaining two were "beam jets" which were removed on the basis of their angles relative to the beams. Finally, the events were forced into six jets using the kt algorithm [96] with an optimised value of R. The kt algorithm is different to the Durham algorithm primarily in the fact that it does not force all of the particles into the jets, only those within a certain jet radius.

Table 5.2 gives a summary of selected cuts. The probability for each was calculated using a χ^2 comparison between the total amount of visible energy passing each cut and the total visible energy in events without pile-up. Also shown in Table 5.2 are the efficiency of genuine event PandoraPFOs not being removed, ϵ, and the purity of the removed PandoraPFOs being from the pile-up component of the event, ρ. The optimal method to remove the pile-up and recovering the correct amount of visible energy was using the kt algorithm with R=1.2 (see Figure 5.5). This result is consistent with other analyses completed for the ILD TDR and studies conducted for CLIC such as [97].

The results presented in the remainder of this chapter have the $\gamma\gamma$ →hadrons pile-up removed even if it is not stated. The only exception is the lepton isolation which was always performed first followed by the pile-up removal to ensure that the isolated leptons were not discarded with the pile-up.

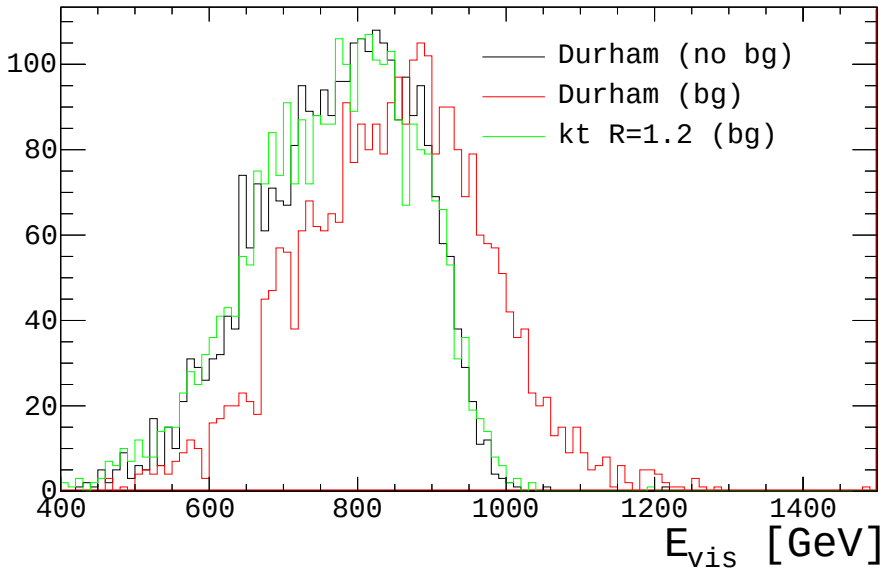

Figure 5.5: The total visible energy for $e^+e^- \rightarrow t\bar{t}H$ events at 1 TeV with and without $\gamma\gamma \rightarrow$ hadrons clustered using the Durham algorithm, and the kt algorithm for the semileptonic mode.

5.6 Event Reconstruction

The reconstructed particles in an event are grouped together into a "collection" of PandoraPFOs. Initially, the collection of PandoraPFOs was examined for isolated lepton which were then removed from the list. The $\gamma\gamma \rightarrow$hadron background was then removed (as explained in Section 5.5) using the kt algorithm operating in exclusive mode to form six jets with R=1.2 as implemented by the FastJet [98] wrapper within Marlin. Any PandoraPFO not associated with these six jets were then also removed from the collection. The remaining PandoraPFOs were then passed to LCFIPlus where they were forced into six jets using the Durham algorithm. The Durham jets were then flavour tagged using LCFIPlus.

Due to the large number of jets in the final state there are ambiguities in the way these should be combined to reconstruct the two W bosons, two top quarks and the Higgs boson. The optimal combination was found by minimising

$$\chi^2 = \frac{(M_{bl\nu} - M_t)^2}{\sigma^2_{bl\nu}} + \frac{(M_{bjj} - M_t)^2}{\sigma^2_{bjj}} + \frac{(M_{b\bar{b}} - M_H)^2}{\sigma^2_{b\bar{b}}} \ , \tag{5.3}$$

where the top quarks are formed by combining a b-jet with a W boson, and the Higgs boson from the remaining two b-jets. The first W boson is formed using the two least b-like jets[1] with the other formed from the isolated lepton and reconstructed neutrino.

The values of $\sigma_{bl\nu}$, σ_{bjj}, and $\sigma_{b\bar{b}}$ were calculated by matching the PandoraPFOs within the reconstructed jets with the truth particles and forming truth jets for the optimal combination of jets with initial values of $\sigma_{bl\nu}$=σ_{bjj}=$\sigma_{\mathrm{b\bar{b}}}$=1. Distributions were created for the difference between reconstructed jet energies and the truth jet energies and the widths of these gave values of $\sigma_{bl\nu}$=17.0, σ_{bjj}=11.5, and $\sigma_{\mathrm{b\bar{b}}}$=8.0. The leptonically decaying top quark had a smaller weight in the final reconstruction due to the uncertainties associated with the neutrino.

5.6.1 Isolated Lepton Finder

To reconstruct the leptonically decaying top quark, the PandoraPFOs were searched for leptons in a region of the detector with minimal amounts of other activity, a so-called "isolated lepton". It was essential to have a highly efficient and pure method of identifying the isolated leptons. For the analysis a cut was applied demanding exactly one isolated lepton per event. If no isolated leptons were found then it was impossible to reconstruct the top quark, and if too many were found it had a negative impact on the jet clustering algorithms. Taking these factors into account the LAL Lepton Finder isolation method as presented here [99] was used. The PandoraPFOs in the events were forced into eight jets and the isolation of the constituent particles within the jets checked using

[1]defined as the jets with the lowest probability of originating from a b-quark according to LCFIPlus.

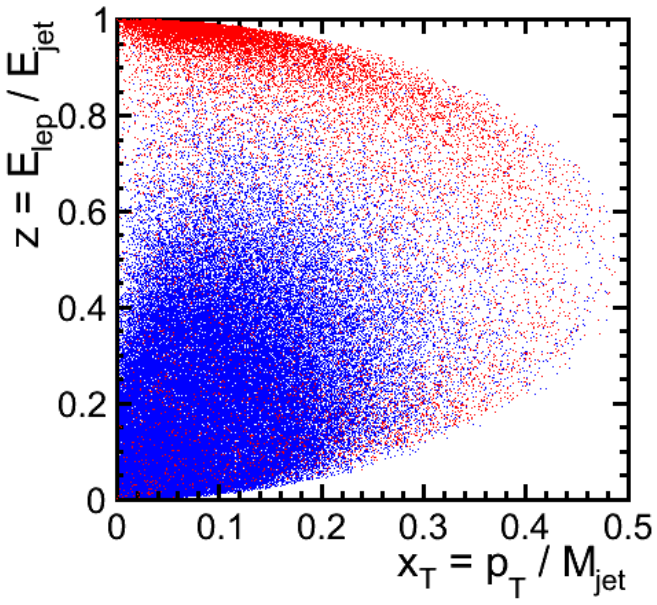

Figure 5.6: A scatter plot showing the variables used in the lepton isolation for leptons originating from a W boson (red) and all other leptons (blue) [2].

$$z = \frac{E_{lep}}{E_{jet}} \ , \tag{5.4}$$

where E_{lep} and E_{jet} are the energies of the lepton and the jet within which the lepton resides, and

$$x_T = \frac{p_T}{M_{jet}} \ , \tag{5.5}$$

where p_T is the transverse momentum of the lepton and M_{jet} is the mass of the jet. The values of z and x_T were optimised to yield the best performance at values of x_T <0.25, and z>0.6 as shown in Figure 5.6. Table 5.3 shows the efficiency of this method for locating isolated leptons, coupled with the purity of the selection and the source of the isolated leptons. An efficiency of 82% (89%) and purity of 95% (97%) for electrons (muons) from W decays is observed.

Table 5.3: The performance of the isolated lepton finder including the efficiency of selecting a genuine lepton from a W decay, and the composition of the selected samples including fake leptons [2].

Lepton	Efficiency	Composition			
		W→e, μ	W→ τ →e, μ	Other e, μ	Fake e, μ
Electrons	84.0%	94.2%	2.9%	1.6%	2.3%
Muons	90.5%	96.3%	2.4%	1.2%	0.7%

5.6.2 Neutrino Reconstruction

The neutrino was reconstructed assuming all of the missing momenta in the event is associated with a neutrino with zero mass. Thus, the properties of the neutrino are given by

$$P^{\nu} = -\sum_{PFO=1}^{n} P^{PFO} \ , \tag{5.6}$$

$$E^{\nu} = |P^{\nu}| \ . \tag{5.7}$$

Figure 5.7 demonstrates the neutrino reconstruction resolutions achieved using the above equations and comparing to the truth information. In general the neutrino is reconstructed very well due to the well defined initial state. However, it is possible for photons to be radiated off the e^+e^- beams prior to the interaction. This leads to Initial State Radiation (ISR) which modifies the beam collision properties causing both a change in the centre of mass energy, and an initial state with non zero momenta in the laboratory frame. These scenarios can have an impact on the neutrino reconstruction using this method.

The maximum energy of the ISR in these events to remain above production threshold for the reaction to occur is ∼530 GeV. From Figure 5.8 it can be seen that the majority of events contain small amounts of ISR compared to this value (see Figure 5.8(a)) but some events do have significantly reduced centre of mass energies. In

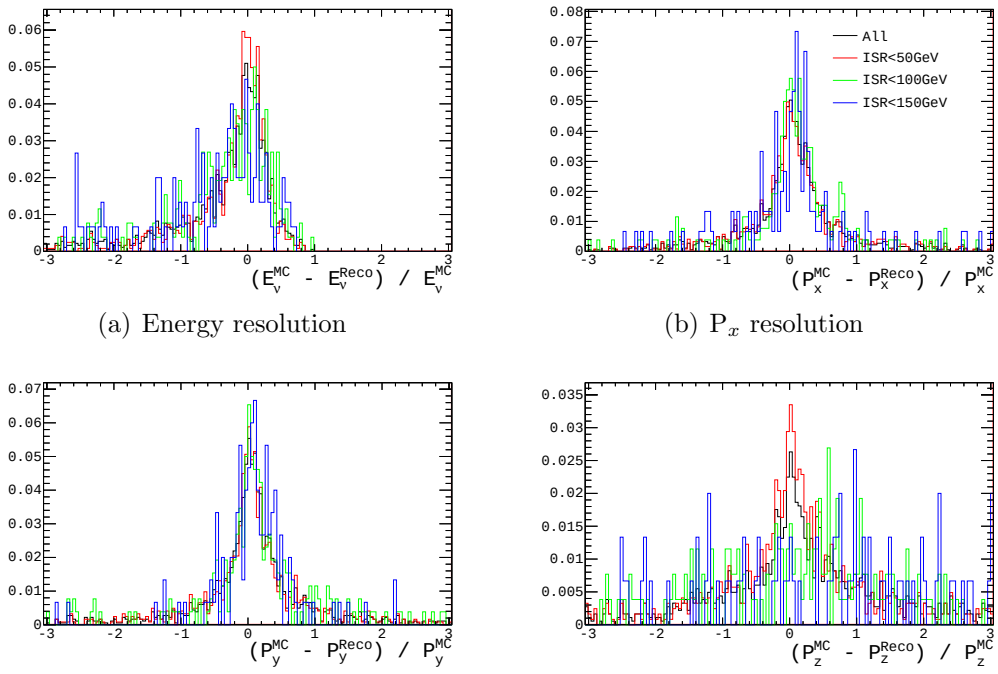

(a) Energy resolution

(b) P_x resolution

(c) P_y resolution

(d) P_z resolution

Figure 5.7: The reconstructed neutrino energy and momenta resolutions for varying amounts of ISR.

general the ISR photons are radiated at small angles relative to the beams and can have large momentum in the beam direction and very little transverse momentum. This is reflected in the reconstructed momentum resolutions in Figure 5.7 where the z-momentum suffers as the amount of ISR increases whereas the x and y components are unaffected.

An extra contribution to the neutrino resolution comes from the $\gamma\gamma \rightarrow$hadrons pile-up removal. If too many PandoraPFOs from the genuine event are removed or too many associated with the pile-up event remain then the collision energy and initial momenta of the system will be misunderstood. This is a small factor compared to the ISR due to the performance of the pile-up removal. In the main analysis, cuts are applied to minimise the impact of a poorly reconstructed neutrino .

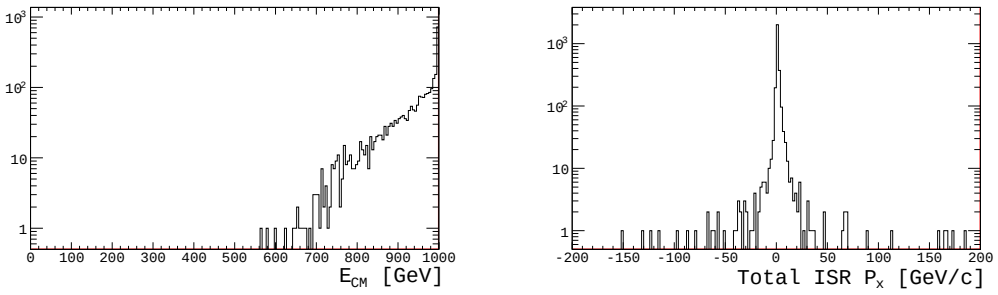

(a) Centre of mass energy

(b) Total ISR P_x

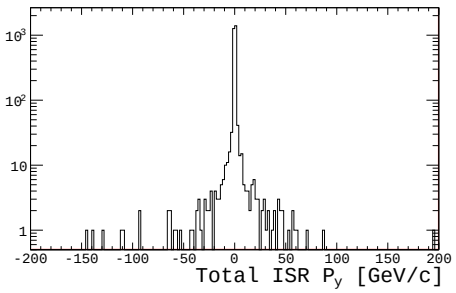

(c) Total ISR P_y

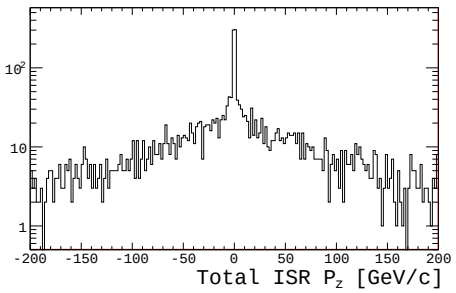

(d) Total ISR P_z

Figure 5.8: Monte Carlo information for the actual centre of mass energy of the collision (top left) and the scalar sum of the momenta for all the ISR photons in an event.

5.7 Selection Variables

The signal was selected and the background suppressed by cutting on various kinematic variables of the event including:

- the number of isolated leptons in the event,
- the total visible energy of the event,
- the number of reconstructed PandoraPFOs,
- the thrust of the event,
- the Y_{45} and Y_{56} parameters from the Durham jet finding algorithm,
- the b-tag information, and
- the reconstructed masses of the best combination of fermions.

The normalised distributions of these variables are shown in Figures 5.9–5.11 and further information for each of these is given below.

5.7.1 Total Visible Energy

Events were selected within a window of the total visible energy in an event, E_{vis}^{tot}, in order to remove events with a large amount of ISR or events which contained multiple neutrinos in the final state. Figure 5.9(b) shows that the total visible energy in the fully hadronic states peaks at larger values than the signal. Therefore, a window cut gave large background suppression whilst maintaining high statistics for the signal.

5.7.2 Number of Particle Flow Objects

Events with a small number of PandoraPFOs were rejected to further remove backgrounds with multiple neutrinos, especially those containing two leptons, two neutrinos, and just two or four quarks. This is of particular relevance for the $t\bar{t}$ background, which contains two-lepton processes with high cross-sections in the final state (see Figure 5.9(c)). The number of PandoraPFOs in the fully hadronic states is much larger than in the signal due to the larger number of jets.

5.7.3 Thrust

The thrust of an event is given by

$$T = \max \frac{\sum_i |\hat{n} \cdot \vec{p_i}|}{\sum_i |\vec{p_i}|} \ , \tag{5.8}$$

where p_i is the momentum of the jet. The thrust of an event with two back to back jets is one whereas for an event where the jets are spherically symmetric in the

detector is 0.5. The $t\bar{t}$ system is effectively a two fermion system and Figure 5.9(d) shows that the thrust of the event is much larger than the $t\bar{t}H$, $t\bar{t}Z$, and $t\bar{t}b\bar{b}$ processes. Therefore, the thrust is an effective discriminant to reduce the huge $t\bar{t}$ backgrounds.

5.7.4 Jet Clustering

The signal and backgrounds were clustered using the Durham algorithm into 6 jets in the final state. The distance parameter between n and (n+1) jets in the final state is given by

$$Y_{ij} = \frac{\min(E_i^2, E_j^2)(1 - \cos\theta_{ij})}{E_{CM}^2} \ , \tag{5.9}$$

where i=n, j=(n+1) jets, and $\cos\theta_{ij}$ is the angle between the jets. For $t\bar{t}$ events with an isolated lepton there is a maximum of four quarks in the event. When these events are forced into a six jet configuration (to be consistent with the signal) the values of Y_{45} and Y_{56} will be small as the distance between the jets will be smaller than in the eight fermion final states. This is demonstrated in Figure 5.9(e) and Figure 5.9(f) where the $t\bar{t}$ and leptonic $t\bar{t}H$ distributions have different shapes to the other processes.

5.7.5 Flavour Tags

The signal has four b-jets in the final state, two from the top decays and two from the Higgs decay. The $t\bar{t}$ background will only contain two b-jets from the top decays as will ∼80 % of $t\bar{t}Z$ events. The flavour tagging is thus a very good discriminant between the signal and backgrounds. The b-tag probability values from LCFIPlus were ordered from largest (b-tag$_1$) to smallest (b-tag$_n$ for an event clustered into n jets) and cuts were made on the four largest values to remove the events containing

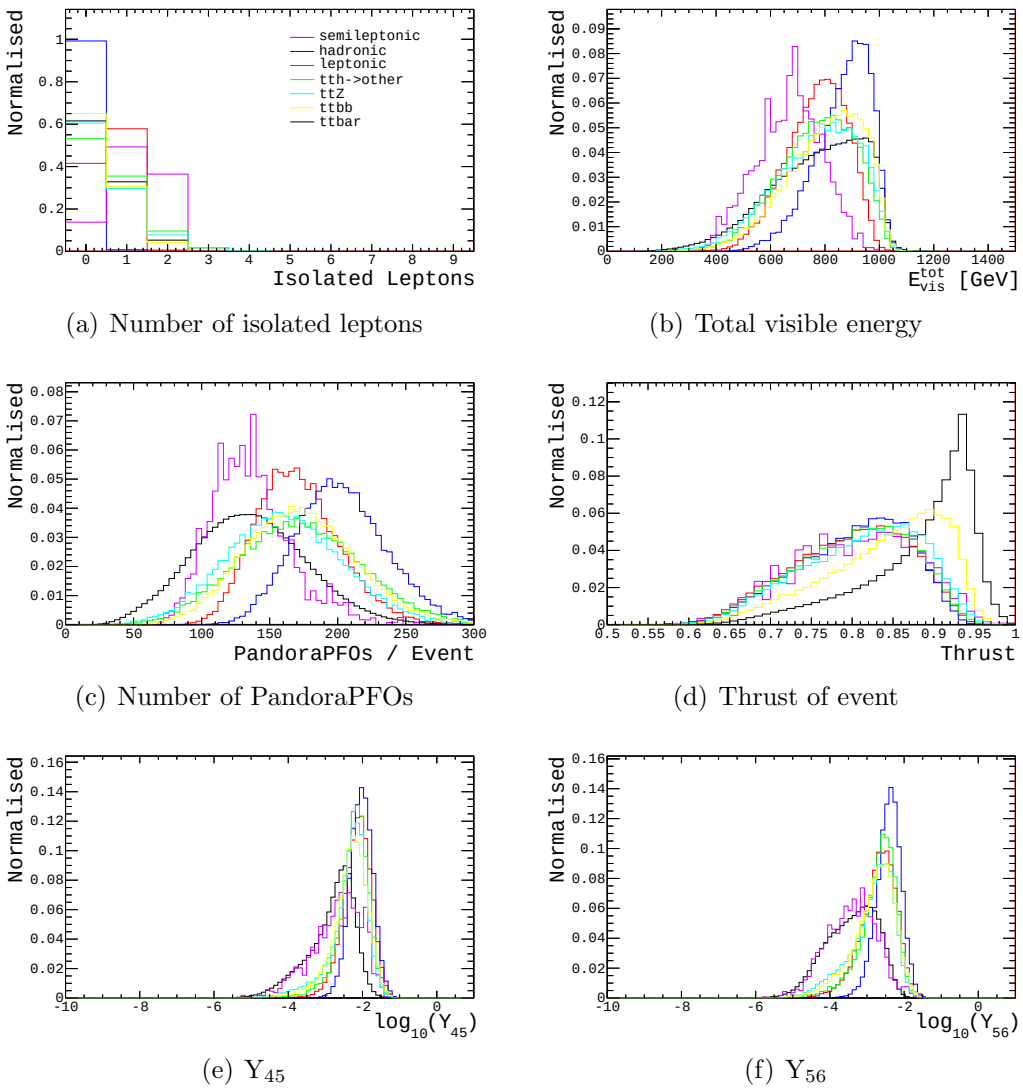

(a) Number of isolated leptons

(b) Total visible energy

(c) Number of PandoraPFOs

(d) Thrust of event

(e) Y_{45}

(f) Y_{56}

Figure 5.9: Normalised histograms of the number of isolated leptons (5.9(a)), total visible energy (5.9(b)), number of PandoraPFOs (5.9(c)), thrust (5.9(d)), and the jet parameters Y_{45} and Y_{56} (5.9(e) and 5.9(f)) within the events for the semileptonic decay mode (red) and reweighted backgrounds.

just two b-jets.

Figure 5.10 shows the differences in the expected profiles of the b-tags. The two largest b-tags in all of the samples have very similar profiles as LCFIPlus is accurately identifying the b-jets in the events. For the backgrounds, there are small peaks at higher values of the b-tag$_3$ and b-tag$_4$ distributions due to the small contributions from genuine backgrounds with four b-jets, but the shapes are dominated

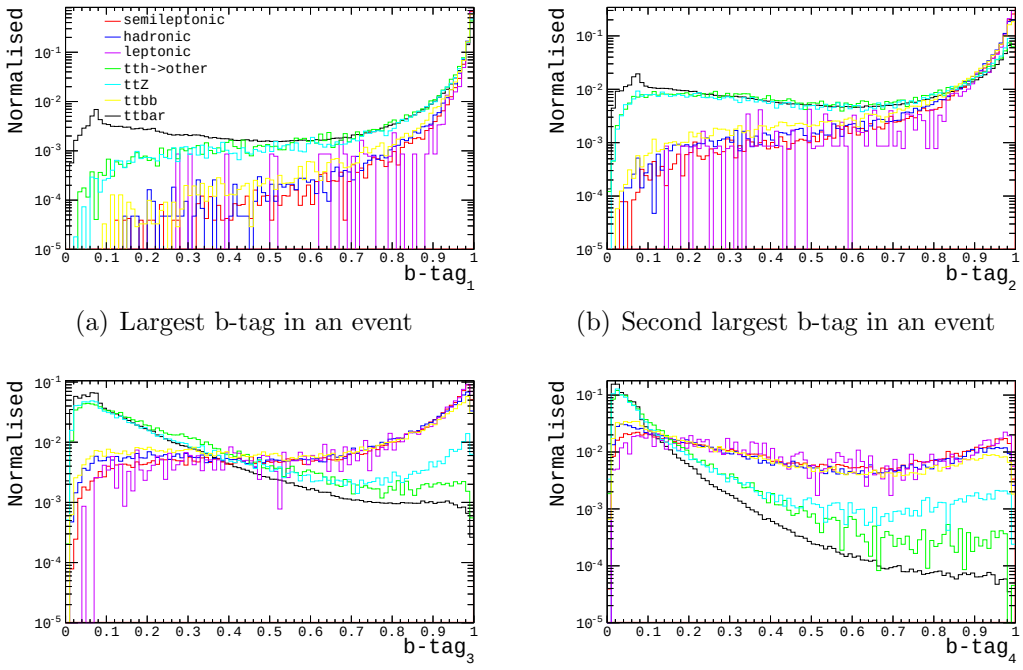

(a) Largest b-tag in an event

(b) Second largest b-tag in an event

(c) Third largest b-tag in an event

(d) Fourth largest b-tag in an event

Figure 5.10: Normalised histograms for the response of the b-tagging from LCFIPlus

by the peaks around 0.1, especially in the $t\bar{t}$ events. The peak at large values for genuine b-jets in b-tag$_4$ is reduced due to the complex nature of searching for four b-jets but the peak is still more pronounced in the signal than the backgrounds.

5.7.6 Reconstructed Masses

After finding the optimal combination of jets from Equation 5.3 and reconstructing the event, cuts were made on the resulting masses of the top quarks, Higgs boson and total mass to ensure that the final event is consistent with $t\bar{t}H$. Figure 5.11 shows the reconstructed masses for the leptonic W, leptonic top, hadronic W, hadronic top, Higgs, and total mass of the final state for the signal and the background for all events where exactly one isolated lepton was identified. This requirement was essential for the reconstruction of the leptonically decaying top quark in the semileptonic mode.

The statistics in the hadronic samples of Figure 5.11 are poor due to the excellent rejection of events which do not contain any isolated leptons. This is also reflected by the lack of a peak in the reconstructed mass of the leptonic W boson for the hadronic sample as there are no genuine isolated leptons for the reconstruction. A peak is observed in all of the backgrounds due to the finite fraction of expected leptonic top decays in the samples. There is a large fraction of events within the $t\bar{t}$ background which do not reconstruct a good hadronic W boson due to the low multiplicity in the events containing multiple neutrinos.

5.8 Results

The analysis was completed using two complimentary approaches; a cut based method where cuts were applied sequentially to the samples, and a multivariate analysis using the TMVA toolkit [100]. The cut based approach was used as a proof of principle to show that the signal could be successfully separated from the huge number of background events and the multivariate analysis allowed a more complex study to be completed. The cut based approach also serves as a sanity check of the work completed in Chapter 6 (where the author generated the samples).

5.8.1 Cut Based Analysis

The cuts on the variables described in Section 5.7 were applied to the data sets to select the signal and reject the background events. The cuts were optimised to maximise the significance $\mathcal{S} = \frac{S}{\sqrt{S+B}}$ of selecting the signal, where S and B are the number of signal and background events passing the cut. Each cut was applied and optimised on the subset of events which passed all of the previous cuts.

Figure 5.12 and Table 5.4 show the optimised cut values and the number of expected signal and background events passed each cut for 1000 fb^{-1} at $\sqrt{s}$=1 TeV. The $t\bar{t}H$ events where the Higgs does not decay to a $b\bar{b}$ pair are incorporated into the

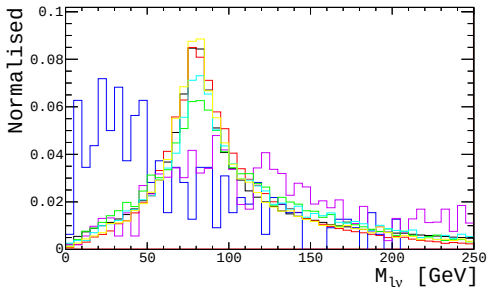

(a) Reconstructed mass of leptonic W boson

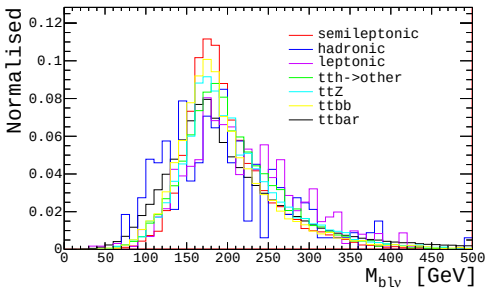

(b) Reconstructed mass of leptonic top quark

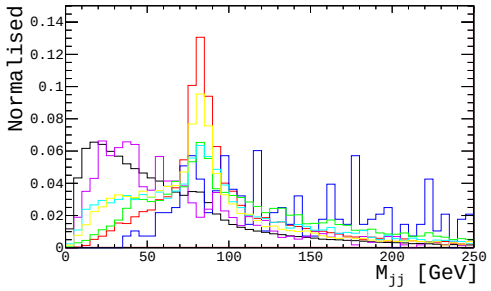

(c) Reconstructed mass of hadronic W boson

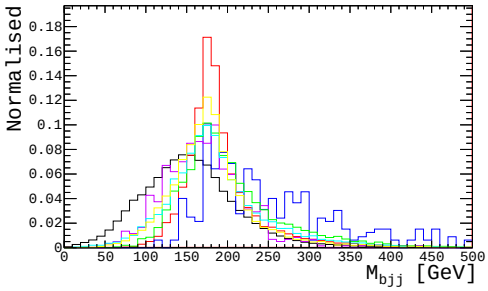

(d) Reconstructed mass of hadronic top quark

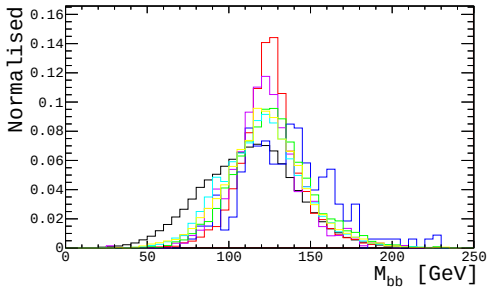

(e) Reconstructed mass of Higgs boson

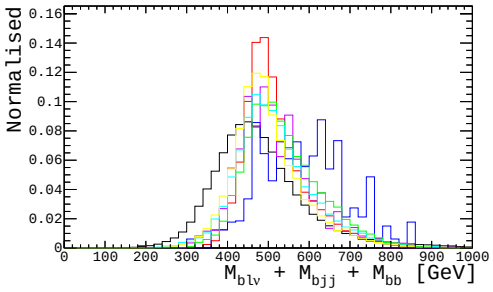

(f) Total reconstructed mass of the events

Figure 5.11: The reconstructed masses of the leptonic W boson, leptonic top quark, hadronic W boson, hadronic top quarks and Higgs boson candidates for the combination of jets which minimises Equation 5.3 when there is exactly one isolated lepton in the event.

$t\bar{t}H \rightarrow$other events. Whilst the cuts before the b-tags demonstrate excellent background reduction, the main discriminant in this analysis is the b-tag$_3$ cut as this yields the largest increases in the signal significance. The small increases observed when applying the mass cuts are a result of the excellent background suppression from the previous cuts leading to only events which are consistent with $t\bar{t}H$ having their masses reconstructed.

Cut	leptonic	semileptonic	hadronic	$t\bar{t}H \rightarrow$other	$t\bar{t}Z$	$t\bar{t}b\bar{b}$	$t\bar{t}$	$\frac{S}{\sqrt{S+B}}$
Total Events	151.4	628.7	652.7	1046.1	5332.4	1434.5	308800.9	1.11
N_{isolep}=1	74.6	363.5	5.0	371.8	1581.5	439.9	101295.2	1.13
610< E_{vis} <1000	49.6	338.5	4.7	312.7	1228.9	373.8	75507.1	1.21
nPFOs>154	15.0	235.0	4.1	195.0	589.0	194.5	12605.9	2.00
Thrust<0.88	12.5	205.6	3.7	168.9	492.6	140.0	6092.3	2.44
$\log_{10}(Y_{45})$ >-2.25	7.7	151.3	3.2	108.5	295.2	91.0	2067.2	2.90
$\log_{10}(Y_{56})$ >-3.35	6.9	145.1	3.2	106.2	277.6	86.0	1836.1	2.92
b-tag$_1$ >0.96	6.7	135.1	2.8	79.8	216.9	78.3	1367.8	3.11
b-tag$_2$ >0.91	6.1	118.2	2.3	41.2	135.1	66.9	715.2	3.59
b-tag$_3$ >0.67	5.5	102.1	1.6	5.7	59.4	56.0	137.2	5.33
b-tag$_4$ >0.04	5.5	100.5	1.5	5.4	58.3	54.8	128.7	5.34
χ^2 <450	5.3	100.0	1.4	5.2	56.8	53.7	126.0	5.36
364< M_{Total} <808	5.2	99.7	1.4	5.2	56.5	53.5	124.7	5.36
0< M_W^{lep} <360	5.1	99.5	1.4	5.2	56.5	53.3	122.5	5.37
84< M_t^{lep} <442	5.1	99.5	1.4	5.2	56.5	53.2	121.9	5.37
28< M_W^{had} <392	5.1	99.4	1.4	5.1	56.5	53.1	121.3	5.38
96< M_t^{had} <420	5.1	99.4	1.4	5.1	56.5	53.0	121.0	5.38
98< M_H <234	4.4	94.8	1.2	4.6	46.1	48.2	106.7	5.42

Table 5.4: The expected number of events passing each cut when the cut values are optimised to select the semileptonic signal with maximum significance at $\sqrt{s}$=1 TeV for an integrated luminosity of 1000 fb^{-1} divided equally between both polarisation states. The $t\bar{t}H \rightarrow$other is the background where the Higgs boson does not decay to a $b\bar{b}$ pair.

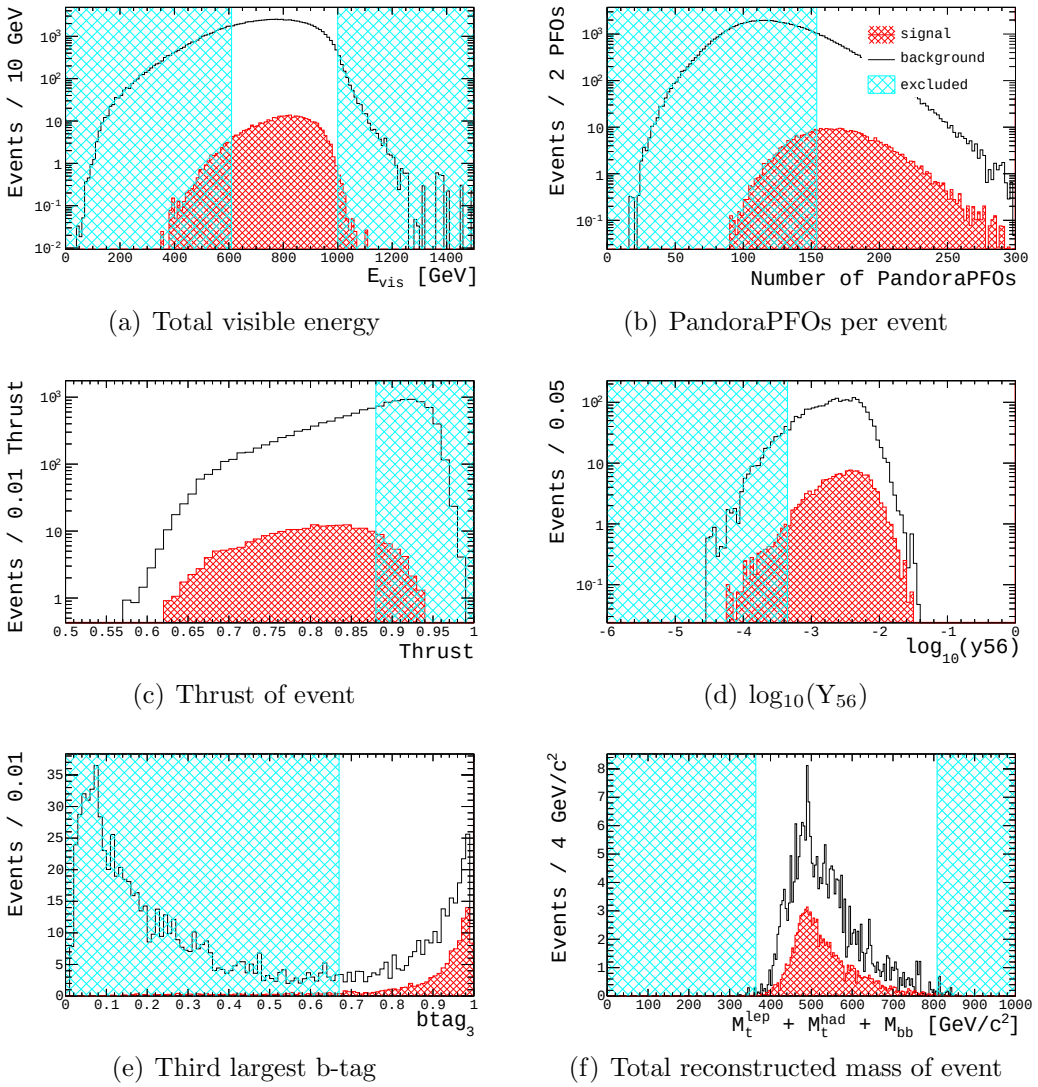

(a) Total visible energy

(b) PandoraPFOs per event

(c) Thrust of event

(d) $\log_{10}(Y_{56})$

(e) Third largest b-tag

(f) Total reconstructed mass of event

Figure 5.12: The distributions of observables used in the event selection where the cuts are applied sequentially from top left to bottom right to the subset of event which passed all previous cuts. The signal is shown in red and the total reweighted background in black. The cyan box shows the region where the events which will be rejected from the next cut reside.

Figure 5.13 demonstrates the power of the background suppression. Before any cuts have been applied the reconstructed Higgs mass peak in the signal is completely swamped by background events. After all of the cuts have been applied the number of signal and background events remaining are comparable with each other and the Higgs boson mass peak is clearly visibly above the background. The final efficiency of signal selection, ϵ_{sig}, is 15.1% with a selected sample purity, $\rho^{\text{sel}}_{\text{sample}}$, of 31.0%.

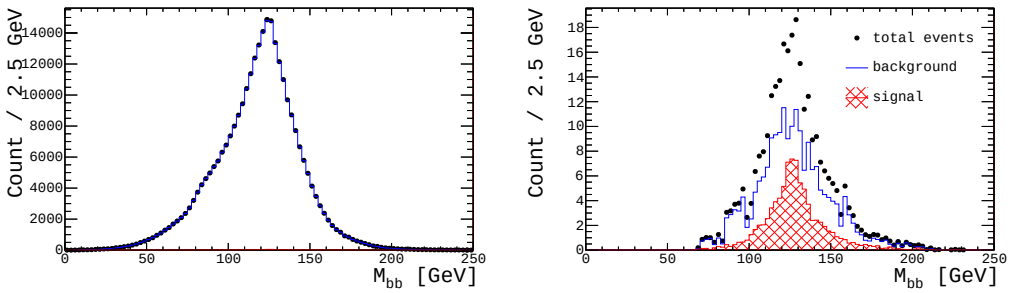

Figure 5.13: The reconstructed Higgs boson mass for the optimal combination of jets in the semileptonic decay mode for all events (left) and only the events which pass all of the cuts (right).

This yields a signal significance of 5.4 and a statistical uncertainty of 9.6% on the value of $g_{t\bar{t}H}$.

5.8.2 TMVA Analysis

A multivariate analysis using the TMVA toolkit was implemented using Boosted Decision Trees with gradient boosting (BDTG) in order to improve the signal and background separation.

The variables defined in Section 5.7 with the addition of the helicity angle of the decay products of the Higgs boson were used as the input. The helicity angle is defined as the angle of the Higgs boson decay products, in the rest frame of the Higgs boson, with respect to the direction of the Higgs boson's momentum. As the SM Higgs boson is a scalar particle the decay products should be distributed isotropically and back-to-back in the Higgs boson rest frame. The Z boson, however, is a vector particle and the decay products are not isotropic. Figure 5.14 demonstrates the power of this cut, with the $t\bar{t}Z$, $t\bar{t}b\bar{b}$ and $t\bar{t}$ backgrounds having an excess of events at large values of $|\cos(\theta_{hel})|$ compared to the $t\bar{t}H$ decays.

The samples were split into two subsets of events. Half of the events were used to train the TMVA with the remaining events used for testing. Figure 5.15 shows the efficiencies, purities, and signal significances for various values of the BDTG

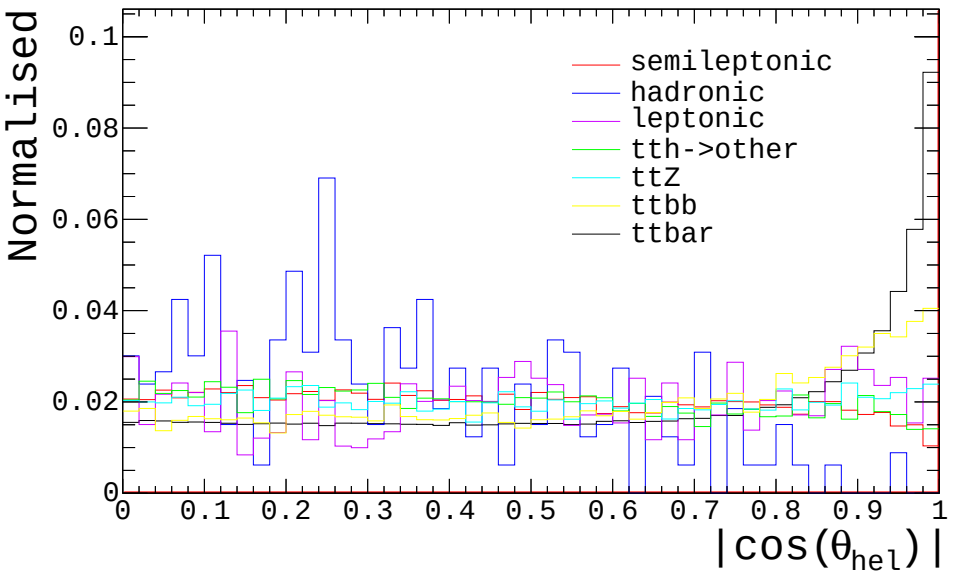

Figure 5.14: The helicity of the decay products associated with the Higgs boson relative to the Higgs direction.

output value obtained when testing the TMVA using only the events with exactly one isolated lepton in the training process. Using the number of events in 1000 fb^{-1} which passed this cut from Table 5.4, the optimal cut value from the training is 0.1325. At this value there are 208.0 signal events and 542.8 background events leading to a significance of signal selection of 7.6. Using Equation 5.2 this translates into a statistical uncertainty on $g_{t\bar{t}H}$ of 6.9%.

The number of background events passing the TMVA and isolated lepton cuts from the testing stage is the sum of all the possible backgrounds. To understand the breakdown of these backgrounds, the output weights from the TMVA training were used to evaluate the TMVA response. Figure 5.16 illustrates the response of the separate backgrounds and Table 5.5 outlines the number of events passing the cuts for each background separately. The number of events passing the cuts at the training stage differs slightly from the number here because the testing used half of the events within the samples, whereas, here all of the events are used. The numbers are not significantly different from each other.

The TMVA leads to excellent background and signal separation. The main contri-

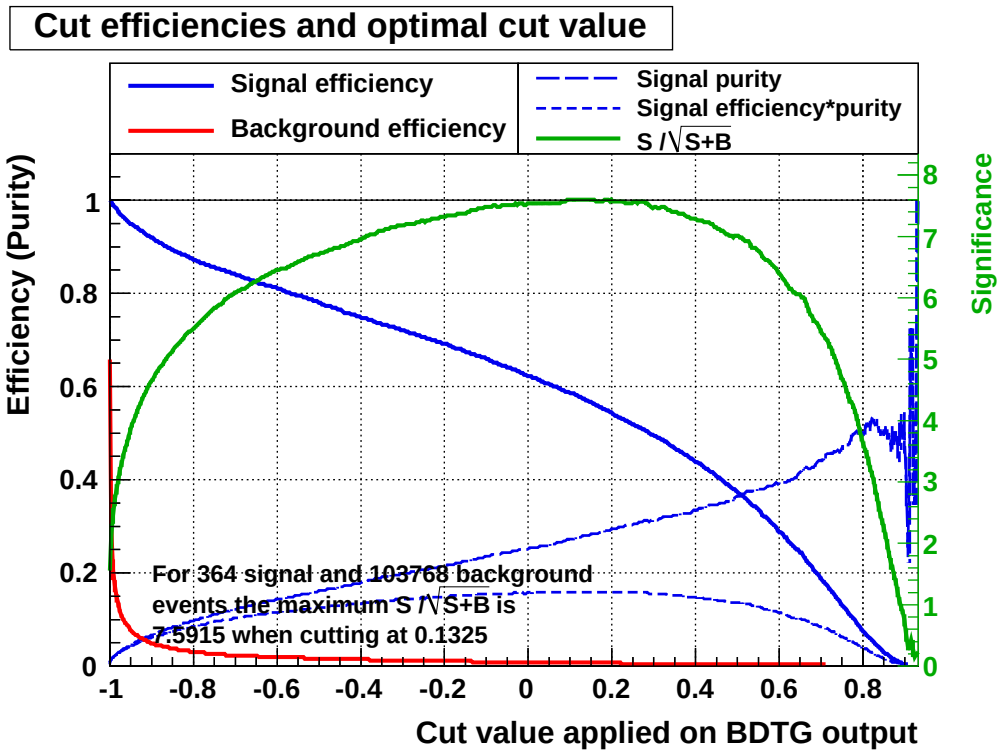

Figure 5.15: The response of the multivariate training showing the efficiency of the signal and combined background; signal purity, and significance against the BDTG value.

Table 5.5: Number of events expected in each channel after 1000 fb^{-1} for all events and the number remaining following the isolated lepton and BDTG cuts.

Cut	leptonic	semileptonic	hadronic	$t\bar{t}H \rightarrow$other	$t\bar{t}Z$	$t\bar{t}b\bar{b}$	$t\bar{t}$
Total Events	151.4	628.7	652.7	1046.1	5332.4	1434.5	308800.9
Remaining	14.8	209.7	2.1	11.1	120.4	118.0	264.0

bution to the remaining background is from $t\bar{t}$ events which are selected with an efficiency of just 0.09%. The $t\bar{t}H$ decaying to anything other than the signal contributes just 4% of the total events and as such the combination of this channel with the others was simplified in [2]. There is still a large contribution to the background from the eight fermion processes $t\bar{t}b\bar{b}$ and $t\bar{t}Z$ which was expected due to the b-tag variables being amongst the highest ranked variables for signal and background separation.

To understand fully the discriminating power of each variable in the TMVA, the training process was repeated multiple times with one variable excluded on each occasion. The b-tag_3 variable has the most discriminating power followed by the

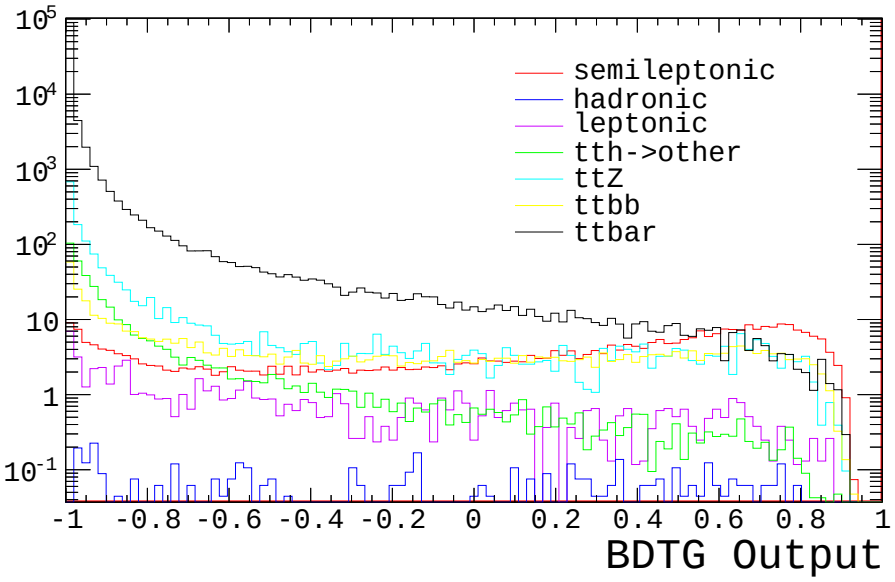

Figure 5.16: The response from the TMVA training for all channels when evaluated for all events with the backgrounds divided into the relevant channels.

thrust, E_{vis} and b-tag$_4$ as shown in Table 5.6. The other variables only have a small effect on the final significance.

In an attempt to control the backgrounds further the event reconstruction was repeated without the Higgs boson mass term (by setting σ_{bb} in Equation 5.3 to 10^7) and the TMVA was retrained without the Higgs mass to allow this to be the final discriminating variable. Due to the lowly rank of the Higgs boson mass for separation in the TMVA analysis the results of the two training processes were almost identical as outlined in Table 5.7. The distributions of the Higgs boson masses from this analysis method are, however, quite different for each channel. As shown in Figure 5.17 the signal process peaks strongly at 125 GeV as expected whereas the other backgrounds do not. The $t\bar{t}$ and $t\bar{t}b\bar{b}$ backgrounds have a much wider distribution whereas the $t\bar{t}Z$ background peaks at the Z boson mass. These variations allowed for cuts to be applied to the distributions to reduce the backgrounds. Two such cuts were applied: firstly an optimal cut on the Higgs boson mass was made at greater than 45 GeV, and secondly a narrow window around the Z boson mass was excluded. Whilst both of these mass cuts improved the signal significance the performance was still comparable to when the Higgs boson mass was included in the

Table 5.6: Response of the TMVA training when one variable was excluded from the training process.

Excluded Cut	Optimal BDTG	N_{sig}	N_{bg}	ϵ_{sig}	ρ_{sig}^{sample}	$\frac{S}{\sqrt{S+B}}$
E_{vis}	0.1073	208.9	576.7	0.57	0.27	7.45
PandoraPFOs	0.2176	193.8	466.5	0.53	0.29	7.54
Thrust	0.1254	200.3	569.7	0.55	0.26	7.22
$\log_{10}(Y_{45})$	0.2608	185.9	422.4	0.51	0.31	7.54
$\log_{10}(Y_{56})$	0.1369	207.1	540.2	0.57	0.28	7.57
b-tag$_1$	0.2403	190.7	444.6	0.53	0.30	7.57
b-tag$_2$	0.1988	197.5	486.2	0.54	0.29	7.55
b-tag$_3$	0.1116	184.5	494.0	0.51	0.27	7.08
b-tag$_4$	0.1204	207.4	564.8	0.57	0.27	7.46
χ^2	0.2510	189.3	434.1	0.52	0.30	7.58
$M_{l\nu}$	0.2346	192.0	448.3	0.53	0.30	7.59
$M_{bl\nu}$	0.2048	196.7	483.1	0.54	0.29	7.55
M_{jj}	0.1886	200.0	496.2	0.55	0.29	7.55
M_{bjj}	0.2405	191.1	446.8	0.53	0.30	7.57
M_{bb}	0.2082	195.7	484.0	0.54	0.29	7.51
$\cos(\theta_{hel})$	-0.0221	229.1	697.4	0.63	0.25	7.53

Table 5.7: Number of events expected when the Higgs boson mass was removed from the jet optimisation and TMVA training for all events, the number passed the BDTG cut, and the numbers passed cuts on the mass distributions.

Cut	leptonic	semileptonic	hadronic	$t\bar{t}H \rightarrow$other	$t\bar{t}Z$	$t\bar{t}b\bar{b}$	$t\bar{t}$	$\frac{S}{\sqrt{S+B}}$
Total Events	151.4	628.7	652.7	1046.1	5332.4	1434.5	308800.9	1.11
Remaining	17.2	210.2	2.3	10.9	125.9	126.0	278.4	7.57
$M_{b\bar{b}}$ >45	17.2	209.3	2.3	10.8	124.1	120.7	269.1	7.62
$\lvert M_{b\bar{b}} - M_Z \rvert$ >2	17.1	206.4	2.3	10.7	118.5	118.1	259.5	7.62

training.

Irrespective of the method used to train the TMVA the performance in separating the signal and backgrounds is significantly improved over the cut based method. With the Higgs boson mass constraints included the statistical uncertainty on $g_{t\bar{t}H}$ was 6.9% and 6.8% without this constraint after mass cuts had been applied.

5.9 Conclusions

The determination of how precisely the ILD will be able to measure the top Higgs Yukawa coupling was a benchmark study for the ILD TDR as it demonstrates the ability of the detector to untangle complex final states. The semileptonic decays of $t\bar{t}H$ have been studied using a cut based method and a TMVA utilising BDTGs

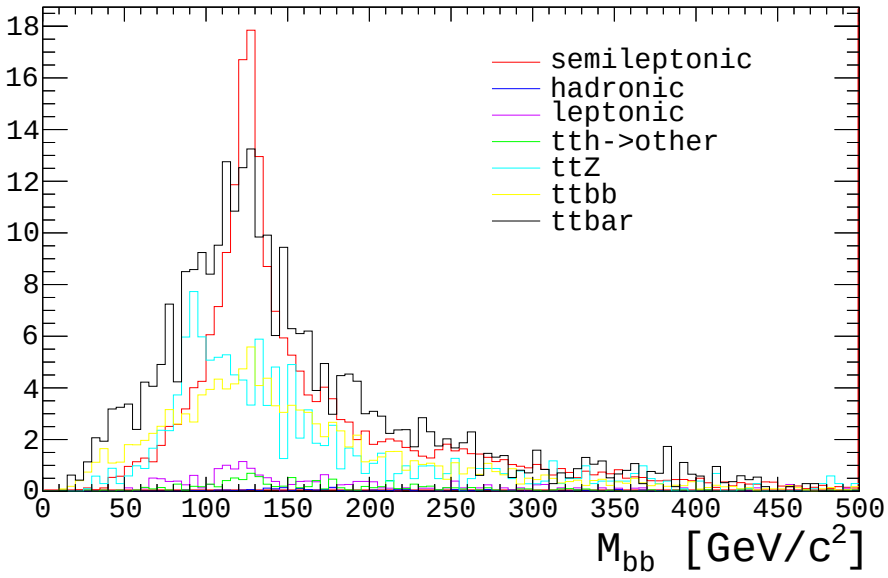

Figure 5.17: The reconstructed mass of the $b\bar{b}$ system with the Higgs mass constraint removed for events with one isolate lepton and passing the BDTG for the TMVA trained without the Higgs boson constraints.

incorporating 18 variables and has yielded a statistical uncertainty on $g_{t\bar{t}H}$ of 6.8% for the TMVA method and 9.6% for the cut based method.

CHAPTER 6

Full Scale DECAL Simulation Studies

6.1 Introduction

One of the major contributions to the cost of building a HEP detector is the ECAL. Work has been presented in earlier chapters towards the development of a technology that could be used in a low cost DECAL. In this chapter the effects on the physics of replacing the conventional Analogue Electromagnetic Calorimeter (AECAL) with a highly granular DECAL are discussed.

The procedure for simulating and reconstructing the events along with an outline of the modifications which were made to implement a DECAL are outlined in Section 6.2. The calibration of the new simulation models is outline in Section 6.3 and the response to di-jet events is given in Section 6.4. Finally, the semileptonic decay of the $t\bar{t}H$ TDR benchmark process and relevant backgrounds are reconstructed using the DECAL to investigate the effect of the DECAL on the reconstruction of

a complex final state and the impact on the precise measurement of the top Higgs Yukawa coupling.

6.2 Event Generation and Reconstruction

The work described in this chapter uses samples which I simulated and reconstructed using the BlueBEAR cluster [3] at the University of Birmingham. Four underlying samples were used:

- single photons with a monochromatic energy of 10 GeV generated with a flat $\cos(\theta)$ and ϕ dependency,
- single kaons with a monochromatic energy of 10 GeV generated with a flat $\cos(\theta)$ and ϕ dependency,
- hadronic Z boson decays at four centre of mass energies, 91, 200, 360, and 500 GeV, and
- semileptonic $t\bar{t}H$ events at 1 TeV.

A total of more than 500,000 events were simulated and reconstructed, which required over 80,000 CPU hours and occupied over 2 TB of disk space.

The single particle samples were generated using Geant4 "particle guns" within Mokka, whereas, the four vector input files for the Z boson decays and $t\bar{t}H$ samples were generated by members of the ILD Physics Analysis and Software Collaboration. The underlying $t\bar{t}H$ four vectors were generated using Physsim with a top quark mass of 175 GeV and Higgs boson mass of 120 GeV as they were generated prior to the discovery of the Higgs like boson at the LHC [16] [17].

The AECAL samples were simulated using versions of Mokka and GEANT4 consistent with iLCSoft v01-13-05 with the ILD_O1_v02 geometry model. This model

consists of a SiW ECAL with 5×5 mm^2 cell sizes, and a Steel-Scintillator HCAL with 3×3 cm^2 readout pads. For the DECAL samples the geometry was modified such that the ECAL cell sizes were reduced to 50×50 μm^2 with a sensitive epitaxial layer thickness of just 15 μm. The rest of the detector was left unchanged. Although this means the DECAL was being tested in full detector simulations which had been optimised for the AECAL, the complete optimisation of the number of layers, materials and their thicknesses, readout cable placement, and many other properties of the ECAL were beyond the scope of these studies.

The reconstruction used software packages consistent with iLCSoft v01-16. The configuration package, ILDConfig v01-15-03-p00, was used as a base configuration to create the required DSTs. These settings were the final release prior to the central sample generation for the ILD TDR and do not include the $\gamma\gamma \rightarrow$hadrons overlay. However, the settings were optimised for the ILD_o1_v05 geometry detector model and some of the settings, particularly associated with the calorimeters, needed to be modified. The processor associated with the calorimeter reconstruction was changed from LDCCaloDigi to ILDCaloDigi. Previous DECAL studies had demonstrated a $\cos(\theta)$ dependence on the reconstructed energies due to an increasing amount of passive material being traversed at higher angles. ILDCaloDigi possessed the ability to correct for these factors whereas LDCCaloDigi did not. For consistency the ILDCaloDigi method was used for both the AECAL and DECAL samples and the calorimeters were calibrated using the methods explained in Section 6.3. The PandoraPFA settings were assumed to be the same for both samples and the constants from ILDConfig v01-15-03-p00 were used.

6.3 Calibration

6.3.1 Electromagnetic Calorimeter

The response of the ECAL was characterised and calibrated using single photon events at an energy of 10 GeV. As photons are uncharged they are unaffected by the magnetic fields within the detector, do not create tracks within the tracking systems, and are fully absorbed within the ECAL meaning the only dependency on the photon reconstruction is the ECAL itself. The ILDCaloDigi package has a calibration factor, CalibrECAL, to convert from the energy deposited in the sensitive layers of the ECAL to the total energy deposited within the complete ECAL. As the energy deposited within the calorimeter was used as an input to PandoraPFA (where the settings were fixed) the value of CalibrECAL was optimised such that the total reconstructed energy of the PandoraPFOs in an event summed to the initial energy and not necessarily the total calorimeter energy.

Figure 6.1(a) and Figure 6.1(c) show the mean reconstructed energy of the photons as a function of CalibrECAL in the reconstruction for the AECAL and DECAL respectively. The reconstructed energies were fitted with a first order polynomial to identify the values of CalibrECAL which corresponded to reconstructed values of 10 GeV. The optimal value was 42.82 for the AECAL and 0.0128 for the DECAL. The large discrepancy in the numbers is caused by the vastly reduced sensitive area in the DECAL model.

Figure 6.1(b) and Figure 6.1(d) show the reconstructed photon energies using the optimised values of CalibrECAL in the reconstruction of the AECAL and DECAL samples. When the reconstructed energy is fitted with a Gaussian distribution the means of the distributions are consistent within errors with 10 GeV. However, the DECAL single photon energy resolution is reduced by 25 % as the width of the distribution increases from 0.61 GeV in the AECAL model to 0.76 in the DECAL.

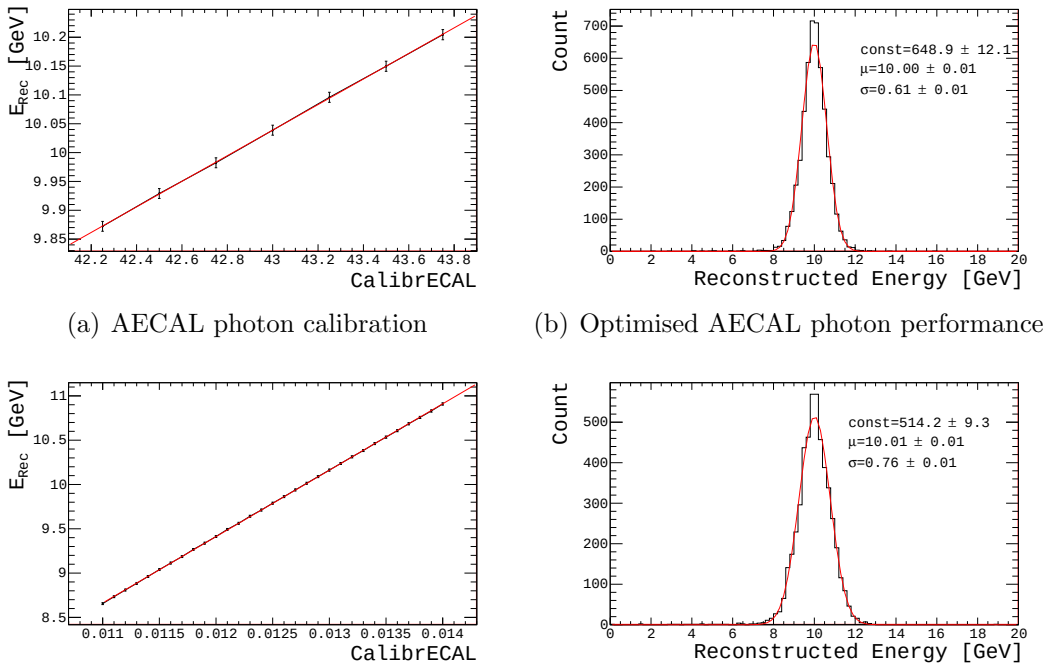

(a) AECAL photon calibration

(b) Optimised AECAL photon performance

(c) DECAL photon calibration

(d) Optimised DECAL photon performance

Figure 6.1: Calibration co-efficients versus the total reconstructed energy of the PandoraPFOs in an event and the optimised single photon response for the AECAL (top) and DECAL (bottom)

6.3.2 Hadronic Calorimeter

Naively, one would expect the performance of the HCAL to be unchanged due to the geometry modifications only affecting the ECAL. However, hadronic particles deposit a finite, non negligible amount of energy in the ECAL before entering the HCAL and its response was recalibrated to account for any effects of the DECAL. Uncharged K_L's were chosen to calibrate the HCAL due to their long time of flight meaning only a small fraction decay into charged particles before reaching the HCAL minimising the amount of energy lost and allowing the best calibration to be made. As with the ECAL calibrations, there was a parameter in ILDCaloDigi, CalibrHCAL, which was optimised to achieve the required reconstructed peaks at 10 GeV. The values obtained in the previous section for CalibrECAL were used to account for energy deposited within the ECAL.

Figure 6.2(a) and Figure 6.2(c) demonstrate the behaviour of the mean reconstructed

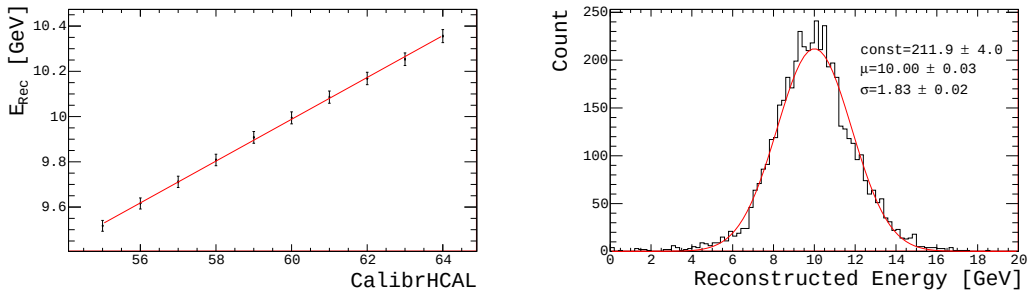

(a) AECAL K_L calibration

(b) Optimised AECAL K_L performance

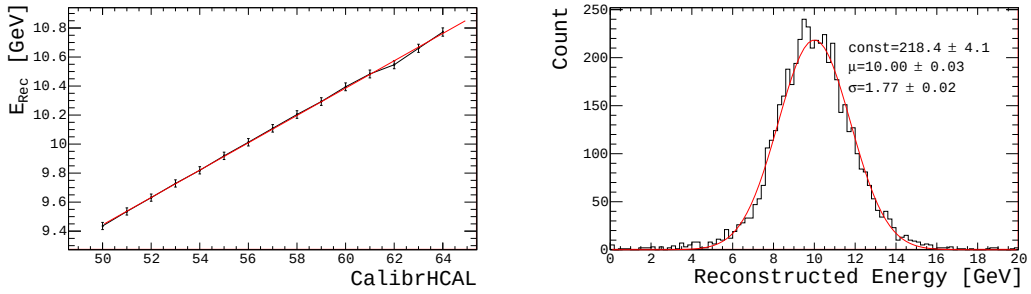

(c) DECAL K_L calibration

(d) Optimised DECAL K_L performance

Figure 6.2: Calibration co-efficients versus the total reconstructed energy of the PandoraPFOs in an event and the optimised kaon response for the AECAL (top) and DECAL (bottom)

energies as a function of CalibrHCAL. Figure 6.2(b) and Figure 6.2(d) show the performance at optimal values of CalibrHCAL of 60.1 and and 55.9 for the AECAL and DECAL. The inclusion of the DECAL has a negligible affect on the performance of the HCAL as the reconstructed energies for both geometries peak at 10 GeV as expected and the widths are compatible within one standard deviation.

6.4 Jet Energy Resolution

The energy and momentum resolutions of a detector utilising PFA have a large dependence on the tracking systems as well as the calorimeters meaning that single particle studies which test individual components are insufficient to evaluate the performance of the complete detector. As explained in Section 2.2.11, the perfor-

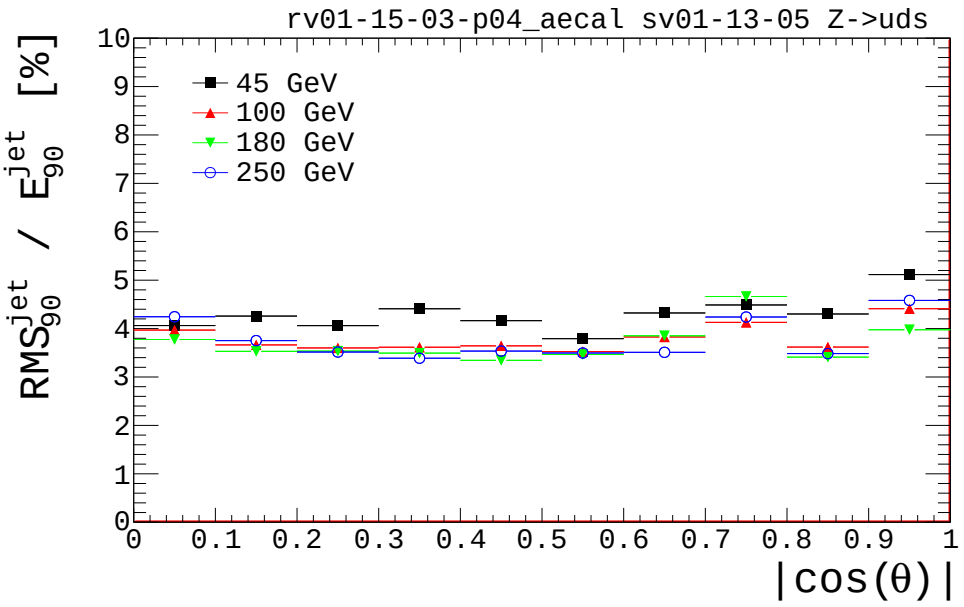

Figure 6.3: Jet energy resolution ($\frac{RMS_{90}}{E_{90}}$) as a function of angle from the beamline for the Z→uds events at centre of mass energies of 91, 250, 360, and 500 GeV for the AECAL using iLCSoft v01-13-05 and reconstruction v01-15-03-p04_aecal.

mance of the reconstruction is evaluated using Z→uds[1] events. The reconstruction of such events coupled the optimised values of CalibrECAL and CalibrHCAL from the previous sections with the standard reconstruction parameters from ILDConfig v01-15-03-p00. The modified versions of ILDConfig were tagged as v01-15-03-p04_aecal and v01-15-03p-05_decal for the AECAL and DECAL reconstructions respectively.

Figure 6.3 demonstrates the jet energy resolution versus the angle relative to the incoming beam for the Z→uds events for a detector with an AECAL. In the barrel region of the detector the required jet energy resolution of ∼4 % is achieved for all energies, with significantly better performance for energies above 45.5 GeV. There are observed increases between 0.7< $|\cos(\theta)|$ <0.8 due to the transition between the barrel and endcaps in the detector, and $|\cos(\theta)|$ >0.9 due to events very close to the beamline. These features have been observed in both the LOI [47] and TDR [23] (also see Figure 2.8(b)) using centrally generated samples and as such the simulation and reconstruction processes set-up for the AECAL and DECAL studies are considered as validated for the rest of the this chapter.

[1]events where the Z decays to a $q\bar{q}$ pair where q=u,d,s.

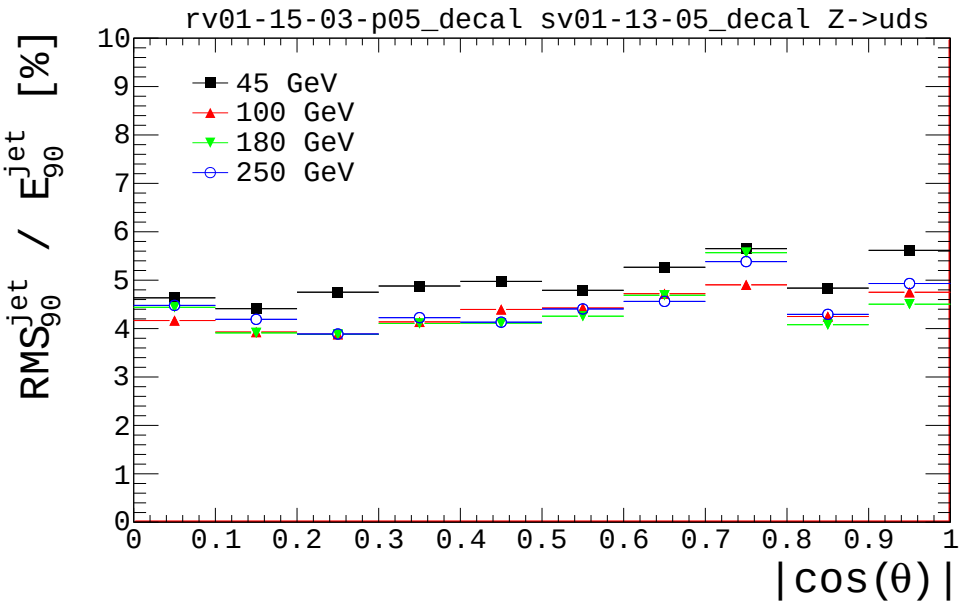

Figure 6.4: Jet energy resolution ($\frac{RMS_{90}}{E_{90}}$) as a function of angle from the beamline for the Z→uds events at centre of mass energies of 91, 250, 360, and 500 GeV for the DECAL using iLCSoft v01-13-05_decal and reconstruction v01-15-03-p05_decal.

The equivalent plot for a detector incorporating the DECAL is shown in Figure 6.4. As with the photons, the jet energy resolution is marginally reduced with the introduction of the DECAL across all four energies at all angles. Similar properties are observed to the AECAL with a decrease in the resolution at the cross over from barrel to endcap and close to the beamline. Considering that the geometry and all but two of the calibration factors are optimised for the AECAL model, this is a very promising result for a detector including a DECAL. There is also a small increase in jet energy resolution as the jet angle increases through the barrel implying that the angular dependence of the DECAL is not being fully corrected within ILDCaloDigi. Without the angular corrections the performance is further degraded indicating the corrections are working but are not optimised. At the level of sophistication appropriate for the AECAL/DECAL comparisons, the optimisation was considered adequate.

The jet energy resolutions are better than those achieved for single photons in both the AECAL and DECAL cases as the PandoraPFOs are reconstructed using all aspects of the detector. Figure 6.4 also demonstrates that the DECAL would be

a viable technology at a linear collider using the current reconstruction software available due to the ability of PandoraPFA to cope with the increased number of reconstructed clusters in the DECAL with only a marginal impact on the performance.

6.5 $e^+e^- \to t\bar{t}H$ Reconstruction

Previous studies into the impact of the DECAL have concentrated on single particles [101] or simple physics analyses such as $e^+e^- \to ZH$ or $e^+e^- \to \tau\tau$ at 500 GeV as presented here [102]. Whilst these studies are essential to understand the performance of the DECAL the topologies of the final states are not overly complex (single photons, two taus or four jets). To complement the studies in Chapter 5, the semileptonic decay mode of $e^+e^- \to t\bar{t}H$ with the Higgs boson decaying into a $b\bar{b}$ pair was studied to assess the effect of the DECAL on a complex final state.

6.5.1 Event Reconstruction

Due to the complex final state the analysis was split into stages and at each stage characteristics were compared for the different technologies. Firstly the reconstructed particles were searched for the presence of an "isolated lepton" as explained in Section 6.5.2. The isolated leptons were removed from the collection of particles and only events with exactly one isolated lepton were kept for the analysis. Following the identification of isolated leptons the neutrino was reconstructed by accrediting all of the missing energy and momenta in the event to the neutrino. Finally, the remaining reconstructed particles were forced into six Durham jets and flavour tagged using the LCFIPlus package. The leptonic top quark was reconstructed using the isolated lepton, neutrino and one jet tagged as a b-jet, the hadronic top quark was reconstructed using the two least b-like jets and a b-jet, and the Higgs boson reconstructed from the remaining two b-jets in the event. The optimal combination of jets

to reconstruct the event followed the procedure in Section 5.6 with the appropriate values of M_H and M_t for these samples used as input to Equation 5.3.

6.5.2 Isolation Criteria

To ensure a clean sample of events in the reconstructed final state only events where the W boson decayed into a muon were considered. A cone of fixed radius corresponding to an angle of 0.2 radians was constructed around each muon and the sum of the energy of all of the particles within this cone, E_{cone}, excluding the muon itself, was calculated. The muon was deemed to be isolated if

$$\frac{E_{cone}^2}{E_{muon}^2 - E_{cut}^2} \leq 1 \ , \tag{6.1}$$

where E_{muon} is the energy of the muon at the centre of the cone, and E_{cut} is a parameter optimised to maximise the significance of selecting a muon from the W decay rather than a lepton in a jet. Figure 6.5 is a scatter plot of the values of E_{muon} and E_{cone} for muons from W decays and all other leptons in the event where a clear division between the two types of lepton is visible. From this plot an optimised value of E_{cut}=15 GeV was obtained.

The fraction of events with exactly one muon tagged as isolated were found to be similar for both technologies (see Figure 6.6(a)). As the same underlying four vectors were used for each technology and the energy distributions of the isolated muons are very similar for both the AECAL and DECAL it is assumed that the same muons are being tagged as isolated.

6.5.3 Neutrino Reconstruction

The reconstruction of the neutrino is highly sensitive to the performance of the whole detector due to the assumption that all of the missing energy and momentum

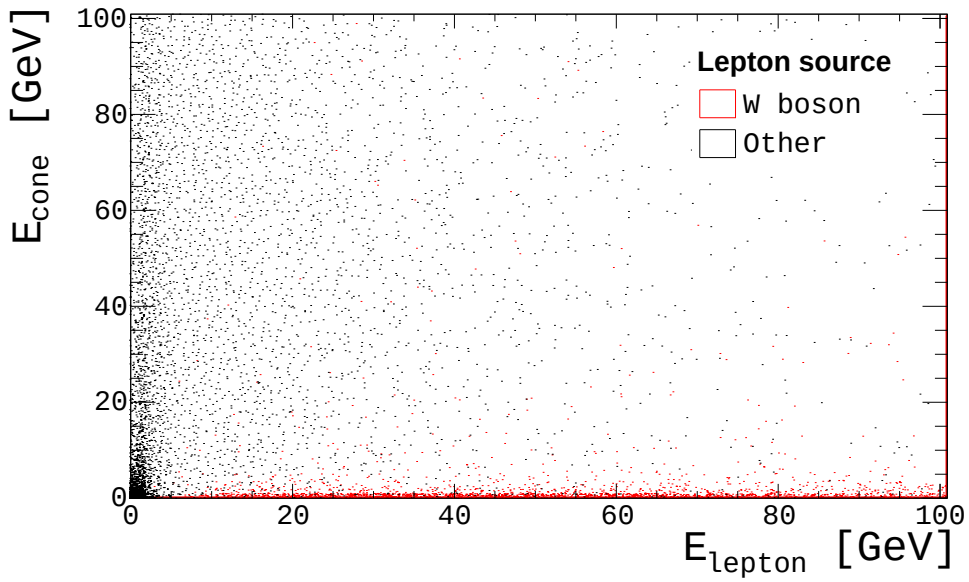

Figure 6.5: Scatter plot of the energy of the muon versus the energy of the surrounding cone for all muons coming from a W boson decay (red) and all other leptons in the event from all other sources (black).

is associated with the neutrino. The presence of ISR was not studied as the four vector inputs into the simulations were identical in both the AECAL and the DECAL cases and therefore, any effects of the ISR cancelled in the comparisons. Figure 6.7(a) shows that the neutrino energy is, in general, off shifted to higher values by a few GeV indicating that the total visible energy in the event is slightly underestimated for the DECAL. Figure 6.7(b) reinforces this as the value of E_{ν}^{MC} - E_{ν}^{Reco} peaks at a marginally lower value for the DECAL than for the AECAL. The slight difference is attributed to the parameters in PandoraPFA being optimised for the standard AECAL case.

6.5.4 Reconstructed Masses

The reconstructed masses of the W bosons, top quarks, and Higgs boson for the optimal combination of jets obtained by minimising Equation 5.3 for the AECAL and DECAL samples are shown in Figure 6.8. The widths of the reconstructed leptonic W boson and top quark masses are dominated by the neutrino reconstruction and

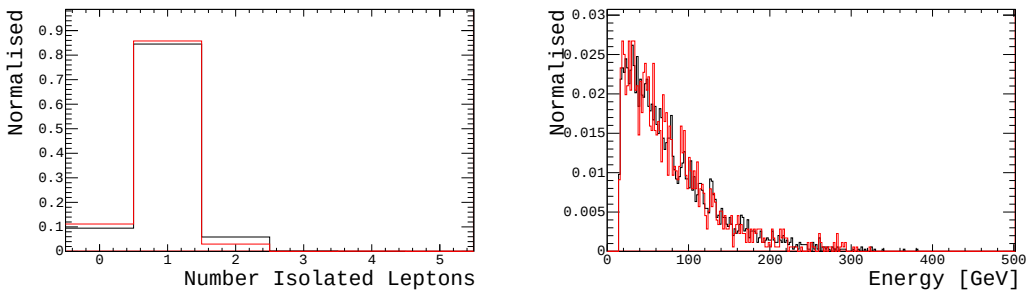

(a) Isolated muons per event

(b) Energy of isolated muons

Figure 6.6: Properties of the isolated lepton identification performance with the fraction of events corresponding the each number of isolated leptons 6.6(a), and the energies of the isolated leptons 6.6(b) for the AECAL (black) and DECAL (red).

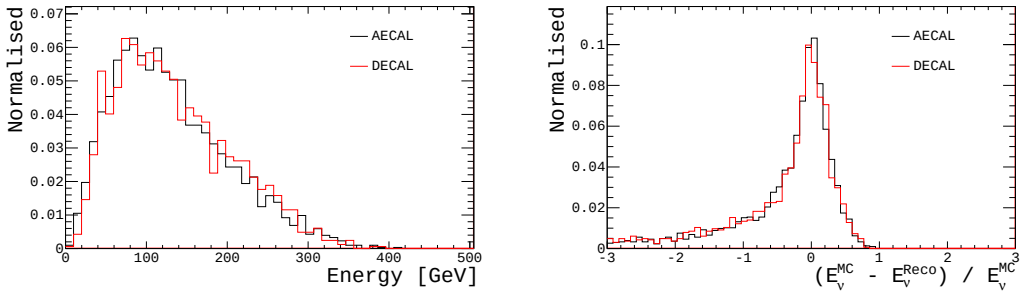

(a) Reconstructed energy

(b) Reconstructed energy resolution

Figure 6.7: Reconstructed energy of the neutrino 6.7(a) and the corresponding energy resolutions 6.7(b) for the AECAL (black) and DECAL (red).

are thus wider than the corresponding particles from the hadronic decays. The reconstruction of the leptonically decaying top quark is insensitive to differences between the AECAL and DECAL. The widths of the reconstructed masses of the hadronic W boson and top quark are narrower due to the increased certainty of the reconstruction using only hadronic jets. In the hadronic W reconstruction there are long tails around the true mass due to confusion within the jet finding or where the wrong combination of jets has been used. This is supported by Figure 6.9(c) where the resolution of the hadronic W mass is very good in a narrow window with large shoulders where the resolution is degraded from the confusion. There is a slight increase in the reconstructed masses of the hadronic top quark and Higgs boson for the DECAL which is attributed to the optimised parameters for the AECAL being

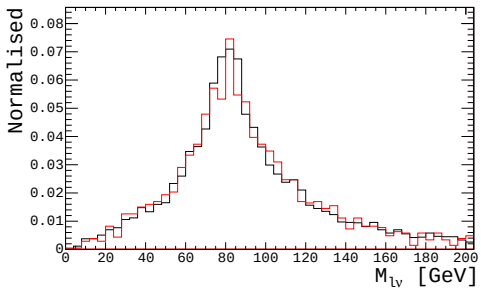

(a) Leptonic W boson candidate

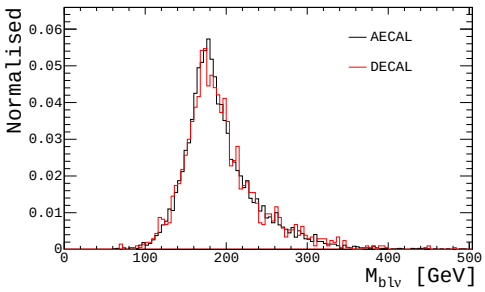

(b) Leptonic top quark candidate

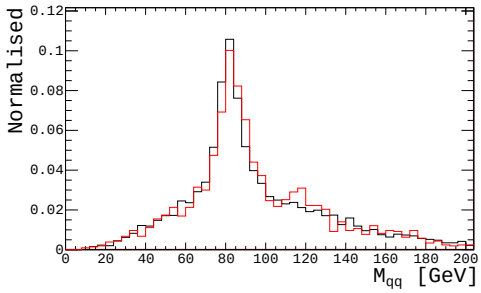

(c) Hadronic W boson candidate

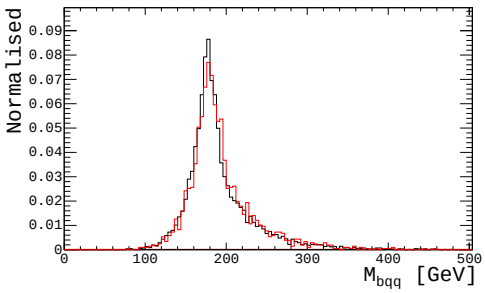

(d) Hadronic top quark candidate

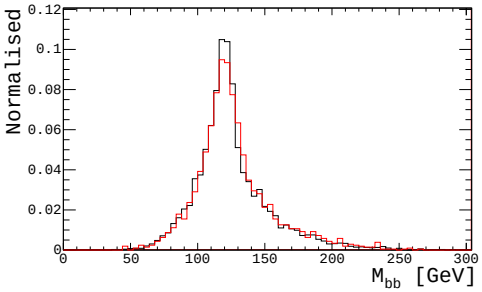

(e) Higgs boson candidate

Figure 6.8: The reconstructed masses of the leptonic W boson candidate (6.8(a)), leptonic top quark candidate (6.8(b)), hadronic W boson candidate (6.8(c)), hadronic top quark candidate (6.8(d)), and Higgs boson candidate (6.8(e)) for the AECAL (black) and DECAL (red).

used in the DECAL reconstructions.

Overall, Figure 6.9 demonstrates that the resolutions of the reconstructed masses of the final state are in excellent agreement even though the single photon and jet energy resolutions are slightly worse for the DECAL. This is a consequence of the confusion when clustering the jets and finding their optimal configuration being a larger factor in the mass resolution than that of the intrinsic jet energy resolution.

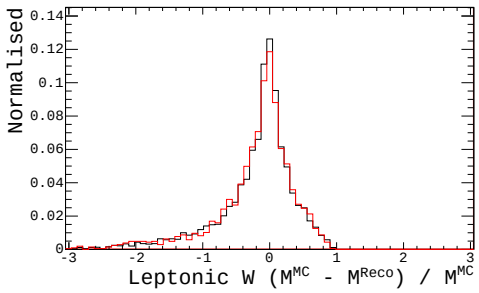

(a) Leptonic W boson candidate

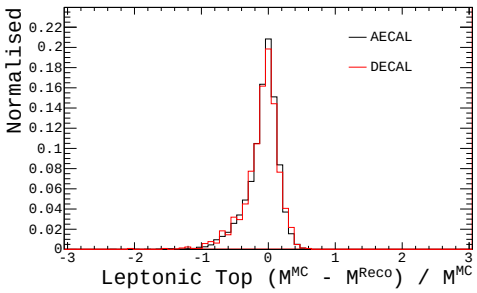

(b) Leptonic top quark candidate

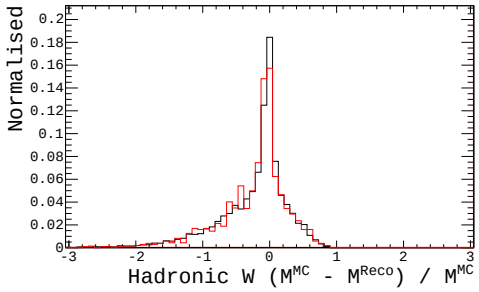

(c) Hadronic W boson candidate

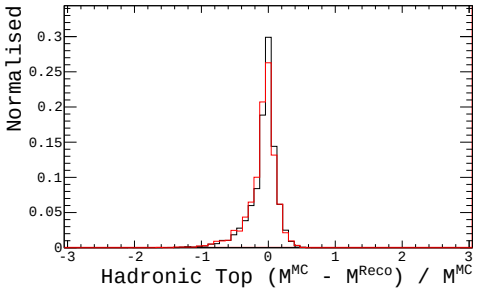

(d) Hadronic top quark candidate

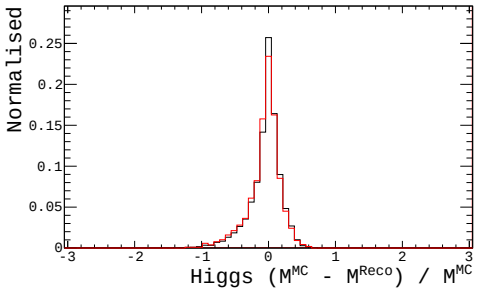

(e) Higgs boson candidate

Figure 6.9: The reconstructed mass resolutions of the leptonic W boson candidate (6.9(a)), leptonic top quark candidate (6.9(b)), hadronic W boson candidate (6.9(c)), hadronic top quark candidate (6.9(d)), and Higgs boson candidate (6.9(e)) for the AECAL (black) and DECAL (red).

This is an excellent result for the DECAL as it demonstrates that for a reduced cost in building the detector the physics performance is not degraded.

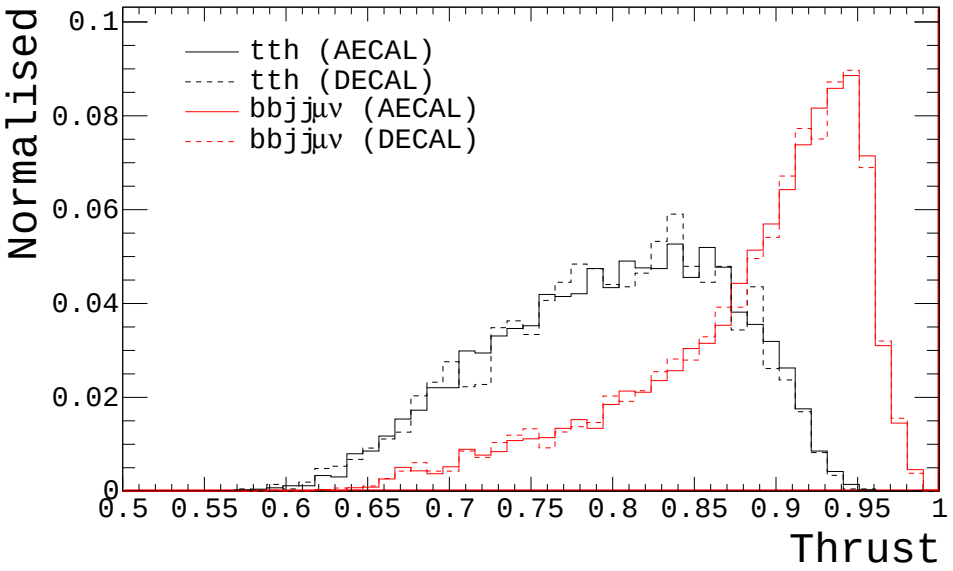

Figure 6.10: The calculated thrust of the event for both the semileptonic $t\bar{t}H$ (black) and the $t\bar{t}$ channel including four jets and one muon (red) for the AECAL (solid lines) and DECAL (dashed lines).

6.5.5 Treatment of Backgrounds

As shown in the previous section, the reconstruction of the semileptonic $t\bar{t}H$ channel is unchanged whether simulated with the AECAL or the DECAL geometries. It is fairly safe to assume that the backgrounds will also be unchanged and a selection of variables were studied to test this hypothesis. In Table 5.6 the main discriminating variables between the signal and the backgrounds are the thrust of the event and the b-tag properties. To evaluate the potential of the DECAL to select signal events whilst rejecting the background these two variables are evaluated for the $t\bar{t}$ channel where one W boson decays to a muon and a neutrino and the other decays hadronically.

Figure 6.10 demonstrates the calculated thrust of an event for the $t\bar{t}H$ semileptonic and the $t\bar{t}$ samples for the AECAL (solid line) and the DECAL (dashed line). The thrust distributions for the two technologies are very similar and the distinguishing power of the thrust variable is therefore preserved. This result was not totally unexpected as the thrust is a global property of the event and is not strongly dependent

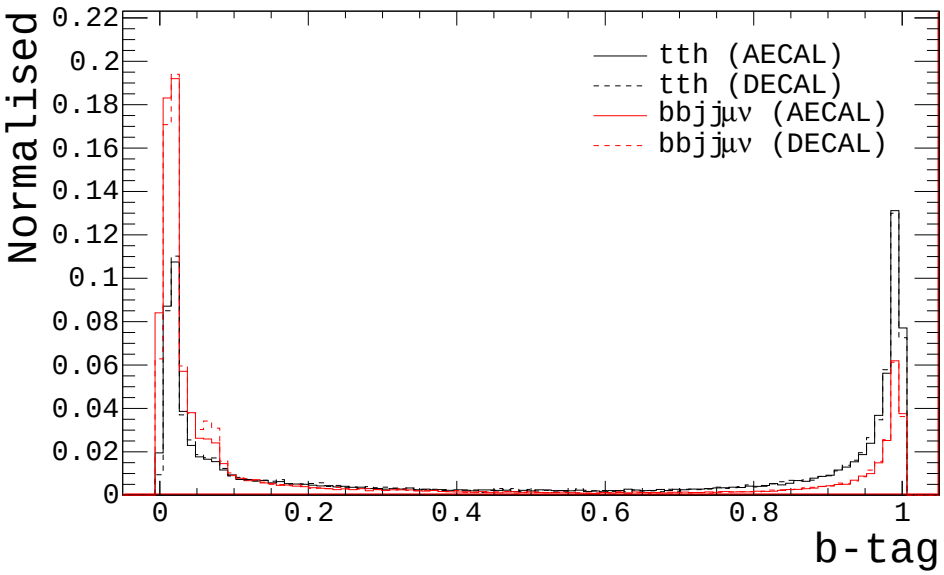

Figure 6.11: The b-tag values of all the jets in an event for both the semileptonic $t\bar{t}H$ (black) and the $t\bar{t}$ channel including four jets and one muon (red) for the AECAL (solid lines) and DECAL (dashed lines).

on the detector design.

The distributions for the b-tag values of all of the jets in an event for the $t\bar{t}H$ and $t\bar{t}$ samples are given in Figure 6.11. Once again, only the $t\bar{t}$ decaying to a final state with four jets and a muon was studied. Due to there only being two b-jets in the $t\bar{t}$ samples the distributions have more entries at low values compared with the four in the $t\bar{t}H$ samples. The distributions are unchanged when the DECAL is introduced. As the b-tagging procedure in LCFIPlus is heavily dependent on the reconstruction of PandoraPFOs in the detector this is a very important result as it demonstrates that the reconstruction is not hindered by the information obtained from the DECAL.

Whilst the reconstructed masses for the $t\bar{t}H$ channel are unchanged it is important to evaluate how well $t\bar{t}H$ can be distinguished from $t\bar{t}Z$ given the slightly reduced jet energy resolution achieved with the DECAL and the relatively similar expected masses of the Z and Higgs bosons. The mass term of the $b\bar{b}$ system was removed from Equation 5.3 such that the optimisation concentrated on reconstructing the two top

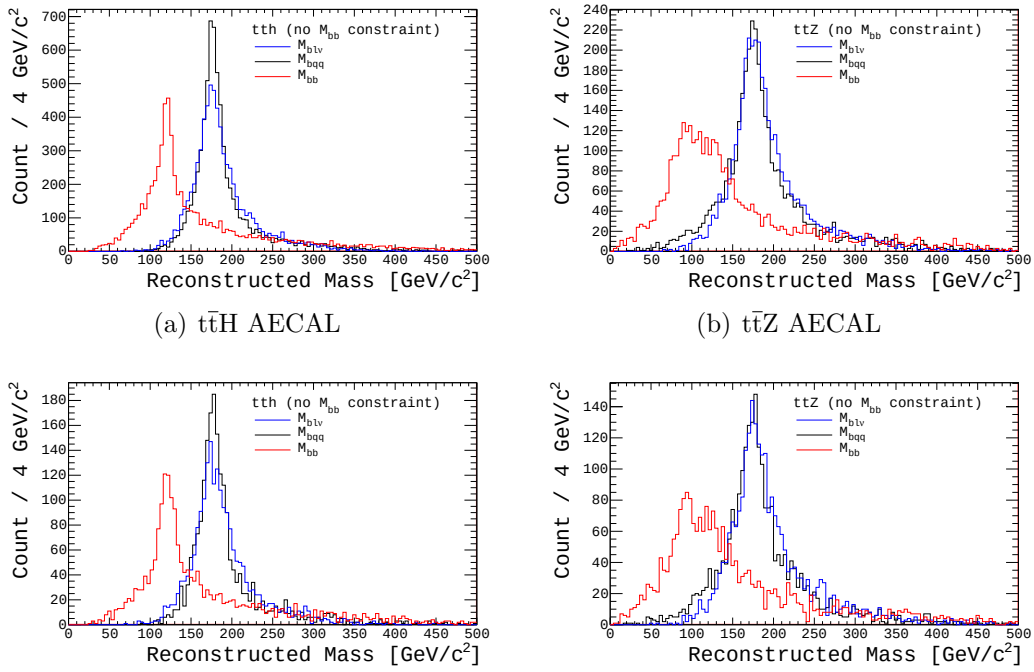

(a) $t\bar{t}H$ AECAL (b) $t\bar{t}Z$ AECAL

(c) $t\bar{t}H$ DECAL (d) $t\bar{t}Z$ DECAL

Figure 6.12: The reconstructed masses for the two top quarks and $b\bar{b}$ pair when the Higgs mass constraint is removed for the $t\bar{t}H$ and $t\bar{t}Z$ channels when using the AECAL (top) and DECAL (bottom).

quarks, leaving the reconstructed H/Z boson masses as a discriminant. Figure 6.12 demonstrates that the top quarks in all four of the samples are reconstructed with the expected behaviour with the resolution of the leptonically decaying top quark candidate being slightly worse. In the $t\bar{t}H$ samples for both the AECAL and DECAL the mass of the $b\bar{b}$ system peaks strongly around the expected 120 GeV. The mass of the $b\bar{b}$ system in the $t\bar{t}Z$ samples also peaks around the expected value of 90 GeV but with a much wider distribution caused by the optimisation procedure having been trained for the $t\bar{t}H$ channel and not the $t\bar{t}Z$.

The masses of the $b\bar{b}$ system for the $t\bar{t}H$ and $t\bar{t}Z$ channels with both detector geometries are overlaid in Figure 6.13. Whilst the Z and Higgs boson candidates peaks are separate the large tail at higher masses associated with the Z boson candidate means it is hard to distinguish between the two channels on a mass only basis. The ability to separate the masses is not degraded by the addition of the DECAL as

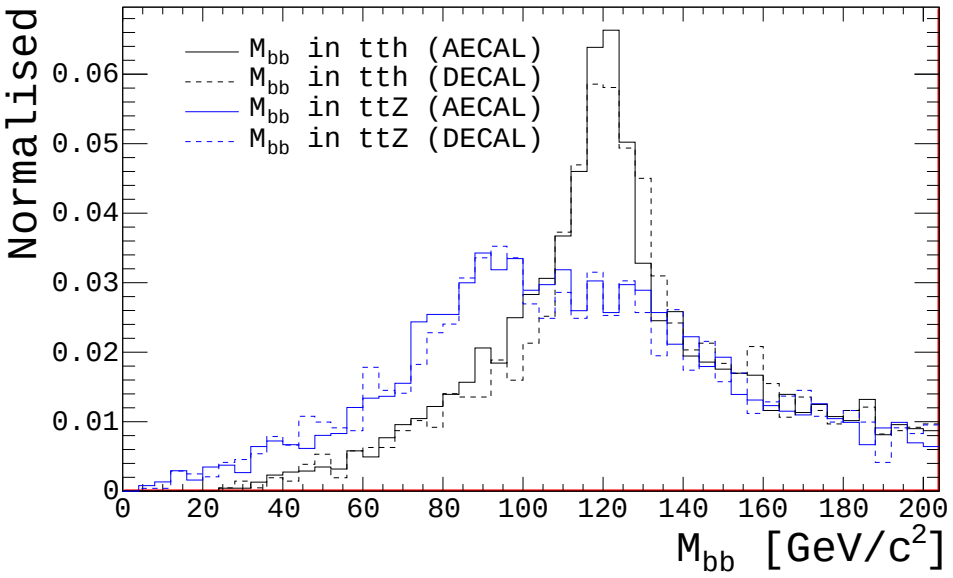

Figure 6.13: The reconstructed mass of the $b\bar{b}$ system when the Higgs mass constraint is removed for the $t\bar{t}H$ (black) and $t\bar{t}Z$ (blue) samples for the AECAL (solid lines) and DECAL (dashed lines).

the peaks Z/H peaks do not move closer together as initially feared due to reduced di-jet energy resolutions.

As the distributions of the thrust, b-tag values, and reconstructed masses are unaffected by switching to the DECAL it is assumed that all of the cut variables used in the analysis will follow the same pattern for all backgrounds. Therefore, the precision of measuring the top Higgs Yukawa coupling for a detector utilising a DECAL will be comparable to that of one using the conventional SiECAL as used in the simulation studies in Chapter 5.

6.6 Conclusions

The detector model ILD_O1_v02 has been modified in such a way that the area of the ECAL cell sizes have been reduced by a factor of 10^4 and drastically thinned to allow the implementation of a DECAL.

The standard procedure used by the ILD Collaboration to calibrate both the old ILD_O1_v02 geometry and the new DECAL geometry has been performed using single photons, single kaons, and di-jet events. The energy resolution of single photons was observed to degrade by ∼25% for the DECAL model. The response to kaons, which is dominated by the HCAL but has a non-negligiable contribution from the ECAL was unchanged. Using the standard configuration parameters for the PandoraPFA reconstruction, as optimised for the AECAL, a di-jet energy resolution RMS_{90}/E_{90} of between 4% and 6% has been demonstrated for the DECAL. The design goal for the ILD is 4% to distinguish between Z and W bosons and this is achieved for the higher energy jets in the barrel region. The performance could be further improved and potentially brought into agreement with the AECAL samples by optimising the PandoraPFA parameters for the DECAL geometry.

When a complex, mulit-jet final state was studied the differences in the jet energy resolution were not propagated to the final reconstructed masses of the optimal combination of jets, primarily due to the contribution from the jet energy resolution being smaller than the confusion in the jet clustering. The main backgrounds associated with the signal channel were studied in terms of the main discriminating variables (thrust and b-tagging) and the distributions were found to be unchanged for the DECAL compared to the conventional AECAL meaning the sensitivity of measuring the top Higgs Yukawa coupling will be unchanged.

These results suggest that a cheaper calorimeter system could be used to study the complex multijet final states at the ILC as the confusion of the jet clustering algorithms dominates intrinsic energy resolution of the detector.

CHAPTER 7

Discussion and Conclusions

With the discovery of a Higgs boson at the LHC we are currently at a very exciting time in HEP. However, the challenging nature of the complex final state in a hadron collider, coupled with the added problems which arise from pile-up at the LHC, place limits upon the accuracy of many measurements. In order to fully understand the properties of the Higgs boson a new experiment is required which collides fundamental particles to have a much cleaner and better understood signal.

The proposed ILC will collide electrons and positrons at $\sqrt{s} \leq 1$ TeV, yielding highly precise collisions into which all of the beam energy will be avaliable for the production of new particles. The centre of mass energy will be upgraded and tuned in different stages of running to ensure that a full scan of the SM and the Higgs boson up to TeV energies can be made. In order to fully take advantage of the cleaner initial state avaliable at lepton colliders the detectors will require unprecedented performance to reconstruct unambiguously events with multiple jets, leptons, and missing energy in the signal.

The work in this thesis has focused on developing a novel calorimeter system for the ILD at the proposed ILC. The concept of a DECAL is to measure the number of particles in a particle shower which removes the Landau fluctuations associated with the energy deposited in thin layers of material. This allows, in theory, a jet energy resolution to be obtained which is closer to the intrinsic resolution arising from fluctuations of the shower production mechanisms. The TPAC sensor was developed for such a purpose. The performance of the TPAC sensors has been successfully tested during beam tests using pions and electrons at CERN and DESY.

Studies into the electrical properties of the sensor yielded very promising results where the design goals of the sensor were met. One such goal was the development of a low noise sensor and with an observed noise rate of 0.2 hits/timestamp/sensor at a threshold of 180 DTU, this has been achieved.

A stack of six TPAC sensors operated successfully and tracks were formed through the stack to allow properties such as cluster sizes, single particle efficiencies, shower multiplicities and shower densities to be studied. The high resistiviy sensors demonstrated an improved single particle efficiency relative to the standard sensors at higher thresholds with calculated efficiencies comparable to those achieved in earlier studies by members of the collaboration.

An increased shower multiplicity was observed for electrons with higher incident energies in the sensors downstream of the showering material. This demonstrated an essential property of a DECAL where, for an increasing incident particle energy the observed multiplicity increases. For a fixed energy the multiplicity for increasing amounts of material follows the same trend as the energy deposition rate in a conventional ECAL. This result was especially pleasing due to the shower being wider than the sensor size causing an incomplete measurement of the shower and suggests that excellent, highly granular measurements of an electromagnetic shower would be possible with a larger physics prototype and allow the validation of simulation models. However, the severe funding restrictions placed upon the SPiDeR Collaboration following the withdrawal of support from the UK funding agency prevented

the construction of such a prototype. Following the beam test analyses the SPiDeR Collaboration evolved into Arachnid which used the next generation of sensor designed by SPiDeR, with particular attention paid to applications within a tracking system.

A simulation was developed in an attempt to validate the results obtained from the beam test data. However, due to the fine interplay between tiny energy deposits, charge spreading and threshold conversion factors the efficiency of digitised hits gave vastly lower than expected particle efficiency results. Following the presentation of the beam test results at the CALICE Collaboration meeting in Cambridge and LCWS12 in Arlington, Texas, an offer of help was made by members of the linear collider community with expertise in the modelling of silicon sensors. This illustrates the interest in these studies of the wider HEP community, as an understanding of the properties of low energy electromagnetic showers validated by data is essential for future detectors which will require an increased granularity.

In order to evaluate the potential of using the TPAC sensors for future applications, the radiation hardness of the sensors was evaluated. The noise in the TPAC sensors increased by between 2.5 % and 8 % at 200 krad for various sensor biases rising to 21 % at 5000 krad for a sensor held at ground during exposure. The S/N has been shown to fall by a maximum of 8 % in sensors at a dose of 200 krad. At 5000 krad, the S/N has reduced by just 15 % which is very promising for future applications. The observed changes in S/N are independent of epitaxial layer type as the sensors irradiated whilst powered were all in agreement.

When the sensors were irradiated whilst powered, problems developed in the shift register. The reduced dose rate gave rise to a vastly reduced number of configuration errors in the shift register. A dose rate of 6 rad/s yielded just three bad columns compared to greater than 20 bad columns for a dose rate of 60 rad/s. The dose rate received by the SIT, SET, and the ECAL in CLIC ILD, and the ECAL in ILC ILD is orders of magnitude lower than 6 rad/s and as such the shift register issues would not present a problem even using the current TPAC technology. Future applications

of the technology used for the TPAC sensors in higher radiation environments would require a redesign of the shift register which loads the configuration data into the pixels.

The radiation studies presented in this thesis, together with studies performed on the TPAC sensor by the ALICE Inner Tracking Systems Upgrade team[1], have lead to the CMOS development centre at RAL being associated with ALICE to develop a next generation of sensor. This sensor will potentially be used in the upgrades and will be based on parts of the underlying TPAC technology.

The performance of the ILD to untangle complex events was also studied using the semileptonic decay of $e^+e^- \rightarrow t\bar{t}H$. Full scale detector simulations were conducted and studied for the final state which contained six jets, a lepton and missing energy from the neutrino. The reconstruction of such events proved to be very successful and allowed a prediction of 6.9% on the precision with which measurements of the top quarks coupling to the Higgs boson could be made. This study was combined with a study of the hadronic decay by Tomohiko Tanabe of KEK in the ILD TDR to address one of the essential physics benchmarks for the process and yielded a prediction precision of just 4.3% on the measurement of the top Higgs Yukawa coupling at the ILC operating at $\sqrt{s}$=1 TeV. This measurement was in excellent agreement with the same studies conducted for the SiD detector and a combined paper is proposed to demonstrate the expected overall performance of the two detectors for the ILC for this channel.

The ILD model was modified in such a way that the area of the ECAL cell sizes have been reduced by a factor of 10^4 and the active depth of silicon drastically thinned to allow the implimentation of a DECAL. Full Geant4 simulations and event reconstructions were performed using software packages consistent with the TDR samples for the $e^+e^- \rightarrow t\bar{t}H$ channel to produce samples where the detector utilised both the conventional ECAL and the DECAL. These allowed the impact of the inclusion of the DECAL technology on physical measurements to be studied.

[1]of which the author assisted in the setting up of the systems and advised on work to be carried out

The DECAL was calibrated using standard techniques employed by the ILD Collaboration and demonstrated a jet energy resolution compatible with the centrally generated samples. Considering that the callibration coefficients in the reconstruction were largely optimised for the conventional calorimeter system this is an excellent result for two reasons. Firstly, the current implementation of PandoraPFA can handle the increased number of hits and still reconstruct the event, and secondly, the implementation of the DECAL does not have a detrimental effect on the intrinsic performance of the detector.

When the semileptonic decay of $e^+e^- \rightarrow t\bar{t}H$ was studied the small differences observed in the jet energy resolution were not propagated to the final reconstructed masses of the optimal combination of jets, primarily because the contribution from the jet energy resolution was smaller than the confusion in the jet clustering. The main backgrounds associated with the signal channel were studied in terms of the main discriminating variables (thrust and b-tagging) and the distributions were found to be unchanged for the DECAL compared to the conventional AECAL. It follows that the sensitivity of measuring the top Higgs Yukawa coupling will also be unchanged.

The results in this thesis support the idea of a digital electromagnetic calorimeter. Whilst there is still work to be done to create a physics prototype, the prototype sensors have demonstrated the required properties and have measured particle showers which, considering only a small fraction of the shower was sampled at one time, are in excellent agreement with theoretical shower development models. As the physics performance of a detector which uses a DECAL is largely unchanged the results suggest that a much cheaper calorimeter system could be built and, therefore, the DECAL is a viable option for future HEP detectors.

APPENDIX A

PMT Beam Test Setup

Beam particles traversing the TPAC stack were detected by three scintillation counters. Upstream of the stack were two scintillators at 90° to each other with a third downstream of the stack. Each plastic scintillator had a lateral size of 10×10 mm^2 to match the size of the sensors and a thickness of 6 mm to ensure that sufficient amounts of light is produced. The scintillators were connected to perspex light guides which tapered at its end to match the 8 mm diameter window of a miniature Hamamatsu PMT.

The PMT gain was set by a supply voltage with a typical control voltage of 0.65 V which could be modified via a potentiometer. The output of the PMT was fed into a discriminator where the voltage was amplified by a factor of 10 and compared against a threshold of 50 mV as illustrated in the schematic shown in Figure A.1. The logic output from the comparators was fed into the Master DAQ as shown in Figure A.2

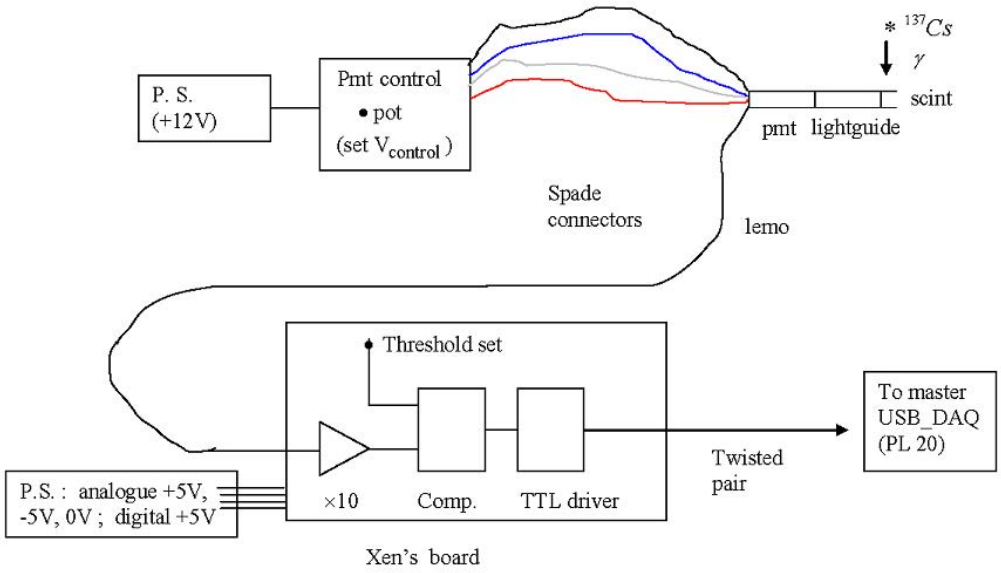

Figure A.1: Schematic of the scintillator circuit

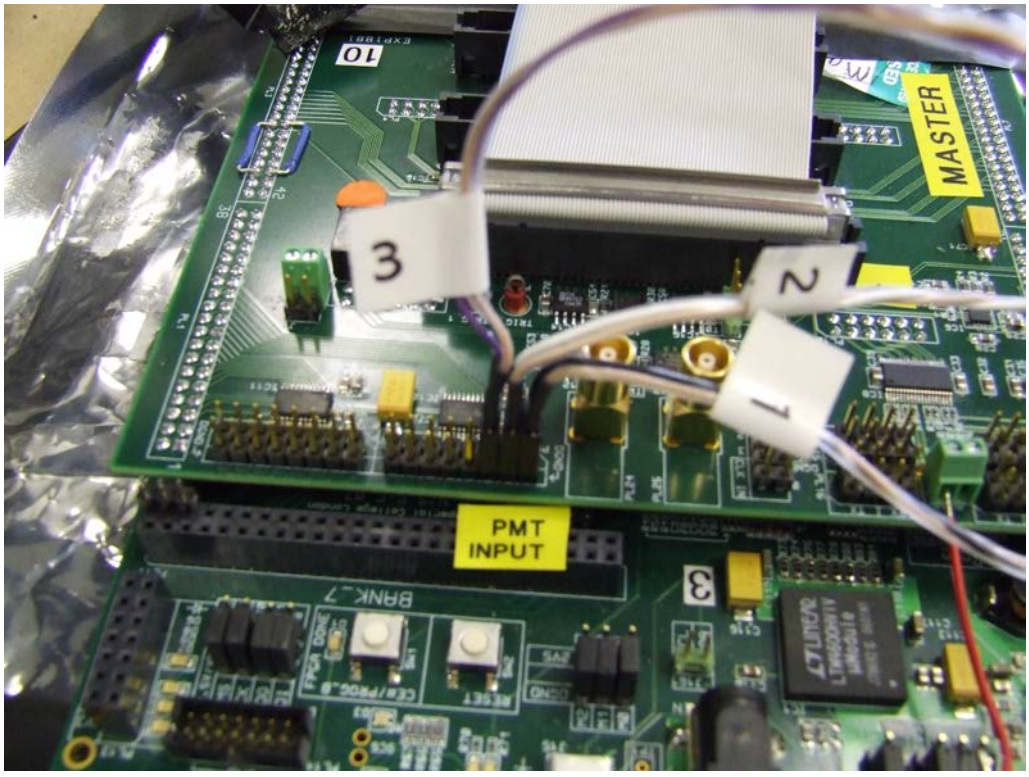

Figure A.2: Output from comparator to the Master DAQ

Table A.1: The settings used for the PMTs which surrounded the TPAC stack and acted as a trigger. H6780 and H5783 are Hamamatsu PMTs.

Device	PMT	$V_{control}$ [V]	Comparator Threshold [mV]
H6780	1	0.70	50
H5783	2	0.60	50
H6780	3	0.65	50

The control voltage was calibrated using a ^{137}Cs gamma source with an energy of 0.662 keV. A MIP will deposit at least 1.2 MeV in the 6 mm thick scintillator and the supply voltage from the Caesium source was set such that the signal size significantly exceeded the comparator threshold, to ensure that a true beam particle would easily trigger the comparator. The final settings for the control voltages for each PMT are given in Table A.1.

APPENDIX B

Beam Test Simulations

In an attempt to isolate each component of the simulations and understand the differences with respect to the beam test data, one variable was modified at a time. As the emlivermore physics list best described the data these studies focused on this list. The efficiencies for a complete threshold scan for the emlivermore physics list are compared against data showing the obvious discrepancies which arise from low thresholds.

Range Cuts

In Geant4 the maximum range on secondaries is specified as a distance rather than an energy cut due to particles having different ranges in different materials. With an epitaxial layer of 12 μm, if the minimum step is larger than this then a step in the layer may be missed. The range was reduced in stages down to 10 nm and

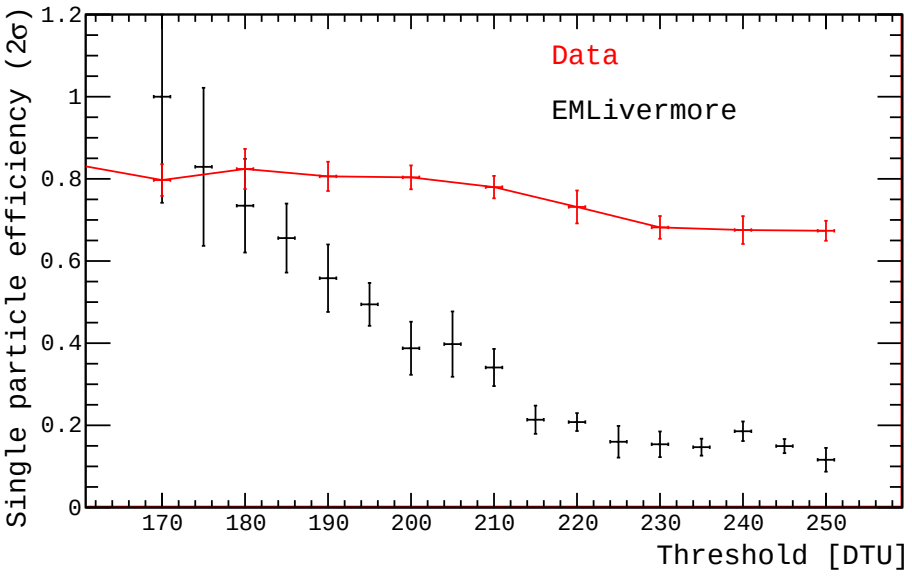

Figure B.1: The efficiencies for a complete threshold scan for the emlivermore physics list compared to data

the resulting number of truth hits is shown in Figure B.2. The range cuts have a minimal effect on the number of particles so this range is not a problem.

Charge Spread Models

The charge spread model was modified in an attempt to keep a greater fraction of charge in the struck pixel by using data files produced for differing epitaxial layer resistivities as shown in Figure B.3. A minor improvement is made to the efficiency with the "REAL_DPW.dat" files but the efficiency was still well below the expected level. When a configuration file was used which did not include the INMAPS process the efficiency effectively dropped to zero for all thresholds.

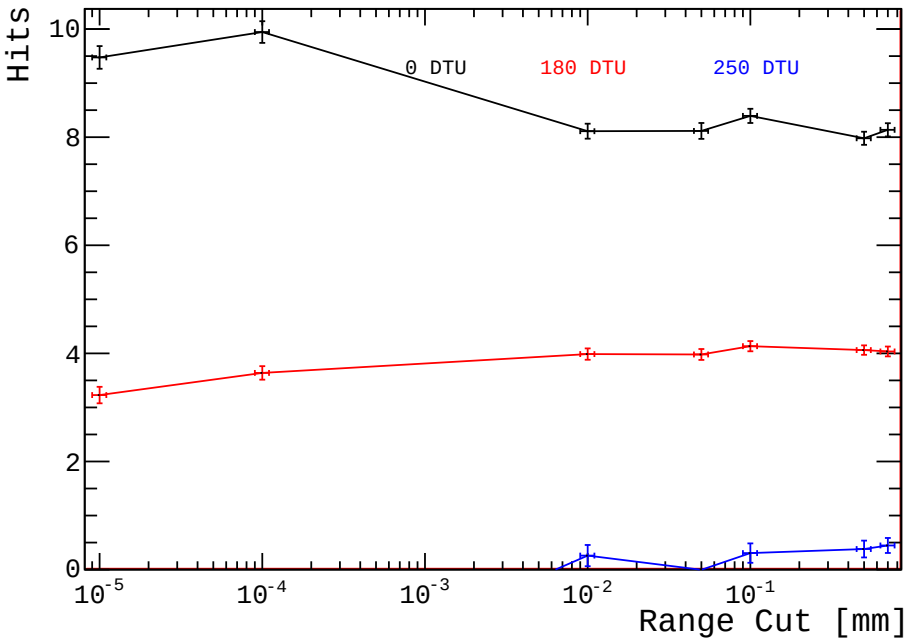

Figure B.2: The number of truth particles as a function of the range cut for secondaries. This simulation uses 4 GeV electrons, passing through 4 χ_0 of tungsten with the emliver-more physics list.

Additional Charge Deposition

To isolate the potential of incorrect charge deposition within Geant4 the charge deposited by a particle was increased before charge spreading up to an additional 5 keV, in steps of 100 eV. Figure B.4 shows the efficiencies for various amounts of additional charge and compares them to data. The additional charge causes saturation effects at lower thresholds where the efficiency is 100% for a large range of thresholds but still dips below the required efficiency at larger thresholds.

Pedestal Spreads

During running, noise in the sensors causes a pedestal spread for fully trimmed sensors of 1.25 DTU (see Section 4.3). This was modelled into the threshold cuts but when coupled with the extra charge deposition no obvious fluctuations arose.

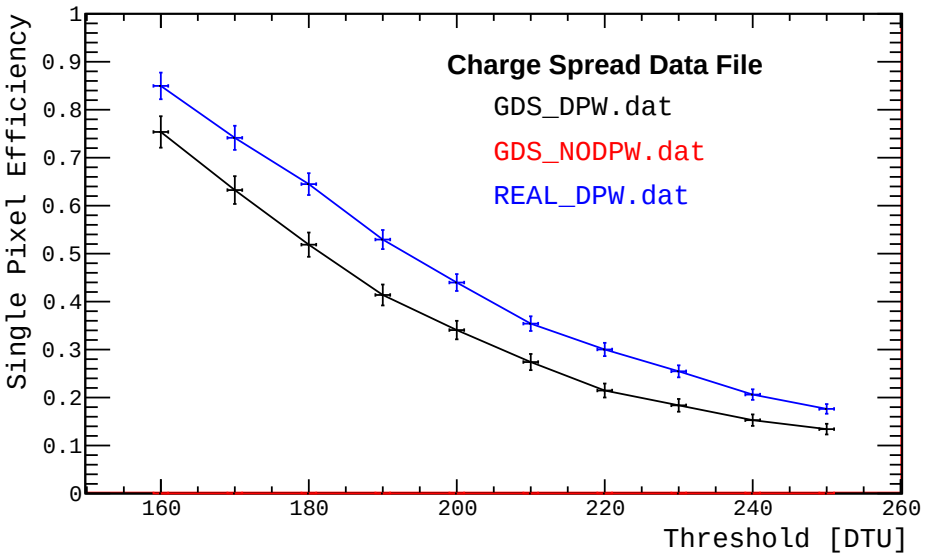

Figure B.3: The efficiencies for a complete threshold scan for the emlivermore physics list for various charge spread models.

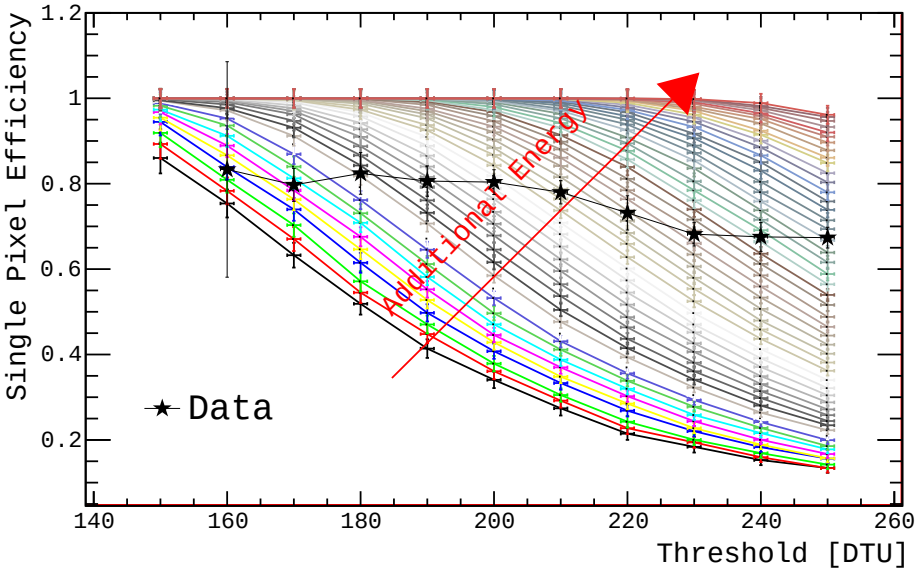

Figure B.4: The efficiencies for a complete threshold scan with the emlivermore physics list for various amounts of additional charge. The corresponding data points obtained at the DESY beam test for a standard 12 μm sensor are overlaid for reference.

Bibliography

[1] T. Price, N. Watson, *et al.*, "First radiation hardness results of the terapixel active calorimeter (tpac) sensor" *JINST* **8** (2013) no. 01, P01007.

[2] T. Price *et al.*, "Measurement of the top Yukawa coupling at $\sqrt{s} = 1$ TeV using the ILD detector".

[3] "Birmingham Environment for Academic Research". `https://intranet.birmingham.ac.uk/it/teams/infrastructure/fm/bear/index.aspx`.

[4] E. Hubble, "A relation between distance and radial velocity among extra-galactic nebulae" *Proc.Nat.Acad.Sci.* **15** (1929) 168–173.

[5] A. Liddle, *An Introduction to Modern Cosmology*. Wiley, 2003.

[6] A. A. Penzias and R. W. Wilson, "A Measurement of excess antenna temperature at 4080-Mc/s" *Astrophys.J.* **142** (1965) 419–421.

[7] **Planck Collaboration**, P. Ade *et al.*, "Planck 2013 Results. I. Overview of Products and Scientific Results" `arXiv:1303.5062 [astro-ph.CO]`.

[8] **Particle Data Group**, J. Beringer *et al.*, "Review of Particle Physics" *Phys. Rev. D* **86** 010001.

[9] D. Griffiths, *Introduction to Elementary Particles*. Wiley, 2008.

[10] A. Hoecker and W. J. Marciano, "The Muon Anomalous Magnetic Moment" *Particle Data Group* (2012) .

[11] E. Noether, "Invariant Variation Problems" *Transport Theory and Statistical Physics* **1** (1971) 186–207.

[12] P. W. Higgs, "Broken Symmetries and the Masses of Gauge Bosons" *Phys. Rev. Lett.* **13** (1964) 508–509.

[13] P. W. Higgs, "Spontaneous Symmetry Breakdown without Massless Bosons" *Phys. Rev.* **145** (1966) 1156–1163.

[14] **LEP Working Group for Higgs boson searches, ALEPH Collaboration, DELPHI Collaboration, L3 Collaboration, OPAL Collaboration**, R. Barate *et al.*, "Search for the standard model Higgs boson at LEP" *Phys.Lett.* **B565** (2003) 61–75.

[15] **CDF Collaboration, D0 Collaboration**, T. Aaltonen *et al.*, "Higgs Boson Studies at the Tevatron" `arXiv:1303.6346 [hep-ex]`.

[16] **ATLAS Collaboration**, G. Aad *et al.*, "Observation of a new particle in the search for the Standard Model Higgs boson with the ATLAS detector at the LHC" *Phys.Lett.* **B716** (2012) 1–29.

[17] **CMS Collaboration**, S. Chatrchyan *et al.*, "Observation of a new boson at a mass of 125 GeV with the CMS experiment at the LHC" *Phys.Lett.* **B716** (2012) 30–61.

[18] "Combined coupling measurements of the Higgs-like boson with the ATLAS detector using up to 25 fb^{-1} of proton-proton collision data" Tech. Rep. ATLAS-CONF-2013-034, CERN, Geneva.

[19] G. Bernardi, M. Carena, and T. Junk, "Higgs bosons: Theory and Searches" *Particle Data Group* (2012) .

[20] J. M. Campbell, J. W. Huston, and W. J. Stirling, "Hard interactions of quarks and gluons: a primer for LHC physics" *Reports on Progress in Physics* **70** (2007) no. 1, 89.

[21] R. Wigmans, *Calorimetry: Energy Measurement in Particle Physics*. Clarendon Press, 2000.

[22] K. Kleinknecht, *Detectors for Particle Radiation*. Cambridge University Press, 1998.

[23] T. Behnke, J. E. Brau, P. N. Burrows, J. Fuster, M. Peskin, M. Stanitzki, Y. Sugimoto, S. Yamada, and H. Yamamoto, "The International Linear Collider Technical Design Report - Volume 4: Detectors" *ArXiv e-prints* (2013) , `arXiv:1306.6329 [physics.ins-det]`.

[24] L. Linssen, A. Miyamoto, M. Stanitzki, and H. Weerts, "Physics and Detectors at CLIC: CLIC Conceptual Design Report" `arXiv:1202.5940`.

[25] **The CALICE Collaboration**, R. Poeschl *et al.*, "Calorimetry for Lepton Collider Experiments - CALICE results and activities" `arXiv:1212.5127`.

[26] "CALICE-UK Home Page". `http://www.hep.ph.ic.ac.uk/calice/`.

[27] R. Turchetta, "CMOS Sensors for the Detection of Minimum Ionising Particles" in *Proceedings of the 2001 IEEE Workshop on Charge-Coupled Devices and Image Sensors*, pp. 7–9. Lake Tahoe, Nevada, USA, June, 2001.

[28] Fossum, E. R., "CMOS image sensors: electronic camera-on-a-chip" *IEEE Transactions on Electron Devices* **44** (1997) no. 10, 1689–1698.

[29] R. Turchetta *et al.*, "A monolithic active pixel sensor for charged particle tracking and imaging using standard VLSI CMOS technology" *NIM A* **458** (2001) no. 3, 677–689.

[30] **CLIC Physics Working Group**, E. Accomando *et al.*, "Physics at the CLIC multi-TeV linear collider" `arXiv:hep-ph/0412251 [hep-ph]`.

[31] "Compact Linear Collider". `http://clic-study.org/`.

[32] **The SPiDeR Collaboration**, N. Watson *et al.*, "DESY PRC Report, Oct 2009".

[33] Ballin, J. A. and others, "Monolithic Active Pixel Sensors (MAPS) in a quadruple well technology for nearly 100% fill factor and full CMOS pixels" *Sensors 2008* (2008) 5336–5351.

[34] J. Ballin *et al.*, "Design and performance of a CMOS study sensor for a binary readout electromagnetic calorimeter" *JINST* **6** (2011) P05009.

[35] **SPiDeR Collaboration**, P. Dauncey, "Performance of CMOS sensors for a digital electromagnetic calorimeter" *PoS* **ICHEP2010** (2010) 502.

[36] G. Arnison *et al.*, "Experimental observation of isolated large transverse energy electrons with associated missing energy at $\sqrt{s}$=540 GeV" *Phys. Lett. B* **122** (1983) no. 1, 103 – 116.

[37] M. Banner *et al.*, "Observation of single isolated electrons of high transverse momentum in events with missing transverse energy at the CERN pp collider" *Phys. Lett. B* **122** (1983) no. 56, 476 – 485.

[38] **ALEPH Collaboration, DELPHI Collaboration, L3 Collaboration, OPAL Collaboration, LEP Electroweak Working Group**, S. Schael *et al.*, "Electroweak Measurements in Electron-Positron Collisions at W-Boson-Pair Energies at LEP" `arXiv:1302.3415 [hep-ex]`.

[39] H. Baer, T. Barklow, K. Fujii, Y. Gao, A. Hoang, *et al.*, "The International Linear Collider Technical Design Report - Volume 2: Physics" `arXiv:1306.6352 [hep-ph]`.

[40] R. Yonamine, K. Ikematsu, T. Tanabe, K. Fujii, Y. Kiyo, *et al.*, "Measuring the top Yukawa coupling at the ILC at $\sqrt{s} = 500$ GeV" *Phys.Rev.* **D84** (2011) 014033.

[41] H. Tabassam and V. Martin, "Top Higgs Yukawa Coupling Analysis from $e^+e^- \to t\bar{t}H \to bWbWbb$" arXiv:1202.6013 [hep-ex].

[42] "LC images and graphics". http://www.linearcollider.org/images/.

[43] N. Walker, "ILC TDR Beam Parameters". http://ilc-edmsdirect.desy.de/ilc-edmsdirect/item.jsp?edmsid=D00000000925325, 2012.

[44] B. Banish, "Introduction to the ILC". http://ilcagenda.linearcollider.org/getFile.py/access?contribId=2&sessionId=0&resId=0&materialId=slides&confId=5636, 2012.

[45] Y. Papaphilippou and J. Urakawa, "Low emmitance generation and preservation: Damping rings". http://ilcagenda.linearcollider.org/getFile.py/access?contribId=260&sessionId=1&resId=0&materialId=slides&confId=5468, 2012.

[46] N. Phinney, N. Toge, and N. Walker, "LC Reference Design Report Volume 3 - Accelerator" arXiv:0712.2361 [physics.acc-ph].

[47] **ILD Concept Group - Linear Collider Collaboration**, T. Abe *et al.*, "The International Large Detector: Letter of Intent" arXiv:1006.3396 [hep-ex].

[48] "ILC - International Linear Collider". http://www.linearcollider.org/ilc.

[49] **GLD Concept Study Group**, K. Abe *et al.*, "GLD Detector Outline Document: Version 1.2" arXiv:physics/0607154 [physics].

[50] T. Behnke, "The LDC Detector Concept" *Pramana* **69** (2007) 697–702.

[51] **The ALEPH Collaboration**, D. Decamp *et al.*, "ALEPH: A detector for electron-positron annihilations at LEP" *NIM A* **294** (1990) no. 12, 121 – 178.

[52] **The OPAL Collaboration**, "The OPAL detector at LEP" *NIM A* **305** (1991) no. 2, 275 – 319.

[53] **D0 Collaboration**, S. Abachi *et al.*, "The D0 Detector" *NIM A* **338** (1994) 185–253.

[54] **The CDF Collaboration**, F. Abe *et al.*, "The CDF detector: An Overview" *NIM A* **271** (1988) no. 3, 387 – 403.

[55] **The ATLAS Collaboration**, "The ATLAS Experiment at the CERN Large Hadron Collider" *JINST 3 S08003* (2008) .

[56] **The CMS Collaboration**, "The CMS experiment at the CERN LHC" *JINST 3 S08004* (2008) .

[57] **The ALICE Collaboration**, "The ALICE experiment at the CERN LHC" *JINST 3 S08002* (2008) .

[58] M. Thomson, "Particle flow calorimetry and the PandoraPFA algorithm" *NIM A* **611** (2009) no. 1, 25 – 40.

[59] C. Hu-Guo *et al.*, "First reticule size MAPS with digital output and integrated zero suppression for the EUDET-JRA1 beam telescope" *NIM A* **623** (2010) 480–482.

[60] L. Reuen *et al.*, "Performance of a DEPFET prototype module for the ILC vertex detector" *Nuclear Science, IEEE Transactions on* **53** (2006) no. 3, 1719–1725.

[61] T2K ND280 TPC collaboration, "Time Projection Chambers for the T2K Near Detectors" `arXiv:1012.0865 [physics.ins-det]`.

[62] G. De Lentdecker, "A large TPC prototype for an ILC detector" in *2009 IEEE*, pp. 2283–2285. 2009.

[63] C. Adloff *et al.*, "Response of the {CALICE} Si-W electromagnetic calorimeter physics prototype to electrons " *NIM A* **608** (2009) no. 3, 372 – 383.

[64] **CALICE Collaboration**, S. Uozumi, "Performance of the scintillator-strip electromagnetic calorimeter prototype for the linear collider experiment" *J.Phys.Conf.Ser.* **293** (2011) 012070.

[65] T. Yoshioka and H. Ueno, "Simulation study of the hybrid ECAL". `http://ilcagenda.linearcollider.org/materialDisplay.py?contribId=53&sessionId=9&materialId=slides&confId=5686`, 2012.

[66] **CALICE Collaboration**, M. Chadeeva, "Hadron Energy Resolution of the CALICE AHCAL and Software Compensation Approaches" `arXiv:1202.6184 [physics.ins-det]`.

[67] **CALICE Collaboration**, C. Adloff *et al.*, "Construction and commissioning of the calice analog hadron calorimeter prototype" *JINST* **5** (2010) P05004.

[68] F. Dulucq, C. De la Taille, G. Martin-Chassard, and N. Seguin-Moreau, "HARDROC: Readout chip for CALICE/EUDET Digital Hadronic Calorimeter" in *Nuclear Science Symposium Conference Record (NSS/MIC), 2010 IEEE*, pp. 1678–1683. 2010.

[69] V. Boubry, "First results of the SDHCAL". `http://ilcagenda.linearcollider.org/getFile.py/access?contribId=124&sessionId=15&resId=0&materialId=slides&confId=5468`, 2012.

[70] W. Placzek *et al.*, "Precision calculation of Bhabha scattering at LEP" `arXiv:hep-ph/9903381 [hep-ph]`.

[71] H. Abramowicz, A. Abusleme, K. Afanaciev, J. Aguilar, P. Ambalathankandy, *et al.*, "Forward Instrumentation for ILC Detectors" *JINST* **5** (2010) P12002.

[72] "LCFIPlus Variables - Linear Collider - SLAC Confluence". `https://confluence.slac.stanford.edu/display/ilc/LCFIPlus+Variables`.

[73] T. Price, "MAPS Technology for Vertexing, Tracking, and Calorimetry" *Physics Procedia* **37** (2012) 932 – 939.

[74] J. J. Velthuis *et al.*, "Beam test results of FORTIS, a 4T MAPS sensor with a signal-to-noise ratio exceeding 100" *JINST* **6** (2011) no. 12, P12006.

[75] "CERN - the European Organization for Nuclear Research". `http://public.web.cern.ch/public/`.

[76] "Short Introduction to the use of the H6 beam". `http://sba.web.cern.ch/sba/BeamsAndAreas/h6/H6manual.pdf`.

[77] CERN, "Secondary Beams & Areas". `http://sba.web.cern.ch/sba/BeamsAndAreas/resultbeam.asp?beamline=H6`.

[78] "Deutsches Elektronen-Synchrotron DESY". `http://www.desy.de/`.

[79] T. Behnke, E. Garutti, I.-M. Gregor, T. Haas, U. Kotz, I.-A. Melzer-Pellmann, N. Meyners, J. Mnich, and F. Sefkow, "Test Beams at DESY".

[80] "The mean and variance of the discrete uniform distribution Digital explorations". `http://adorio-research.org/wordpress/?p=519`.

[81] F. Sefkow, "Partial Shower Development in a W Scintillator HCAL 1–10 GeV/c Momentum Range". `http://ilcagenda.linearcollider.org/getFile.py/access?contribId=116&sessionId=15&resId=0&materialId=slides&confId=5468`, 2012.

[82] S. Agostinelli *et al.*, "Geant4 – a simulation toolkit" *NIM A* **506** (2003) no. 3, 250 – 303.

[83] "Installing Geant4 Release 4.9.4 on Linux". `http://geant4.slac.stanford.edu/tutorial/installation/Geant4.9.4/Linux/Geant4_9_4_Linux_Installation.htm`.

[84] "Physics Lists EM constructors in Geant4 9.4". http://geant4.cern.ch/geant4/collaboration/working_groups/electromagnetic/physlist9.4.shtml.

[85] A. Valentin, M. Raine, J.-E. Sauvestre, M. Gaillardin, and P. Paillet, "Geant4 physics processes for microdosimetry simulation: Very low energy electromagnetic models for electrons in silicon" *NIM B* **288** (2012) no. 0, 66 – 73.

[86] L. Musa, "Conceptual Design Report for the Upgrade of the ALICE ITS" Tech. Rep. CERN-LHCC-2012-005. LHCC-G-159, CERN, Geneva, Mar, 2012.

[87] A. Bevan, J. Crooks, A. Lintern, A. Nichols, M. Stanitzki, R. Turchetta, and F. Wilson, "Design study for a next generation B factory pixel vertex detector" *NIM A* **643** (2011) no. 1, 29 – 35.

[88] A. Faruqi, R. Henderson, and J. Holmes, "Radiation damage studies on STAR250 CMOS sensor at 300keV for electron microscopy" *NIM A* **565** (2006) no. 1, 139 – 143.

[89] B. Dryer, A. Hollanda, N. Murraya, P. Jerramb, M. Robbinsb, and D. Burtb, "Gamma Radiation Damage Study of 0.18 μm Process CMOS Image Sensors" in *Proc. of SPIE Vol*, vol. 7742, pp. 77420E–1. 2010.

[90] M. Esposito, T. Anaxagoras, O. Diaz, K. Wells, and N. Allinson, "Radiation Hardness of a Large Area CMOS Active Pixel Sensor for Bio-medical applications" *ISDI White Paper* .

[91] A. Akkerman, J. Barak, M. Chadwick, J. Levinson, M. Murat, and Y. Lifshitz, "Updated NIEL calculations for estimating the damage induced by particles and gamma-rays in Si and GaAs" *Radiation Physics and Chemistry* **62** (2001) no. 4, 301–310.

[92] A. Gay, "Measurement of the top-Higgs Yukawa coupling at a Linear e+ e- Collider" *Eur.Phys.J.* **C49** (2007) 489–497.

[93] W. Kilian, T. Ohl, and J. Reuter, "WHIZARD: Simulating Multi-Particle Processes at LHC and ILC" *Eur.Phys.J.* **C71** (2011) 1742.

[94] "Physics Study Libraries". `http://www-jlc.kek.jp/subg/offl/physsim/`.

[95] S. Catani, Y. L. Dokshitzer, M. Olsson, G. Turnock, and B. Webber, "New clustering algorithm for multi - jet cross-sections in e+ e- annihilation" *Phys.Lett.* **B269** (1991) 432–438.

[96] S. Catani, Y. L. Dokshitzer, M. Seymour, and B. Webber, "Longitudinally invariant K_t clustering algorithms for hadron hadron collisions" *Nucl.Phys.* **B406** (1993) 187–224.

[97] K. Seidel, S. Poss, and F. Simon, "Top Quark Pair Production at a 500 GeV CLIC Collider".

[98] M. Cacciari, G. P. Salam, and G. Soyez, "FastJet User Manual" *Eur.Phys.J.* **C72** (2012) 1896.

[99] J. Rouene, "Measurement of $t\bar{t}$ asymmetries with the ILD at the ILC". `http://ilcagenda.linearcollider.org/getFile.py/access?contribId=50&sessionId=10&resId=0&materialId=slides&confId=5468`, 2012.

[100] A. Hocker, J. Stelzer, F. Tegenfeldt, H. Voss, K. Voss, *et al.*, "TMVA - Toolkit for Multivariate Data Analysis" *PoS* **ACAT** (2007) 040.

[101] O. D. Miller, "Maps calorimetry for a future linear collider". July, 2011.

[102] N. Watson, S. Halliday, and G. Savage, "Performance Study of Digital ECAL in ILD". `http://ilcagenda.linearcollider.org/getFile.py/access?contribId=3&resId=2&materialId=slides&confId=5092`, 2011.

"I'm finished making sense, done pleading ignorance!"

Dave Grohl, Foo Fighters